



## 저작자표시-비영리-변경금지 2.0 대한민국

이용자는 아래의 조건을 따르는 경우에 한하여 자유롭게

- 이 저작물을 복제, 배포, 전송, 전시, 공연 및 방송할 수 있습니다.

다음과 같은 조건을 따라야 합니다:



저작자표시. 귀하는 원저작자를 표시하여야 합니다.



비영리. 귀하는 이 저작물을 영리 목적으로 이용할 수 없습니다.



변경금지. 귀하는 이 저작물을 개작, 변형 또는 가공할 수 없습니다.

- 귀하는, 이 저작물의 재이용이나 배포의 경우, 이 저작물에 적용된 이용허락조건을 명확하게 나타내어야 합니다.
- 저작권자로부터 별도의 허가를 받으면 이러한 조건들은 적용되지 않습니다.

저작권법에 따른 이용자의 권리는 위의 내용에 의하여 영향을 받지 않습니다.

이것은 [이용허락규약\(Legal Code\)](#)을 이해하기 쉽게 요약한 것입니다.

[Disclaimer](#)

이학박사 학위논문

Gravitational wave as a probe of  
dark matter physics

중력파를 이용한 암흑물질 물리학 탐사

2021 년 8 월

서울대학교 대학원

물리천문학부

최 한 길

Gravitational wave as a probe of dark matter physics

중력파를 이용한 암흑물질 물리학 탐사

지도교수 정 성 훈

이 논문을 이학박사 학위논문으로 제출함

2021 년 8 월

서울대학교 대학원

물리천문학부 물리학 전공

최 한 길

최한길의 이학박사 학위논문을 인준함

2021 년 5 월

위 원 장	_____	김 형 도
-------	-------	-------

부 위 원 장	_____	정 성 훈
---------	-------	-------

위 원	_____	이 형 목
-----	-------	-------

위 원	_____	김 석
-----	-------	-----

위 원	_____	정 동 희
-----	-------	-------

# Gravitational wave as a probe of dark matter physics

By  
Choi, Han-Gil

A DISSERTATION

submitted to the Faculty of  
Seoul National University  
in partial fulfilment of requirements for the degree of  
the Doctor of Philosophy

Supervised by  
Professor Jung, Sunghoon

Department of Physics and Astronomy,  
The Graduate School of Natural Science,  
Seoul National University

August 2021

# Abstract

Gravitational wave as a probe of dark matter physics

Han-Gil Choi

Department of Physics and Astronomy

The Graduate School

Seoul National University

In this dissertation, we present novel ways of probing dark matter(DM) physics through gravitational waves(GWs). We find that if a light scalar dark matter interacts with neutron and induces time-oscillating mass shift of it, GW chirps radiated by neutron star binary inspiral can be sensitive probe to such effects. The sensitivity comes from a large number of GW cycles during year-long measurements in broadband (0.01 Hz – 1000 Hz). Such broadband measurements that can be realized by a future detector network including LIGO and mid-band detectors will probe unconstrained parameter space of the light scalar DM.

We also show that gravitational lensing(GL) of GW can be a probe of dark matter subhalos at subgalactic scales( $M < 10^7 M_\odot$ ). It has been very challenging for GL of light to probe the scale. What special to GW is its parsec scale *Fresnel Length* which comes from its long wavelength and cosmological distance to the GW source. It makes possible GW chirps to be diffracted by the parsec-scale subhalos. We show that the diffractive lensing signal is equivalent to a *shear* distribution of a lens object, and therefore, it can be used for reconstruction of the lens profile. The event rate of such GW lensing is estimated to  $\mathcal{O}(10)$  per year at BBO.

**Keywords:** Gravitational wave, Dark matter, Gravitational lensing

**Student Number:** 2015-20356

# Contents

<b>Abstract</b>	<b>i</b>
<b>List of Figures</b>	<b>v</b>
<b>List of Tables</b>	<b>xi</b>
<b>1 Introduction</b>	<b>1</b>
1.1 Gravitational waves in Linearized GR . . . . .	2
1.2 Gravitational wave radiation from a binary star . . . . .	6
<b>2 A New Probe of Dark Matter-Induced Fifth Force with Neutron     Star Inspirals</b>	<b>11</b>
2.1 Introduction . . . . .	11
2.2 Overview . . . . .	13
2.3 Models of DM-induced fifth force . . . . .	15
2.4 Signals in Neutron Star inspirals . . . . .	16
2.4.1 Oscillating NS-NS mass-shift . . . . .	17
2.4.2 Other light-scalar (non-DM) effects in NS inspirals . . . . .	18
2.4.3 Mass-shift in other experiments . . . . .	19
2.4.4 Light-scalar(non-DM) effects in other experiments . . . . .	21

2.4.5	Equivalence-principle violation . . . . .	22
2.5	Broadband GW detectors and Calculation . . . . .	22
2.6	Prospects . . . . .	24
2.7	Discussion . . . . .	27
2.7.1	Origin of good sensitivity . . . . .	27
2.7.2	DM density dependence . . . . .	30
2.8	Conclusion . . . . .	30
<b>3</b>	<b>Small-scale shear: peeling off diffuse subhalos with gravitational waves</b>	<b>33</b>
3.1	Introduction . . . . .	33
3.2	Diffractional lensing formalism . . . . .	37
3.2.1	Lensing integral . . . . .	37
3.2.2	Diffraction condition . . . . .	39
3.2.3	Formalism for weak diffractional lensing . . . . .	41
3.2.4	Shear as the origin of frequency dependence . . . . .	44
3.2.5	Complete formalism with strong diffraction . . . . .	46
3.3	NFW lensing . . . . .	48
3.3.1	Profile . . . . .	48
3.3.2	Critical curves . . . . .	51
3.3.3	Diffractional lensing . . . . .	52
3.4	GW detection of NFW . . . . .	54
3.4.1	GW chirping . . . . .	54
3.4.2	Log-likelihood detection . . . . .	56
3.5	Prospects . . . . .	59
3.5.1	Semi-analytic estimation . . . . .	59
3.5.2	Results . . . . .	62

3.6	Generalization . . . . .	69
3.6.1	Lensing by power-law profiles . . . . .	69
3.6.2	Semi-analytic estimation . . . . .	72
3.6.3	Peeling off profiles . . . . .	75
3.6.4	Core-vs-cusp . . . . .	78
3.7	Summary . . . . .	78
<b>A</b>	<b>Appendix for Diffractive lensing</b>	<b>80</b>
A.1	$M_{\text{NFW}}$ scaling of milli-lensing perturbation . . . . .	80
A.2	Range of diffractive lensing near a caustic . . . . .	81
A.3	Single image of diffractive lensing . . . . .	83
A.4	Formulation of $\ln p$ . . . . .	84
A.5	Derivation of maximum $ \ln p $ . . . . .	87
A.6	Example diffractive lensing cross-sections . . . . .	88
	<b>Bibliography</b>	<b>90</b>
	<b>초록</b>	<b>105</b>
	<b>감사의 글</b>	<b>106</b>



# List of Figures

Figure 2.1	Single measurement of NS-NS at 10 Mpc with 4(aLIGO+AI) (blue) or with ET+BBO (red). Along the shown solid lines, the DM-induced mass-shift $\delta\mathcal{M}/\mathcal{M}$ equals to the chirp-mass accuracy. Each solid line corresponds to different setup and assumptions; see text for details. The aLIGO+AI 10yr and ET+BBO 1yr curves overlap. Higgs-portal model (left) and scalar-coupled to the trace of the stress-energy tensor (right). Also shown are existing (shaded) and reinterpreted (non-shaded) constraints on DM-induced effects (dashed) from IPTA, LLR displacement, and atomic clocks [27,40] and on non-DM effects (dot-dashed) from static EP test [17,37] and Yukawa searches with LLR [33], Keplerian test [36], Cassini [19], and NS-NS inspiral. . . . .	25
------------	--	----

Figure 2.2	Integration of all NS-NS measurements for 1 or 10 years with 4(aLIGO+AI) (blue) and ET+BBO (red). Along the shown solid lines, the DM-induced mass-shift $\delta\mathcal{M}/\mathcal{M}$ equals to the integrated chirp-mass measurement accuracy. Each solid line corresponds to different setup and assumptions; see text for details. The aLIGO+AI 1yr and LLR displacement curves overlap. Models and other sensitivity curves are as in Fig. 2.1. . . .	26
Figure 2.3	Improvement of Fisher errors in measurement time. NS-NS at 10 Mpc. Shown parameters are chirp-mass fractional accuracy, SNR, $N_{\text{cyc}}$ , sky-localization accuracy, and $D_L$ fractional accuracy. The second plot shows the correlation of chirp-mass accuracy and $\text{SNR} \times N_{\text{cyc}}$ . The considered measurement is for the last 1 year, sweeping $f \simeq 0.22 - 1000$ Hz. The blue-dashed lines assume no correlations with the 5 source parameters (see text for details), and the orange-dotdashed line assumes no correlation with any source parameters. . . . .	32

- Figure 3.1 Illustrating how the chirping GW detects a diffuse subhalo and successively peels off its profile. The solid circles with radii  $\sim$  Fresnel length  $r_F \propto 1/\sqrt{f}$  are the points on the lens plane being probed by the wave with frequency  $f$ ; also where the phase difference with an image “i” is 1. As the frequency chirps, the circle shrinks and the wave feels the mass distribution at successively smaller scales, hence frequency-dependent diffractive lensing essentially due to *shear*. When  $r_F \lesssim r_s$ , the source “s” begins to be well located/imaged by Fermat principle, hence frequency-independent geometric optics. SIS is used for illustration, where mass is densely distributed within the Einstein radius  $r_E$  which is also a boundary between weak and strong diffraction. NFW is more diffuse with essentially zero  $r_E$ . . . . . 36
- Figure 3.2 The surface mass density  $\Sigma(r)$  at the distance  $r$  from the center of the NFW profile, with  $M_{\text{NFW}} = 10^9, 10^6, 10^3 M_\odot$ . The star on each curve denotes the location of the scale radius  $r_0$ . The curves end at their virial radius,  $r_{\text{vir}} = cr_0$ , where  $c$  is given by the Okoli’s  $M_{\text{vir}} - c$  relation [130]. . . . . 49
- Figure 3.3  $|F(w)|$  (upper left),  $\frac{d|F(w)|}{d \ln w}$  (lower left),  $\varphi(w)$  (upper right), and  $\frac{d\varphi(w)}{d \ln w}$  (lower right) for NFW profiles with  $\kappa_0 = 0.002$  (red) and  $\kappa_0 = 0.001$  (blue). Solid lines are full numerical solutions of Eq. (3.13), while dashed are diffraction-limit results in Eqs. (3.51) and (3.52). Their  $|F(w)|$  and  $\varphi(w)$  are obtained according to Eqs. (3.22~3.25). All of them agree in the diffraction regime  $w \lesssim 2/x_s^2$ ; see more in text. Each curve is marked with  $x_s$  value. . . . . 51

Figure 3.4	The spectral density of GW detector noises $\sqrt{S_n(f)}$ (solid) and example chirping GW amplitudes $\sqrt{f} \tilde{h}(f) $ (dashed) with $M_{\text{BBH}} = 10^3 M_\odot$ and $10^5 M_\odot$ . $z_s = 1$ . The time marked with stars indicate the remaining time until final merger. . . . .	56
Figure 3.5	$ \ln p $ as a function of $x_s = r_s/r_0$ . Last 1 year of inspiral observed at LISA. . . . .	58
Figure 3.6	The range of Fresnel length Eq. (3.9) swept by a chirping GW during its last 1 year before merger (shaded). Other time periods are shown as dashed lines; ISCO refers to the innermost stable circular orbit. The corresponding GW frequencies are shown on the right vertical axis. Some part of this range, combined with detector sensitivities, must satisfy Eq. (3.65) for diffractive lensing. $z_s = 1, z_l = 0.35$ . . . . .	60
Figure 3.7	Semi-analytic estimation of the parameter space of NFW diffractive lensing. Diffractive lensing is relevant in the shaded region Eq. (3.65). Solid contours show the shear $\gamma(r_F)$ , reflecting the required SNR for detection. The frequency corresponding to $r_F$ is shown on the right vertical axis. For quick references, green bars roughly show maximal sensitivities at best frequencies. See text for details. $z_s = 1, z_l = 0.35$ . . . . .	62
Figure 3.8	Optical depth $\tau$ for the given $M_{\text{NFW}}$ comprising the full DM abundance (i.e. no halo mass function) at BBO (left), LISA (mid), and MAGIS (right). Each curve is marked with $M_{\text{NFW}}$ , and each panel with $M_{\text{BBH}}$ . Last 1 year of inspiral and $3\sigma$ log-likelihood lensing detection. . . . .	63

Figure 3.9	The number of lensing events per year $\dot{N}_L$ at BBO, LISA, and MAGIS, as functions of $M_{\text{NFW}}$ (top) or $M_{\text{BBH}}$ (bottom). The shaded bands are the range of optimistic and pessimistic $\dot{n}_s$ , while the solid lines are from constant $\dot{n}_s$ ; their total event rates are normalized as in Table 3.1. For comparison, dashed lines show results without a mass function; each $M_{\text{NFW}}$ comprises total $\Omega_{\text{DM}}$ . See more in text. Last 1 year of inspiral and $3\sigma$ log-likelihood lensing detection. . . . .	68
Figure 3.10	The amplitude and phase of $F(w)$ obtained by full calculation (solid), weak diffraction approximation Eq. (3.77) (dashed), and strong diffraction approximation Eq. (3.79) (dotted) for a power-law profile with $k = 1$ . $x_s = 0$ for simplicity. . . . .	70
Figure 3.11	Same as Fig. 3.7 but for SIS with $k = 1$ . Red contours show $\gamma(r_F)$ , reflecting the required SNR for detection, and blue contours show the enclosed mass within $r_F$ . Length scales, $r_{\text{vir}}$ and $r_E$ , are shown as dashed lines. . . . .	72
Figure 3.12	The comparison of $ \ln p $ for detection obtained with full numerical (solid) and approximate weak diffraction Eqs. (3.77) and (3.78) (dashed). Also shown are estimations using only shear and SNR Eq. (3.85) (dotted; which overlap with dashed). Each panel uses the BBH mass yielding maximum SNR. Horizontal lines denote the $3\sigma$ threshold, $ \ln p  = 5.914$ . . . . .	74
Figure 3.13	The Einstein mass and the corresponding frequency for $r_F = r_E$ , as a function of $M_{\text{vir}}$ . $k = 1.0$ (orange) and $1.5$ (blue). The region above(below) each line is the weak(strong) diffraction regime. Shaded regions represent the chirping frequency ranges measured at given detectors. $z_s = 1, z_l = 0.35$ . . . . .	76

Figure 3.14	Same as Fig. 3.12 but for profile measurement accuracies represented by $\delta k/k$ . Cases with $\delta k/k > 1$ are not shown. . . . .	77
Figure A.1	Contours of lensing cross-section in $z_s - z_l$ space. The number on the contours are $r_s^{\text{max}} \equiv \sqrt{\sigma_l/\pi}$ in parsec. Likewise in Fig. 3.5, LISA observation is assumed and the source and lens mass are set to $M_{\text{BBH}} = 10^6 M_\odot$ and $M_{\text{NFW}} = 10^7 M_\odot$ , respectively. . . . .	89

# List of Tables

Table 3.1	The expected numbers of lensing detections per year $\dot{N}_L$ and of total GW detections per year $\dot{N}_{\text{GW}}$ , at BBO, LISA, MAGIS, and ET. The results are marginalized over $M_{\text{NFW}} = 10^{3-10} M_\odot$ with the mass function Eq. (3.70) and summed for $M_{\text{BBH}} = 10^{2-8} M_\odot$ with three models of $\dot{n}_s$ : constant $\dot{n}_s = 0.01 \text{ Gpc}^{-3} \text{ yr}^{-1}$ , optimistic and pessimistic merger models of heavy BBHs [142]. Light BBH mergers are ignored. . . . .	65
-----------	---	----





# Chapter 1

## Introduction

Gravitational wave(GW) is a completely new window to the cosmos. GW is the ripple of the space-time curvature propagating with the speed of light, and is one of the main predictions of the Einstein's General relativity(GR). Same as electromagnetic waves which are radiated by acceleration of electric charge, GWs are radiated by acceleration of mass. Due to weak coupling between matter and gravity, the amplitude of GWs radiated by daily-size objects is completely ignorable. Even GWs sourced by violent astrophysical events such as binary star coalescence and supernovae explosion have extremely small amplitudes, detection of GW has been one of major challenges of modern physics. Despite it's smallness, GWs can carry the information on bulk motion of matters deep inside the astrophysical phenomena to an observer, and are expected to give us new insight on the universe.

Finally in 2015, after the centennial of the birth of GR, LIGO collaboration succeeded in direct detection of GW signal [2, 3]. The GW signal was radiated by the merger event of 30 solar masses binary black holes which occurred at a billion years

ago. Until now (2021), LIGO-VIRGO collaboration has been detected 20 GWs signals [4] which include completely new phenomena such as the coalescence of neutron star binary [5] and the formation of intermediate black hole [6]. The potential of GW astrophysics just have begun to be revealed. In the near future, as more GW detectors such KAGRA and LIGO-india join for GW observation, the number of GW signals and sensitivity to them will drastically improved, which is expected to revolutionize astrophysics.

Meanwhile, the realization of GW observation triggers the rise of interest in the application of GW to dark matter physics. Dark matter, the old mysteries, has revealed its existence only through gravitational interaction, which make its properties not much known until today. Although electromagnetic observation has been very powerful means for dark matter research, it has a clear limitation coming from high systematic errors due to strong interaction with ordinary matters. However, GW, as a pure gravitational probe, might become a game changer for dark matter hunting. In this dissertation, we propose the new way of probing dark matter physics by utilizing the unique properties of GW signals. The following sections of this introduction reviews the basics of gravitational wave.

## 1.1 Gravitational waves in Linearized GR

Although everything of general relativity (GR) are encoded in the Einstein's field equations

$$G_{\mu\nu} \equiv R_{\mu\nu} - \frac{1}{2}g_{\mu\nu}R = \kappa T_{\mu\nu}, \quad \kappa \equiv \frac{8\pi G}{c^4}, \quad (1.1)$$

where  $g_{\mu\nu}$  is space-time metric,  $R_{\mu\nu}$  and  $R$  are Ricci tensor and scalar, and  $T_{\mu\nu}$  is energy-stress tensor, it is almost impossible to solve the equations without simplifying assumptions due to their non-linearity. In this case, the most natural strategy is to find out their linear component by assuming small perturbations to simple and well-

known solutions. Gravitational waves are also well-understood in this context which is enough for most cases. In this section, we consider linearized GR on flat metric  $\eta_{\mu\nu} \equiv \text{diag}(-1, 1, 1, 1)$ , and will see that GR allow only two degree of freedom which propagate with speed of light.

We start with defining metric perturbation  $h_{\mu\nu}$  as

$$g_{\mu\nu} = \eta_{\mu\nu} + \epsilon h_{\mu\nu}, \epsilon \ll 1, \quad (1.2)$$

where  $\epsilon$  is introduced as a book-keeping parameter which eventually will be set to 1. Dealing with them with Lorentz covariant way is more conventional, but resulting gauge dependence somewhat dilute the fact that the true number of propagating degree of freedom is two. Therefore, instead, we adopt the decomposition of  $h_{\mu\nu}$  according to the transformation property with respect to  $SO(3)$ . The decomposition is given by

$$\begin{aligned} h_{00} &= A \\ h_{0i} &= \partial_i B + B_i \\ h_{ij} &= \frac{1}{3} D \delta_{ij} + \partial_{ij} E + \partial_i V_j + \partial_j V_i + h_{ij}^{TT} \end{aligned} \quad (1.3)$$

where the Latin indices take 1 to 3, and the newly introduced 3D vectors and tensor satisfy

$$\partial^i B_i = \partial^i V_i = \partial^i h_{ij}^{TT} = 0, h_{ij}^{TT} \delta^{ij} = 0. \quad (1.4)$$

Assuming appropriate fall of condition for  $r \rightarrow \infty$ , one can show that this decompo-

sition is uniquely determined as

$$\begin{aligned}
A &= h_{00} \\
B &= \Delta^{-1} \partial^i h_{0i} \\
B_i &= h_{0i} - \partial_i \Delta^{-1} \partial^j h_{0j} \\
D &= \frac{3}{2} (h_3 - \Delta^{-1} \partial^{ij} h_{ij}) \\
E &= -\frac{1}{2} \Delta^{-1} h_3 + \frac{3}{2} \Delta^{-2} \partial^{ij} h_{ij} \\
V_j &= \Delta^{-1} \partial^i h_{ij} - \partial_j \Delta^{-2} \partial^{kl} h_{kl} \\
h_{ij}^{TT} &= h_{ij} - (\text{remains}) ,
\end{aligned} \tag{1.5}$$

where  $\Delta \equiv \partial^i \partial_i$ , and  $h_3 \equiv h_{ij} \delta^{ij}$ . As one can see, suffering from non-local definition, this formalism is not preferable option for real-problem solving. However, we shall see that this method will clearly show the formal structure of linearized GR.

By the definition of  $h_{\mu\nu}$ ,  $h_{\mu\nu}$  should be properly redefined under a transformation of  $\eta_{\mu\nu}$ . Especially when the coordinate transformation

$$x^\mu \rightarrow x'^\mu = x^\mu + \epsilon \xi^\mu \tag{1.6}$$

does not significantly distort the background, it is the so-called gauge transformation of  $h_{\mu\nu}$ . Under Eq. (1.6),  $h_{\mu\nu}$  should transform as

$$h'_{\mu\nu} = h_{\mu\nu} + \partial_\mu \xi_\nu + \partial_\nu \xi_\mu . \tag{1.7}$$

Correspondingly, the transformations of Eq. (1.5) are

$$\begin{aligned}
A' &= A + 2\partial_0\xi_0 \\
B' &= B + \partial_0\xi^L + \xi_0 \\
B'_i &= B_i + \partial_0\xi_i^T \\
D' &= D \\
E' &= E + 2\xi^L \\
V'_i &= V_i + \xi_i^T \\
h'_{ij}{}^{TT} &= h_{ij}{}^{TT},
\end{aligned} \tag{1.8}$$

where  $\xi^L = \Delta^{-1}\partial^i\xi_i$ , and  $\partial^i\xi_i^T = 0$ . Note that one can find gauge-invariant scalar, vector, and tensor field by rearranging Eq. (1.8). While  $D$  and  $h_{ij}{}^{TT}$  are already gauge-invariant, the others are given by

$$\begin{aligned}
\Phi &\equiv A - 2\partial_0B + \partial_0^2E \\
K_i &\equiv B_i - \partial_0V_i.
\end{aligned} \tag{1.9}$$

In short,  $h_{\mu\nu}$  have two gauge-invariant degrees of freedom(DOF) for each scalar, vector, tensor component.

The linearized version of Riemann curvature tensor is given by

$$R_{\alpha\beta\gamma\delta} = \frac{1}{2}(\partial_{\beta\delta}h_{\alpha\gamma} - \partial_{\beta\alpha}h_{\gamma\delta} - \partial_{\gamma\delta}h_{\alpha\beta} + \partial_{\alpha\gamma}h_{\beta\delta}). \tag{1.10}$$

One can show that  $R_{\alpha\beta\gamma\delta}$  is invariant under Eq. (1.7). This implies it can be expressed in terms of  $\Phi$ ,  $D$ ,  $K_i$ , and  $h_{ij}{}^{TT}$ . Actually, we can write the Einstein tensor  $G_{\mu\nu}$  as

$$\begin{aligned}
G_{00} &= \frac{1}{3}\Delta D \\
G_{0i} &= \frac{1}{3}\partial_{0i}D + \frac{1}{2}\Delta K_i \\
G_{ij} &= \left(\frac{1}{2}\Delta\Phi + \frac{1}{3}\partial_0^2D - \frac{1}{6}\Delta D\right)\delta_{ij} \\
&\quad + \frac{1}{2}\left[\partial_{ij}\left(\frac{1}{3}D - \Phi\right) + \partial_iK_j + \partial_jK_i + \square h_{ij}{}^{TT}\right].
\end{aligned} \tag{1.11}$$

Before equating these results with  $T_{\mu\nu}$ , note that  $T_{\mu\nu}$  allows same decomposition :

$$\begin{aligned} T_{00} &= \rho \\ T_{0i} &= \partial_i S + S_i \\ T_{ij} &= P\delta_{ij} + \partial_{ij}\sigma + \partial_i\sigma_j + \partial_j\sigma_i + \sigma_{ij}, \end{aligned} \tag{1.12}$$

where  $\partial^i S_i = \partial^i \sigma_i = \partial^i \sigma_{ij} = \sigma_{ij} \delta^{ij} = 0$ . Not all the components are independent due to the conservation law  $\partial^\mu T_{\mu\nu} = 0$ . Their relations are given by

$$\begin{aligned} \partial_0 \rho &= \Delta S \\ \Delta \sigma &= \partial_0 S - P \\ \Delta \sigma_j &= \partial_0 S_j, \end{aligned} \tag{1.13}$$

and removes 4 DOF from  $T_{\mu\nu}$ . The remaining 6 DOF match with the 6 gauge-invariant DOF of  $h_{\mu\nu}$  through the Eq. (1.1). Finally, the Einstein equation with  $T_{\mu\nu}$  of order  $\epsilon$  gives

$$\begin{aligned} \frac{1}{3}\Delta D &= \kappa\rho \\ \Delta\Phi &= \kappa(\rho + 2P - 2\partial_0 S) \\ \Delta K_i &= 2\kappa S_i \\ \square h_{ij}^{TT} &= 2\kappa\sigma_{ij}. \end{aligned} \tag{1.14}$$

Therefore, we can clearly see that only transverse-traceless(TT) tensor components can propagate, and the scalar and vector are constrained by matter distribution, which can be connected to the conservation of energy and linear momentum of the whole system.

## 1.2 Gravitational wave radiation from a binary star

While the TT decomposition clearly shows radiative degree of freedom of gravitational fields, it is lack of practical usefulness due to its non-local properties. Solving the

Einstein equation with a specific gauge choice become the standard which can be found in many literature. We are going to follow the conventional steps to present the gravitational wave radiation of a binary star.

The Lorenz gauge of the linearized Einstein gravity is defined as

$$\partial^\mu \bar{h}_{\mu\nu} = 0, \quad (1.15)$$

where

$$\bar{h}_{\mu\nu} \equiv h_{\mu\nu} - \frac{1}{2} h \eta_{\mu\nu}, \quad (1.16)$$

is the trace-reversed metric. In this gauge, the Einstein's field equation is reduced to

$$\square \bar{h}_{\mu\nu} = -2\kappa T_{\mu\nu}, \quad (1.17)$$

and it is solved by

$$\bar{h}_{\mu\nu}(t, \mathbf{x}) = \frac{\kappa}{2\pi} \int d^3x' \frac{T_{\mu\nu}(ct - |\mathbf{x} - \mathbf{x}'|, \mathbf{x}')}{|\mathbf{x} - \mathbf{x}'|}. \quad (1.18)$$

At large distance which is far larger than a characteristic dimension, the solution is approximately

$$\bar{h}_{\mu\nu}(t, \mathbf{x}) \simeq \frac{\kappa}{2\pi r} \int d^3x' T_{\mu\nu}(ct - r, \mathbf{x}') = \frac{\kappa}{4\pi r} \ddot{I}_{ij}(ct - r), \quad (1.19)$$

where

$$I_{ij}(t) = \int d^3x' \rho(t, \mathbf{x}') x'_i x'_j. \quad (1.20)$$

To arrive at the last expression, we used the conservation law  $\partial^\mu T_{\mu\nu} = 0$  and integration by parts. After taking out the TT component by the projection operator  $P_{ij} = \delta_{ij} - x_i x_j / r^2$ , the expression is the famous quadrupole formula of gravitational wave :

$$\begin{aligned} h_{ij}^{TT}(t, \mathbf{x}) &= \frac{\kappa}{4\pi r} [\ddot{I}_{ij}(ct - r)]^{TT} \\ &= \frac{\kappa}{4\pi r} \frac{d^2}{dt^2} \mathcal{I}_{kl}(ct - r) \left[ P_{ik} P_{jl} - \frac{1}{2} P_{kl} P_{ij} \right], \end{aligned} \quad (1.21)$$

where

$$\mathcal{I}_{kl} = I_{kl} - \frac{1}{3}\delta_{kl}I. \quad (1.22)$$

Remaining part is finding out the energy flux due to the gravitational wave radiation. However, it is revealed to be highly non-trivial task which requires second order perturbations and spatial/time averaged quantities. The difficulty is mainly originated from the heart of general relativity, the equivalence principle which states that observer that lying on a point on space-time cannot distinguish a gravitation and acceleration(which is not a feature of gravitation) only with local measurements.

The localized energy of GW, although it is an effective and approximate concept, can be found to be [7]

$$T_{\mu\nu}^{\text{GW}} = \frac{1}{4\kappa} \langle \partial_\mu h_{ij}^{TT} \partial_\nu h_{TT}^{ij} \rangle, \quad (1.23)$$

where the  $\langle \cdot \rangle$  denotes the spatial/time average over few wavelength of GW. One can show that  $T_{\mu\nu}^{\text{GW}}$  satisfies the conservation laws and the gauge independence. The energy flux due to the quadrupole radiation is given by  $T_{0i}^{\text{GW}}$ . Plugging Eq. (1.21) into Eq. (1.23) and integrating  $T_{0i}^{\text{GW}}$  over the sphere, one find that

$$\frac{dE}{dt} = -\frac{\kappa}{40\pi c} \langle \ddot{\mathcal{I}}_{ij} \ddot{\mathcal{I}}_{ij} \rangle. \quad (1.24)$$

Now we are on the stage of calculating GW radiation from a binary star. Let the mass of binary star as  $m_1$  and  $m_2$ , and also define  $M = m_1 + m_2$  and  $\mu = m_1 m_2 / M$ . The energy density can be written by

$$\rho(t, \mathbf{x}) = m_1 c^2 \delta^3(\mathbf{x} - \mathbf{x}_1(t)) + m_2 c^2 \delta^3(\mathbf{x} - \mathbf{x}_2(t)), \quad (1.25)$$

where  $\mathbf{x}_1(t)$  and  $\mathbf{x}_2(t)$  are the position vectors of the stars. We assume the binary has circular orbit which is given by

$$\begin{aligned} \mathbf{x}_1 &= \frac{m_2}{M} a (\cos \Omega t \hat{x} + \sin \Omega t \hat{y}) \\ \mathbf{x}_2 &= -\frac{m_1}{M} a (\cos \Omega t \hat{x} + \sin \Omega t \hat{y}), \end{aligned} \quad (1.26)$$



where  $\Omega$  is orbital frequency and  $a$  is separation of the binary. Then, the inertia tensor  $I_{ij}$  can be found to be

$$\begin{aligned} I_{11} &= \frac{\mu c^2 a^2}{2} (1 + \cos 2\Omega t), \quad I_{22} = \frac{\mu c^2 a^2}{2} (1 - \cos 2\Omega t), \\ I_{12} &= \frac{\mu c^2 a^2}{2} \sin 2\Omega t, \\ I_{13} &= I_{33} = 0. \end{aligned} \quad (1.27)$$

Combining those quantities with Eq. (1.24), we have

$$\frac{dE}{dt} = -\frac{32G}{5c^5} \mu^2 a^4 \Omega^6 = -\frac{32G^{\frac{7}{3}}}{5c^5} \mu^2 M^{\frac{4}{3}} \Omega^{\frac{10}{3}}, \quad (1.28)$$

up to the Newtonian order, where  $a^3 = GM\Omega^{-2}$  and  $E = Mc^2 - \mu M/(2a)$ . If we rewrite the equation in terms of the GW frequency  $f = \Omega/\pi$ , the equation becomes

$$\frac{df}{dt} = \left( \frac{dE}{df} \right)^{-1} \frac{dE}{dt} = \frac{96G^{\frac{5}{3}}}{5c^5} \mathcal{M}^{\frac{5}{3}} \pi^{\frac{8}{3}} f^{\frac{11}{3}}, \quad (1.29)$$

where

$$\mathcal{M} \equiv M^{\frac{2}{5}} \mu^{\frac{3}{5}}, \quad (1.30)$$

is the chirp mass which takes the central role of GW astrophysics as well as this dissertation. Those aspects will be discussed shortly. Integrating Eq. (1.29) up to the cut-off frequency  $f_c$  (usually set to be inner-most-circular orbit frequency), the time evolution of frequency can be found as

$$t_c - t = \frac{5}{256} \frac{c^5}{G^{\frac{5}{3}} \mathcal{M}^{\frac{5}{3}} \pi^{\frac{8}{3}}} (f^{-\frac{8}{3}} - f_c^{-\frac{8}{3}}), \quad (1.31)$$

where  $t_c$  is the time at GW frequency being  $f_c$ , or by inverting the relation approximately with  $f_c \gg f$ ,

$$f(t) \simeq \frac{5^{3/8}}{8\pi} G^{-\frac{5}{8}} c^{\frac{15}{8}} \mathcal{M}^{-\frac{5}{8}} (t_c - t)^{-\frac{3}{8}} \quad (1.32)$$

Accordingly, the phase of GW is

$$\Phi(t) \equiv \int_t^{t_c} 2\pi f(t) dt = \Phi_c - 2 \cdot 5^{-5/8} G^{-\frac{5}{8}} c^{\frac{15}{8}} \mathcal{M}^{-\frac{5}{8}} (t_c - t)^{\frac{5}{8}}, \quad (1.33)$$

where  $\Phi_c$  is the GW phase at  $t_c$  which can be arbitrary chosen.

To obtain GW waveform, one need to calculate the TT projection of the inertia tensor. The TT projection with respect to the radial direction  $x_i/r$  can be easily obtained in spherical coordinate  $(\theta, \phi)$ . In the coordinates, one can find

$$[I_{\theta\theta}]^{TT} = -[I_{\phi\phi}]^{TT} = \frac{1}{2}(I_{11} \cos^2 \theta - I_{22}), [I_{\theta\phi}]^{TT} = I_{12} \cos \theta. \quad (1.34)$$

Using Eqs. (1.21), (1.27), (1.33), and (1.34), one can obtain GW waveform as follows:

$$\begin{aligned} h_+(t) &= -\frac{2G^{\frac{5}{3}}}{rc^4} \mathcal{M}^{\frac{5}{3}}(\pi f(t))^{\frac{2}{3}} (1 + \cos^2 \theta) \cos \Phi(t) \\ h_\times(t) &= -\frac{2G^{\frac{5}{3}}}{rc^4} \mathcal{M}^{\frac{5}{3}}(\pi f(t))^{\frac{2}{3}} (2 \cos \theta) \sin \Phi(t). \end{aligned} \quad (1.35)$$

As one can see in Eqs. (1.33) and (1.35), the dynamics of a binary star is almost completely determined by the single mass parameter. As a consequence, a binary star coalescence has a high predictability in spite of currently operating GW detectors being only sensitive to GW frequency. The unique property has been utilized to infer the population of binary black holes, to measure distance to binary neutron star merger, and etc. Until now, the application of GW measurement has been restricted to astronomy due to limitation of current GW detectors, however, the opportunity for probing fundamental physics will be widely open as soon as the next-generation GW detectors begin their operation. In this dissertation, we are going to explore the potential of GW physics in the aspect of its application to particle physics. In the first part of main text, we will show how GW measurement can become a sensitive probe to new forces, which are possibly byproducts of dark matter. In the second part, we will introduce how gravitational lensing of GW can be used to detect dark matter substructure at subgalactic scale.

## Chapter 2

# A New Probe of Dark Matter-Induced Fifth Force with Neutron Star Inspirals

This chapter was published as *New probe of dark matter-induced fifth force with neutron star inspirals. Phys. Rev. D 99, 015013 (2019)*.

### 2.1 Introduction

The Gravitational Wave (GW) from compact binary mergers are finally discovered [1]. The discovery has convinced the existence of solar-mass black holes for the first time [2] and tested General Relativity in a new way [3]. But more and foremost excitingly, in the upcoming years with next-generation GW detectors, its physics potential is bound to grow significantly and extend outside astrophysics.

In particular, binary neutron stars (NS) [5] are becoming new precision observatories. Their final years of inspirals can be tracked very precisely through the observation

of GW radiation. The final inspiral is strongly governed by general relativity, producing a well-predicted particular type of evolution called the “chirping”. The chirping inspiral is thus naturally immune to small perturbations from their environments or backgrounds. This allows not only the detection of binary GWs as tiny as  $10^{-21}$  fractional oscillation of the metric but also precision cosmology combined with optical counterparts [8].

But the immunity does not mean that small perturbations are irrelevant or unobservable. Often, they do leave important traces on the binary inspiral from which we can observe the binary environments – the Universe. One of the most exciting environmental effects would be from the dark matter (DM). For example, DM can accumulate at the core of NS, strongly modifying NS binary mergers [9–12]. A DM locus nearby the binary may be also able to perturb the binary orbit in such a way to enhance the instability or ellipticity [13]. The high-precision observation of NS inspirals with GW may have broader (unexplored) sensitivities to milder DM effects from more varieties of DM.

Dark matter is one of the biggest mysteries of the Universe. In spite of its unprecedented evidence, it has not been discovered yet. For decades, Weakly Interacting Massive Particle – WIMP – has been a main paradigm of DM, but all DM detection experiments so far have failed to discover it. Today, it became essential to explore broader possibilities of DM interactions and masses both theoretically and experimentally.

A light scalar DM is one important candidate that receives much attention these days. A wide range of its mass as light as  $10^{-23}$  eV is unconstrained. Various types of its couplings to matter are possible. There are also several well-motivated examples such as axions [14], fuzzy dark matter [15], relaxions [16] as well as simple scalar DM. These scalars might be relevant to the solution of important particle physics

problems such as strong QCD problem and the Planck-weak hierarchy. Thus, many direct detection experiments are proposed and ongoing; a good survey of them is in Ref. [17]. But to probe a complete range of possible masses and interactions of the DM, more new and complementary ideas are needed.

In this paper, we show that final years of NS-NS inspirals may be sensitive to light scalar DM-induced perturbations in a new way. We give an overview of the new observable and possible experimental setup in Sec. 2.2, then we introduce DM models in Sec. 2.3, discuss new observables and other existing ones in Sec. 2.4, experimental setup and calculation in Sec. 2.5, finally show and analyze results in Sec. 2.6 and 2.7.1, and conclude at the end.

## 2.2 Overview

We give an overview of the new DM-induced signal on the NS-NS inspiral, a signal that can be observed through the last years of inspiral at, e.g., LIGO plus mid-frequency detectors.

- Signal with the oscillating NS mass. The light scalar DM (not just light scalars) interacting with neutrons can induce the *time-oscillating mass-shift* of NS-NS binaries. The oscillation is due to the lightness of DM with long phase coherence. The phase coherence is kept for long enough periods  $\sim 1/m_{\text{DM}}v^2 \gg 1/m_{\text{DM}}$  because DM is non-relativistic  $v \sim 10^{-3}$ . Thus, the lightest possible DM oscillates coherently at its Compton frequency,  $m_{\text{DM}} \gtrsim 10^{-22} \text{ eV} \approx 0.76/\text{year}$ , which is about 1 per year.
- Enhanced sensitivity to the chirp-mass. The oscillation in time is a key property that provides a time-dependent change to detect the mass shift. As long as the DM Compton period is within inspiral measurement time, the oscillation is

detectable, through the exquisite chirp-mass measurement from GW waveform evolution. The sensitivity benefits from *a large number of GW cycles* during a long measurement, which can accumulate a tiny phase shift (from the chirp-mass shift) in each cycle to a detectably large one. Thus, the chirp-mass accuracy is augmented by  $\sim N_{\text{cyc}} \cdot \text{SNR}$  (not just SNR).

- Highest-frequency broadband. The broadband  $f \simeq 0.01 - 1000$  Hz (e.g. with LIGO + mid-frequency detectors) is ideal to detect the DM effects, as it is the *highest-frequency band with year-long lifetime* of NS-NS binaries. Not only can a long measurement enhance  $N_{\text{cyc}}$  and SNR, but the highest-frequency end can also resolve important parameter degeneracies, partly by utilizing the Doppler effects around the Sun. In addition, as mentioned, the year-long measurement is also a proper time scale to probe the lightest scalar DM.
- NS-NS. The NS-NS is the type of binaries that can test the DM induced effect. Here, non-DM light-scalar effects (such as dipole radiation of the scalar and Yukawa force) is absent or at least suppressed. We focus on the NS-NS case in this paper.
- Other probes. There are existing and proposed experiments that can be sensitive to light-scalar DM effects: pulsar timing arrays, lunar laser ranging, atomic clocks, GW interferometers, and torsion balance experiments. These can search for the DM-induced time-varying clock rate,  $\alpha$ , acceleration, and equivalence-principle (EP) violation. Our new probe – looking for the DM-induced absolute mass-shift – can be competitive or complementary to those.

## 2.3 Models of DM-induced fifth force

A light scalar DM shows its wave nature through its long phase coherence. Although background DM is an incoherent superposition of individual DM waves, their phase coherence is retained for a long time  $\sim 1/(m_{\text{DM}}v^2) \gg 1/m_{\text{DM}}$ . Within that time, DM then coherently oscillates at the Compton frequency  $m_{\text{DM}} = 2.42 \times 10^{-8} \text{Hz} \left( \frac{m_{\text{DM}}}{10^{-22} \text{eV}} \right)$ , and its background effect can be collectively enhanced.

Testable signals arise when the light scalar DM interacts with the visible matter (hence, the fifth force), in particular with the neutron in this paper. We introduce benchmark models for this phenomena:

- Higgs portal DM. The mixing between the DM  $\phi$  and the Higgs  $h$  induces the coupling to the neutron  $n$

$$\mathcal{L} \supset \frac{b\phi}{m_h^2} \langle h \rangle g_{hnn} \bar{n}n \quad \rightarrow \quad \frac{b\phi}{m_h^2} c_N m_n \bar{n}n, \quad (2.1)$$

where the non-perturbative QCD effects on the nucleon coupling is captured by  $c_N \approx 200 \text{MeV}/m_n$  with significant uncertainties [18]. The DM wave almost coherently oscillates in time and space with the amplitude set by the DM density:  $\phi(t) = (\sqrt{\rho_{\text{DM}}}/m_\phi) \cos(m_\phi t)$ . The coefficient  $b$  is our free parameter.

The couplings to protons and electrons are also generated by the mixing; since these couplings are not proportional to the masses due partly to QCD confinement effect, they generally break the (weak) equivalence principle (EP) [18]. For constraints on the weak EP-violation, we take the results in Ref. [17]. Couplings to photons and gluons can also be generated (at least through loops of charged/colored particles). But searches of such couplings from the lightest possible DM is absent. We focus on the coupling to the neutron in this paper.

- Scalar DM coupled to the trace of the stress-energy tensor  $T = T^\mu_\mu$

$$\mathcal{L} \supset g_\phi \phi T, \quad (2.2)$$

where  $g_\phi$  is a universal coupling constant. In the long-wavelength limit of  $\phi$ , the interaction term for the neutron is effectively equivalent to

$$\mathcal{L} \supset g_{\phi nn} \phi \bar{n} n, \quad (2.3)$$

where  $g_{\phi nn} = g_\phi m_n$  is our free parameter specialized to the neutrons. We assume no other modifications in the gravitational sector. This model does not violate the weak EP, but the strong EP is still broken. One can find that  $\phi$  violates the strong EP in the following two ways: (1) the outcome of the elementary particle mass measurements depend on the space-time varying intensity of  $\phi$ , (2) the self-energy dependence (due to the self-energy of  $\phi$ ) of the free-falling acceleration under the external fields ( $g_{\mu\nu}$  and  $\phi$ ). The effect of the scalar field  $\phi$  can be constrained by not only the tests of the fifth force but also by the tests of the general relativity, such as the Shapiro delay measurement from Cassini spacecraft [19] and strong-EP tests by the observation of stellar binary or triple systems containing a pulsar [20, 21]. The Cassini constraints are stronger and will be shown in our results.

## 2.4 Signals in Neutron Star inspirals

We introduce the new observable in Sec. 2.4.1, then we review non-DM signals in NS-NS in Sec. 2.4.2, other mass-shift effects in Sec. 2.4.3, other light scalar non-DM effect Sec. 2.4.4 and equivalence-principle violating effects in Sec. 2.4.5.



### 2.4.1 Oscillating NS-NS mass-shift

The neutron-star(NS) inspiral interacts with the background DM distributed over the space through which it moves. This interaction can leave traces<sup>1</sup> as (1) the oscillating mass-shift of NS, (2) oscillating external forces on the NS. The former one is our focus in this paper, and we show that NS-NS inspirals can be used to test this DM effect.

The (oscillating) fractional neutron mass-shift from the two benchmark models is

$$\frac{\delta m_n}{m_n} = \begin{cases} c_N \frac{b\phi}{m_h^2} = c_N \frac{b\sqrt{\rho_{\text{DM}}}}{m_\phi m_h^2} \simeq 8.0 \times 10^{-13} \left( \frac{b}{10^{-9}\text{eV}} \right) \left( \frac{10^{-7}\text{Hz}}{m_\phi} \right) \cos(m_\phi t) \\ \frac{g_{\phi nn}\phi}{m_n} = \frac{g_{\phi nn}\sqrt{\rho_{\text{DM}}}}{m_\phi m_n} \simeq 6.3 \times 10^{-13} \left( \frac{g_{\phi nn}}{10^{-23}} \right) \left( \frac{10^{-7}\text{Hz}}{m_\phi} \right) \cos(m_\phi t) \end{cases} \quad (2.4)$$

The effect is proportional to  $\phi \propto \sqrt{\rho_{\text{DM}}}$  so that galactic centers where the majority of both DM and NS-NS reside are good places to detect the DM effect. We base our numerical calculation on the value of  $\rho_{\text{DM}} = 77.3 \text{ GeV}/\text{cm}^3$  from the 0.8 kpc flat-core value of Burkert profile, but we also consider variations later. The neutron mass-shift will induce the NS mass-shift, hence the NS-NS chirp-mass shift

$$\frac{\delta \mathcal{M}}{\mathcal{M}} = a \frac{\delta m_n}{m_n} \quad (2.5)$$

with  $a = 1$  for NS-NS binary, but there can be a mild suppression from the neutron fraction in the NS.

The mass-shift becomes observable as it oscillates in time:  $\delta \mathcal{M}(t)/\mathcal{M} \propto \sqrt{\rho_{\text{DM}}} \cos(m_\phi t)$ . The time-oscillation of the chirp mass induces a characteristic change of the GW evolution that cannot be mimicked by GR effects. As a proxy of sensitivity, we will calculate the parameter space where the oscillation amplitude equals to the chirp-mass measurement accuracy; we discuss our calculation in the next section and show results in Fig. 2.1 and 2.2. The chirp mass can be exquisitely well measured through a huge number of GW cycles and highest-frequency data, as will be discussed. For the

---

<sup>1</sup>Similar DM effects on binary pulsars have been studied in Ref. [22] based on DM oscillation in resonant with binary orbital frequency.

chirp-mass oscillation to be detected, at least a large portion of an oscillation should be within the GW measurement time (about a year or longer in  $f \geq 0.01$  Hz). Since  $m_\phi \gtrsim 10^{-22}$  eV = 0.76/yr and their phase coherence is retained for much longer time, the (multi) year-long high-frequency GW measurement is proper to test the lightest possible DM.

#### 2.4.2 Other light-scalar (non-DM) effects in NS inspirals

A light scalar can also induce other effects in NS-NS binaries, the non-DM effects that exist even if the scalar is not the main fraction of DM. The exchange of light scalars  $\phi$  mediates a long-range Yukawa force between the neutron stars, deviating from the  $1/r^2$  law

$$\mu \frac{v^2}{r} = \frac{G\mu M}{r^2} (1 + \alpha(1 + m_\phi r)e^{-m_\phi r}), \quad (2.6)$$

where  $\alpha = \frac{b^2 c_N^2}{m_h^4} \frac{1}{4\pi G} \simeq 1.48 \times 10^{-9} (\frac{b}{10^{-9} \text{ eV}})^2$  for the first model and  $\alpha = \frac{g_{\phi nn}^2}{4\pi G m_n^2} \simeq 1.44 \times 10^{-9} (\frac{g_{\phi nn}}{10^{-23}})^2$  for the second model, and the reduced and total mass  $\mu$  and  $M$ .

The effect on the GW waveform evolution can be described approximately by the shift of the chirp mass  $\frac{\delta \mathcal{M}(r)}{\mathcal{M}} \simeq \frac{2}{5} \alpha (1 + m_\phi r) e^{-m_\phi r^2}$ . The resulting radius-dependent (hence, frequency-dependent) chirp mass is a clean signal that cannot be mimicked by GR effects. The total change of the chirp mass during a measurement starting from  $f_i$  (or  $r_i$ ) until  $f_f$  (or  $r_f$ ) is given by

$$\begin{aligned} \frac{\delta \mathcal{M}}{\mathcal{M}} &\simeq \frac{2}{5} \alpha \left( (1 + m_\phi r_f) e^{-m_\phi r_f^2} - (1 + m_\phi r_i) e^{-m_\phi r_i^2} \right) \\ &\approx \begin{cases} \frac{2}{5} \alpha (1 - \frac{1}{2} m_\phi^2 r_f^2), & r_i \gg \frac{1}{m_\phi} \\ \frac{1}{5} \alpha m_\phi^2 (r_i^2 - r_f^2), & r_i \ll \frac{1}{m_\phi} \end{cases} \lesssim \frac{2}{5} \alpha \end{aligned} \quad (2.7)$$

The change is maximal,  $\frac{2}{5} \alpha$ , for the scalar mass in the range  $r_i \gg 1/m_\phi \gg r_f$ . The range, for the NS-NS binary, is  $r_i(f = 0.1 \text{ Hz}) \simeq (7.8 \times 10^{-14} \text{ eV})^{-1} \simeq 16000 \text{ km}$  and

---

<sup>2</sup>Our method applied to ET yields similar or actually slightly worse sensitivity than the more dedicated estimation in Ref. [25].

$r_f(f = 1000 \text{ Hz}) \simeq (3.7 \times 10^{-11} \text{ eV})^{-1} \simeq 34 \text{ km}^3$ . Thus, this effect can only probe those range of the DM mass (in our experimental setups); lighter Yukawa force essentially looks the same as gravity. In Fig. 2.1 and 2.2, we show the parameter space where Eq. (2.7) equals to the chirp-mass accuracy.

A light scalar (again not necessarily the main DM) can also be efficiently radiated if each NS carries different scalar charge-to-mass ratio, forming a scalar-charge dipole [10, 23]. This dipole radiation is qualitatively different from the GW quadrupole radiation, thus can be tested with GW waveform evolution [23–25]. It is efficient for any light scalars with long enough Compton wavelength  $1/m_\phi \gtrsim 10 \text{ km}$ . But this effect is absent in the NS-NS in our model, as every NS has the same charge ( $m_{\text{NS}}/m_n$ ) to mass ( $m_{\text{NS}}$ ) ratio  $= 1/m_n$ ; at least, the radiation is suppressed by a small variation of the neutron fraction in the NS. In the NS-BH, on the other hand, the dipole radiation is efficient and dominant effect of light scalars, prohibiting the detection of the DM effects – the oscillating mass-shift. Thus, in this paper, we focus on the NS-NS as the type of binaries that can test the light-scalar DM effects.

### 2.4.3 Mass-shift in other experiments

Pulsars are highly stable and regular clocks. If its mass changes by DM effects, its rotation period (hence, the clock) also changes; see also Ref. [22]. This leaves an oscillating timing residual on each pulsar timing measurement. Each pulsar’s variation is uncorrelated with those of every other pulsar since pulsars are separated by distances much longer than the DM Compton wavelength. Thus, the average of pulsar timing array (PTA) can provide a stable clock, cancelling the DM effect [17]. This PTA clock may be compared with individual pulsar timing to measure the oscillation.

With EP violations, the pulsar measurement can also be affected by the varia-

---

<sup>3</sup>For LIGO-band expected sensitivities, refer to Refs. [10, 23–25].

tion of atomic clocks on the Earth [17]. The atomic-clock rate varies because atomic transition frequencies are affected by the DM-induced variations of nucleus (and electron) masses and fine-structure constant  $\alpha$  [26–30]. But all the atomic clocks oscillate coherently on the Earth while independently from all the pulsars. Thus, individual pulsar’s oscillation can perhaps be distinguished from atomic clock oscillations.

Therefore, we assume that DM-induced mass-shift can be detected by either observation, whether EP is conserved or not. One difference is that DM density at pulsars can be different from local density that affects the atomic clocks on the Earth. In the future, this difference can be exploited to better measure DM effects. Today, however, most pulsars used in IPTA [31] and Parkes PTA [32] are within  $1 \sim 2$  kpc from the Earth<sup>4</sup>. Thus, we use the same local DM density  $\rho_{\text{DM}} = 0.39 \text{ GeV}/\text{cm}^3$  to estimate both effects. They give equivalent sensitivities at the end so that we essentially do not distinguish the two observables.

The first release of IPTA [31] achieved the timing sensitivity  $\Delta t \approx \sigma_t / \sqrt{N_p N_m}$  with r.m.s. timing residual  $\sigma_t \simeq 1 \mu\text{s}$ ,  $N_p = 50$  pulsars and  $N_m \simeq 10 \text{ yr}/2 \text{ weeks}$  total number of measurements. In our final results, we compare this sensitivity with the DM-induced mass-shift or timing-residual amplitude

$$\Delta t \simeq \int dt \frac{\delta T}{T} \simeq \frac{1}{m_\phi} \frac{\delta m_n}{m_n}. \quad (2.8)$$

Lunar laser ranging (LLR) may be also sensitive to the absolute mass-shifts of the Earth and the Moon. About 50% of their masses come from neutrons, so their fractional mass-shift is approximately  $\frac{1}{2} \frac{\delta m_n}{m_n}$ . We assume that the mass-shift induces a change or perturbation in orbital radius about the same fractional size as the fractional mass-shift. The LLR measurement of the separation distance is currently limited by  $\delta \ell \leq 1 \sim 2 \text{ cm}$  [33]. We take the fractional sensitivity on the mass-shift to

---

<sup>4</sup>Presumably, pulsars and NS-NS are both accumulated at galactic center (GC). But the observed distributions (pulsars with lights and NS-NS with GWs) could be somewhat different. See Sec. 2.7.2 for more discussions.

be

$$\frac{\delta\ell}{(3.8 \times 10^5 \text{ km})} \simeq \frac{1}{2} \frac{\delta m_n}{m_n} \lesssim 5 \times 10^{-11}. \quad (2.9)$$

In our final results, we compare this sensitivity with the DM-induced mass-shift.

It is also proposed that GW interferometers can detect DM-induced space-time varying accelerations on the mirrors [17, 34, 35]. The best sensitivity is achieved when the DM Compton frequency matches approximately with the interferometer sensitivity range, hence  $m_\phi \sim 100 \text{ Hz}$  or  $10^{-3} \text{ Hz}$  for LIGO and LISA, for example.

#### 2.4.4 Light-scalar(non-DM) effects in other experiments

A long-range Yukawa force has been also searched in other observations: lunar laser ranging (LLR) [33] and Keplerian tests from planetary motions. We show these existing constraints taken from Ref. [36]. Note that the searches only cover up to 1 AU ( $\sim 10^{-18} \text{ eV}$ ) scale.

In contrast, the Shapiro time delay measurement of the Cassini spacecraft [19] can give constraints above 1 AU too. During the period of 15 days before and after the Cassini solar conjunction event, the Cassini spacecraft and the ground antenna on the Earth have exchanged the radio signals. The strong gravity of the Sun delays the round-trip time of the radio signal by  $\Delta t$

$$\Delta t \propto 4 \frac{GM_\odot}{c^3} = 4(1 - \alpha) \frac{GM_\odot^{\text{orbital}}}{c^3}, \quad (2.10)$$

where  $M_\odot^{\text{orbital}} = M_\odot(1 + \alpha)$  is what is determined by the orbital motion (under the influence of both gravity and the  $\phi$ -Yukawa force). The time-delay of the radio signal is not affected by the  $\phi$ -Yukawa force. Thus, the  $\phi$ -Yukawa force (or, the strong EP-violation) can be searched by comparing the two effects as in Eq. (2.10).  $2\alpha \lesssim 2.1 \times 10^{-5}$  from Cassini experiment [19]. This is weaker than the static EP-violation searches for the first model, but is relevant to the strong EP-violating second model.

Other constraints from stellar binaries or triple systems containing a pulsar [20, 21] are weaker.

#### 2.4.5 Equivalence-principle violation

There are existing and proposed experiments that can be sensitive to light-scalar EP violation. Stringent limits were obtained from the EP tests of Eöt-Wash torsion balance [37] and MICROSCOPE free-falling Earth orbit [38] experiments (see also Ref. [39]). But both measure static non-DM effects. We show the Eöt-Wash constraint taken from Ref. [17] in our final results.

On the other hand, atomic clocks can be sensitive to EP-violating DM effects. Depending on the atom’s proton and neutron fractions, oscillating DM can induce different variations of clock rate. To measure the differences, one can compare clock rates among atomic clocks made of different atoms [26–28, 40, 41], or accelerations among atom-interferometers made of different atoms [17], or the PTA clock rates measured by different atomic clocks [17]. Torsion balance experiments may also be sensitive to DM effects by sensing DM-induced force directions that may not point to the Earth. These searches all depend on the local DM oscillation. We show existing constraints from atomic clock experiments [27, 40] in our final results.

### 2.5 Broadband GW detectors and Calculation

We discuss proposed experimental setups and our calculation.

The crucial for exquisite chirp-mass measurement are a large number of GW cycles and highest-frequency chirping. Thus we consider final 1-year and 10-year measurements of NS-NS binaries, long enough and highest-frequency measurements that are proper for this work. At  $1\sim 10$  years before the merger, the redshifted GW frequencies are  $\mathcal{O}(0.01 - 0.1)$  Hz (where the lower range corresponds to  $z_S \simeq 10$ ) and reach

the innermost stable orbit (ISCO) at  $\mathcal{O}(100 - 1000)$  Hz. We combine mid- and high-frequency detectors to cover those range of frequencies  $0.01 \text{ Hz} \lesssim f \lesssim 1000 \text{ Hz}$ .

The first benchmark detector-network consists of 4 sets of aLIGO (design sensitivity) [42] + Atom Interferometer (AI) (resonant mode) [137, 138]; and the more optimistic benchmark network consists of one set of Einstein Telescope (ET) [45] + Big Bang Observatory (BBO) [46]. The second benchmark has  $\mathcal{O}(10)$  times smaller noise.

Our calculation proceeds as follow. Since we consider year-long or longer measurements, particular detector properties (baseline direction and their rotation, etc) are not so important. Thus, for the calculational simplicity, we use the simplest antenna function (from a single-baseline AI detector) for all kinds of detectors mentioned above; we follow the procedure in Ref. [47]. Considering more accurate and complicated antenna functions may even improve the chirp-mass precision, thus our estimation may be conservative in this sense. For GW waveforms, we use  $m_{\text{NS}} = 1.3M_{\odot}$  with the amplitude at the Newtonian order. The GW phase includes post-Newtonian corrections up to 1.5PN at which the reduced mass  $\mu$  and spin-orbit parameter  $\beta$ . We pick a random set of extrinsic source parameters (sky location, polarization, orbit inclination) that are close to the orientation-averaged GW amplitude; we use the same parameters as in Ref. [47]. For further simplicity, we assume that spins and orbital eccentricities are zero.

Our goal is to compare the DM-induced chirp-mass shift in Eq. (2.5) with the chirp-mass measurement accuracy, as a proxy of sensitivity to the DM effect. We envisage that oscillating data have the sensitivity to the oscillating part of the chirp mass at the same level as the chirp-mass accuracy without oscillations; thus, inspirals can be sensitive equally to any oscillation frequency as long as it is within the inspiral measurement time. The chirp-mass accuracy (without oscillations) is estimated by the

Fisher information matrix,  $F$ . We include 10 source parameters: sky location  $(\theta, \phi)$ , polarization, inclination, luminosity distance  $D_L$ , coalescence time  $t_c$ , constant phase-shift, masses (chirp mass  $\mathcal{M}$  and reduced mass  $\mu$ ), and spin-orbit coupling  $\beta$  (although we set spins to zero, we do not assume that we know it). The parameter definition and calculation are followed from Refs. [47, 48]. Fisher matrices from different detectors are added linearly; equivalently, SNR is added in quadrature. The accuracy of a parameter is given by the square-root the inverse-Fisher diagonal elements  $\sqrt{(F^{-1})_{ii}}$ ; thus, it improves with the square root of the number of measurements and linearly with SNR.

## 2.6 Prospects

Fig. 2.1 and Fig. 2.2 are our main results. We show the parameter space (solid lines) where the mass-shift amplitude Eq. (2.5) equals to the chirp-mass Fisher accuracy. Fig. 2.1 is from the single measurement of NS-NS at 10 Mpc, and Fig. 2.2 is from the integration of all NS-NS measurements (for 1 or 10 years) according to their merger-rate distributions. Each solid line corresponds to different setup and assumptions, each of which will be discussed. Also shown are existing (shaded) or proposed (non-shaded) sensitivities on DM effects (dashed) from IPTA and LLR displacement and on non-DM effects (dot-dashed) from Eöt-Wash EP test and Yukawa searches with LLR, Keplerian test, Cassini, and NS-NS inspiral in our experimental setups. As discussed, for the second model, we do not show weak EP-test results. And whether EP is conserved or not, IPTA probes oscillating DM effects in both models, either by pulsar mass-shift or period-variation. Notably, a large part of the light-DM parameter space of the second model is unconstrained.

The single measurement of NS-NS at 10 Mpc (Fig. 2.1), if we are lucky to see this, alone can be already powerful. In particular, for the EP-conserving second model, this



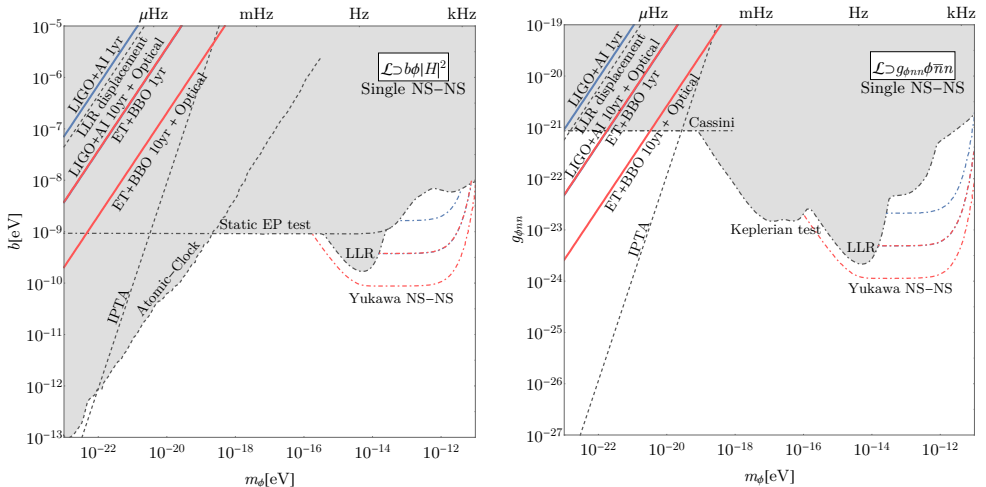


Figure 2.1 Single measurement of NS-NS at 10 Mpc with 4(aLIGO+AI) (blue) or with ET+BBO (red). Along the shown solid lines, the DM-induced mass-shift  $\delta\mathcal{M}/\mathcal{M}$  equals to the chirp-mass accuracy. Each solid line corresponds to different setup and assumptions; see text for details. The aLIGO+AI 10yr and ET+BBO 1yr curves overlap. Higgs-portal model (left) and scalar-coupled to the trace of the stress-energy tensor (right). Also shown are existing (shaded) and reinterpreted (non-shaded) constraints on DM-induced effects (dashed) from IPTA, LLR displacement, and atomic clocks [27, 40] and on non-DM effects (dot-dashed) from static EP test [17, 37] and Yukawa searches with LLR [33], Keplerian test [36], Cassini [19], and NS-NS inspiral.

can probe unconstrained parameter space. It can also strengthen or complement other expected sensitivities from LLR displacement and IPTA.

Each solid line shows possible improvements. The top line assumes 4(aLIGO+AI) for 1-yr integration time with full  $10 \times 10$  Fisher matrix, and the second line assumes a 10-yr integration with *a posteriori* optical-counterpart information to remove the 5 degeneracies with sky-location  $(\theta, \phi)$ , luminosity distance (redshift with standard cosmology), coalescence time (knowing when merges), spin  $\beta$  (knowing that NS has small spin). The last two lines show ET+BBO results with the same set of assumptions. A smaller noise (LIGO+AI  $\rightarrow$  ET+BBO) improves the chirp-mass accuracy by about

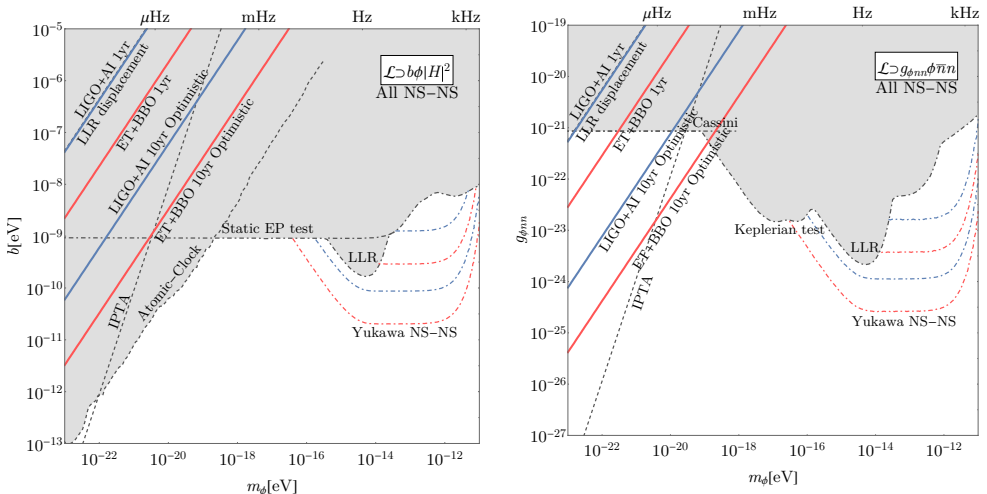


Figure 2.2 Integration of all NS-NS measurements for 1 or 10 years with 4(aLIGO+AI) (blue) and ET+BBO (red). Along the shown solid lines, the DM-induced mass-shift  $\delta\mathcal{M}/\mathcal{M}$  equals to the integrated chirp-mass measurement accuracy. Each solid line corresponds to different setup and assumptions; see text for details. The aLIGO+AI 1yr and LLR displacement curves overlap. Models and other sensitivity curves are as in Fig. 2.1.

50 times larger SNR, whereas a longer measurement (1 year  $\rightarrow$  10 years) by about 10 times larger  $N_{\text{cyc}}$ . Removing the 5 degeneracies improves by another factor of 2; this relatively small improvement is one of the highest-frequency benefits (see the next section). For a shorter 1-yr integration, the degeneracies with sky-location and spin  $\beta$  are similar, but the latter one becomes more important for a longer 10-yr integration. This is because spin effects are irrelevant at low-frequency (farther separation) regimes, thus longer lower-frequency data do not contain much spin information.

A combination of all NS-NS observations for  $T = 1$  or 10 years of integration (Fig. 2.2) can extend the reach by a few orders of magnitudes. Summing all observa-

tions enhances the sensitivity statistically, scaling approximately as

$$\left( \int dz \frac{4\pi\chi(z)^2}{H(z)} \left( \frac{10 \text{ Mpc}}{\chi(z)} \right)^2 \frac{\dot{n}}{(1+z)^2} \left( \frac{T}{\text{year}} \right) \right)^{1/2}, \quad (2.11)$$

with the binary redshift  $z$ , comoving distance  $\chi$ , comoving merger-rate density of NS-NS  $\dot{n}$  (we assume a constant comoving density), the Hubble constant today  $H_0 = 70 \text{ km/sec/Mpc}$  and  $\Omega_M = 0.3$ ,  $\Omega_\Lambda = 0.7$  for matter and  $\Lambda$  energy fraction. The two sets of predictions shown are based on lower and optimistic values of  $\rho_{\text{DM}}$  and  $\dot{n}$ . For the lower expectation, we use  $\rho_{\text{DM}} = 77.2 \text{ GeV/cm}^3$  from 0.8 kpc flat-core Burkert profile (similar to 0.1 kpc NFW and Einasto values) and  $\dot{n} = 1000/\text{Gpc}^3/\text{yr}$  [49] from the central value of predictions. For the optimistic case, we use  $\rho_{\text{DM}} = 1000 \text{ GeV/cm}^3$  [50] maximum not exceeding the  $\mathcal{O}(10)\%$  of baryonic mass inside the 100 pc galactic center (which can be constrained by future pulsar-timing residual measurements from SKA/FAST [32]) and  $\dot{n} = 12000/\text{Gpc}^3/\text{yr}$  [49] maximum consistent with LIGO observations so far. The “optimistic” curves are the optimistic results with 10-yr integration and the 5 degeneracies removed. It improves the lower sensitivity by about a factor 250. After all, the most optimistic sensitivity reaches down to an exquisite level,  $b \lesssim 10^{-11} \text{ eV}$  and  $g_{\phi nn} \lesssim 10^{-25}$ , from the 10-year integration with ET+BBO for the lightest DM.

## 2.7 Discussion

### 2.7.1 Origin of good sensitivity

We now turn to analyze the origin of good sensitivity to small DM effects.

Above all, the potential chirp-mass measurement accuracy is significantly enhanced by a large  $N_{\text{cyc}}$  (during year-long measurement). It is because a tiny phase shift in each cycle can be accumulated to an observably large one after  $N_{\text{cyc}}$  cycles [51, 52]. For example, the last 1 year measurement of NS-NS at 10 Mpc yields

$N_{\text{cyc}} \simeq 10^7$  and  $\text{SNR} \simeq 600$  (see Fig. 2.3) so that the fractional accuracy is expected to be enhanced as  $1/(\text{SNR} \cdot N_{\text{cyc}}) \sim 10^{-9}$ , instead of just  $1/\text{SNR} \sim 10^{-2}$ . Indeed, while the accuracies of parameters that do not accumulate with  $N_{\text{cyc}}$  (such as  $\ln D_L$ ) is only  $1/\text{SNR} \sim 10^{-2}$ , the final chirp-mass accuracy is  $10^{-8}$  augmented significantly by  $\sim N_{\text{cyc}}$ .

As shown in the first four panels of Fig. 2.3, however, the chirp-mass accuracy does not improve closely (or linearly) with  $\text{SNR} \cdot N_{\text{cyc}}$ . Only at the end of a year-long measurement, the accuracy grows significantly and becomes close to the expectation. Here, it is the interplay of low-frequency and highest-frequency regimes that allows to fully realize the potential enhancement from  $N_{\text{cyc}}$ . We discuss this in this section.

The relevance of  $N_{\text{cyc}}$  can be read directly from the Fisher matrix element. The Fisher element of the chirp-mass part,  $F_{\ln \mathcal{M} \ln \mathcal{M}} = \int df |d\tilde{h}/d \ln \mathcal{M}|^2$ , is given by

$$\frac{d\tilde{h}(f)}{d \ln \mathcal{M}} \simeq -\frac{5i}{4}(8\pi \mathcal{M} f)^{-5/3} \tilde{h}(f), \quad (2.12)$$

at the Newtonian order. The term in the first parenthesis is proportional to the  $N_{\text{cyc}}$  accumulated in each frequency interval as

$$N_{\text{cyc}} \approx 2.44 \times 10^7 \left( \frac{\mathcal{M}_z}{1.5 M_\odot} \right)^{-5/3} \left( \frac{f_i}{10^{-1} \text{Hz}} \right)^{-5/3}, \quad (2.13)$$

where the initial frequency  $f_i \ll f_f$  is assumed to be much smaller than the final frequency  $f_f$ . The final term  $\tilde{h}(f)$  in Eq. (2.12) is proportional to the SNR accumulated in that interval. Thus, the Fisher element in each frequency interval is indeed related to the  $N_{\text{cyc}} \cdot \text{SNR}$  there.

The most of the GW cycles is accumulated at low frequencies (see Eq. (2.13)) as GW spends much more time there than at high frequencies. So does SNR. These behaviors are shown in Fig. 2.3. Thus, a long period of particular waveform evolution at low-frequencies contains a large amount of information of the chirp mass. But

a problem remains in that low-frequency data alone is not enough to confidently distinguish the chirp mass from other source parameters. The unresolved correlations with other parameters prohibit to achieve the expected accuracy yet.

Here comes the highest-frequency data, chirping rapidly towards the merger. There, the frequency evolves most rapidly, whose evolution is governed by the chirp mass. Even though  $N_{\text{cyc}}$  does not increase much during that short evolution, the large range of non-trivial frequency evolution can resolve various degeneracies.

In particular, high-frequency measurement significantly improves the accuracy of sky-location  $(\theta, \phi)$  and hence correlations with them (see Fig. 2.3). It is improved due to the huge Doppler phase shift accumulated across the Sun [47] (during year-long measurement). The GW phase explicitly grows with the frequency as

$$\Psi(f) \sim 2\pi f(-\vec{r}_{AU} \cdot \hat{n}/c + t_c), \quad (2.14)$$

where  $\hat{n} = \hat{n}(\theta, \phi)$  is a unit vector for the GW propagation direction or the source's sky-location and  $\vec{r}_{AU}$  is the Earth-Sun separation vector. The first term (depending on  $\theta, \phi$ ) is the Doppler phase shift. But this effect is measurable only after long enough measurement around the Sun [47] as linear (or constant) Doppler shift is not measurable (confused with the cosmological redshift  $z$ ). Thus, a short high-frequency segment of data alone is not useful, but only year-long measurement can utilize this natural benefit. As shown in Fig. 2.3, the location accuracy begins to improve after about 6 months.

The highest-frequency chirping actually improves most of the source-parameter accuracies that affect the GW phase. The coalescence time  $t_c$  will be obviously better determined as GW approaches that time (and see Eq. (2.14) that the  $t_c$  contribution also grows with the frequency). Spin-orbit parameter  $\beta$ 's impact on precession and phase evolution will be largest when the binary separation is smallest near merger. The reduced mass  $\mu$  will receive similar (although smaller) benefits that the chirp

mass receives. On the other hand, the source parameters that affect GW amplitudes do not gain high-frequency benefits, as Fig. 2.3 shows for  $\ln D_L$  accuracy.

By comparing the full results (red-solid) and blue-dashed lines in Fig. 2.3 where we ignore the 5 aforementioned correlations (with sky-location  $(\theta, \phi)$ ,  $t_c$ ,  $D_L$ , and  $\beta$  from *a posteriori* (optical) information), we conclude that the resolution of degeneracies is responsible for the improvement of chirp-mass accuracy at the highest-frequency end. And it is the one that finally allows to realize the potential enhancement from  $N_{\text{cyc}}$ .

### 2.7.2 DM density dependence

The DM density dependence of the signal significance is an interesting property. If NS-NS formation follows the star formation history, then the majority of NS-NS will reside in the galactic center (GC) where DM is also most abundant. NS-NS is then a natural candidate to detect large DM effects. The DM density dependence can also be exploited to better confirm the DM origin of anomalous signals or to map DM distribution.

In this paper, we implicitly assume that the GC is transparent to the GW. But how bright or transparent it is would be an interesting question. Note that the majority of pulsars measured (with lights) and used in PTA [31,32] are within about kpc from the Earth. Thus, NS-NS with the GW can also be complementary to the local fuzzy DM search by Parkes PTA [32] too.

## 2.8 Conclusion

We have shown that last years of NS-NS inspiral may have a precision capability to detect tiny perturbations from the lightest possible scalar DM. The new observable considered is the time-oscillating mass shift, induced by the DM fifth force with long coherence. The precision capability stems from a large number of GW cycles and year-

long measurement of highest frequencies, which can be realized by a future detector network in the broadband  $f \simeq 0.01 - 1000$  Hz. If light scalar DM interacts with the NS, our new observable in this broadband measurement can probe a large part of the unconstrained parameter space, in particular the lightest possible mass range.

Our study also emphasizes the role of long-time high-frequency measurements in the precision GW program; a large  $N_{\text{cyc}}$  can enhance the chirp-mass sensitivity as discussed, and moreover, the Doppler effect around the Sun can localize the source [47, 53], and a better frequency resolution can resolve the GW lensing fringe generated by intervening cosmic strings [117] and compact DM [89] (see also [56, 57] for other benefits). These shall motivate the development of mid-frequency ( $f \simeq 0.01 - 10$  Hz) detectors that can form such broadband detector networks by combining with ongoing or upcoming LIGO-band detectors.

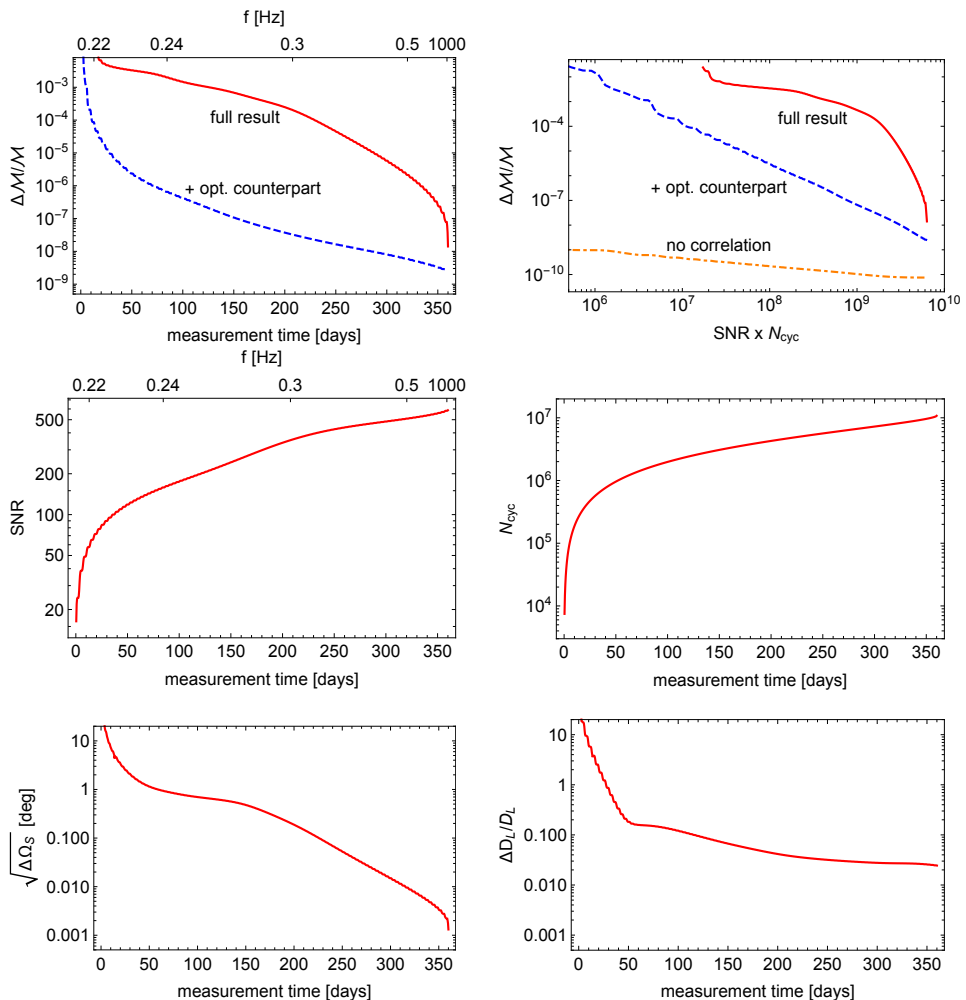


Figure 2.3 Improvement of Fisher errors in measurement time. NS-NS at 10 Mpc. Shown parameters are chirp-mass fractional accuracy, SNR,  $N_{\text{cyc}}$ , sky-localization accuracy, and  $D_L$  fractional accuracy. The second plot shows the correlation of chirp-mass accuracy and  $\text{SNR} \times N_{\text{cyc}}$ . The considered measurement is for the last 1 year, sweeping  $f \simeq 0.22 - 1000$  Hz. The blue-dashed lines assume no correlations with the 5 source parameters (see text for details), and the orange-dotdashed line assumes no correlation with any source parameters.



## Chapter 3

# Small-scale shear: peeling off diffuse subhalos with gravitational waves

This chapter was posted on **arXiv** as *Small-scale shear: peeling off diffuse subhalos with gravitational waves. arXiv:2103.08618 [astro-ph.CO]*.

### 3.1 Introduction

Cold Dark Matter (CDM) hypothesis has successfully explained large-scale structures of the universe, providing firm evidences of DM. But, DM was never detected directly, and its properties in smaller scales are not yet well established. For decades, there has been missing satellites problem [58, 59], where the observed number of luminous satellite galaxies is smaller than the prediction, although CDM predicts numerous structures – (sub)halos – at the subgalactic scale. Recently, it was argued that the completeness correction of star formation and detection efficiencies may resolve the discrepancy [60, 61]. Many new observations of satellite galaxies since then by DES, PANSTARRS1, and Gaia [61, 62] are indeed making a better agreement down to (star-

forming limit)  $M \gtrsim 10^7 - 10^8 M_\odot$ .

Much further can be progressed by searching for DM subhalos below  $10^7 - 10^8 M_\odot$ . Above all, such light subhalos do not harbor star formation [63, 64], hence free of baryonic physics and keeping pristine nature of DM. Their number abundance, mass profile, and spatial distribution can all be important information of underlying DM models [65]; warm, fuzzy, and axion DM models, let alone primordial black holes, predict significant deviations here [61, 66, 67]. They can also test CDM and missing satellites problem more confirmly [65, 68]. Lastly, they might be numerous around us, affecting local direct detection.

However, the searches are challenging. First, they are dark (no stars). Second, they are diffuse in mass profile (no cooling and contraction by baryons) so that their gravitational effects are also suppressed; often too diffuse to produce strong-lensing images or Einstein arcs. In addition, NFW profile [69] is known to fit simulations and galactic-scale observations, but its validity at small scales is also not established. Core-vs-cusp may be another relevant problem about the central mass profile [68, 70, 71].

Existing searches mainly rely on milli-lensing perturbations by subhalos. When one of the strong-lensed images (of compact sources such as quasars) or an arc (of spatially extended sources such as galaxies) is near a subhalo, its flux, shape, location, and arrival time can be milli-lensing perturbed so that different from those of the other images or the other part of the arc [72] (see also [73–79] and refs therein). With excellent imaging spatial resolution, this method can detect subhalos individually [80], but only heaviest ones down to  $M \gtrsim 10^7 - 10^8 M_\odot$  for NFW [81] (and similarly for pseudo-Jaffe [81–84]). The sensitivity is lower limited in part but inherently by profile diffuseness; NFW is so diffuse that milli-lensing cross-section  $\sigma_l \propto M_{\text{NFW}}^{2.5-5}$  scales rapidly with the mass, as estimated in Appendix A.1. (For comparison, compact DM can be probed down to very small masses with lensing [85–95].) Alternatively, a mass

function [96–100] or power spectrum [101–103] can be extended below this range, through the collective or statistical effects of subhalos; the mass abundance inferred in this way also agrees better with CDM in the range  $10^6 - 10^9 M_\odot$  [66, 67, 104, 105]. In all, to search for individual (sub)halos below  $10^7 M_\odot$ <sup>1</sup>, we need a very different method.

Recently, it has been proposed that diffractive lensing of chirping GWs can be used to probe relatively light pseudo-Jaffe subhalos of  $M_{\text{vir}} \lesssim 10^6 M_\odot$  (more precisely,  $M_E = 10^2 - 10^3 M_\odot$ , where  $M_E$  is the mass within the Einstein radius) [110]. As will be discussed throughout this paper, the chirping GW is an ideal object to probe such subhalos; first because its Fresnel length coincides with the scale radii of such profiles [111, 112]; the frequency chirping is so well under theoretical control that it can be used for precision measurements; and it is highly coherent, generated from an almost point source, retaining diffraction pattern. The same physics has also been used to search for compact DM such as primordial black holes [88, 89, 113–115] and cosmic strings [116, 117]. These works have pioneered diffractive lensing near the Einstein radius,  $r_E$ , but NFW is more diffuse with essentially zero  $r_E$  (see Sec. 3.3.2). Not only is it difficult to calculate their diffractive lensing even numerically, but also not clear which scales are relevant and how strong lensing will be.

In this paper, we develop a general formalism for diffractive lensing and work out the GW lensing by a single NFW halo, both analytically and numerically (see Refs. [118, 119] for some numerical results). GW diffraction has been already proposed to measure the matter power spectrum that includes NFW halos at small scales  $1 - 10^4 M_\odot$  [111, 112] or solar-mass microlens populations [120, 121]. But focusing on individual lens, we aim to assess the prospects of individual detection and profile

---

<sup>1</sup>We note that searches using star kinematics [62, 106–109] are also limited by  $\gtrsim 10^8 M_\odot$ , similarly to the milli-lensing. Perhaps, it is partly because both rely on presumably similar size  $\sim 10\%$  of gravitational perturbations. But the similar threshold of star-forming galaxies  $\gtrsim 10^7 - 10^8 M_\odot$  might be a coincidence.

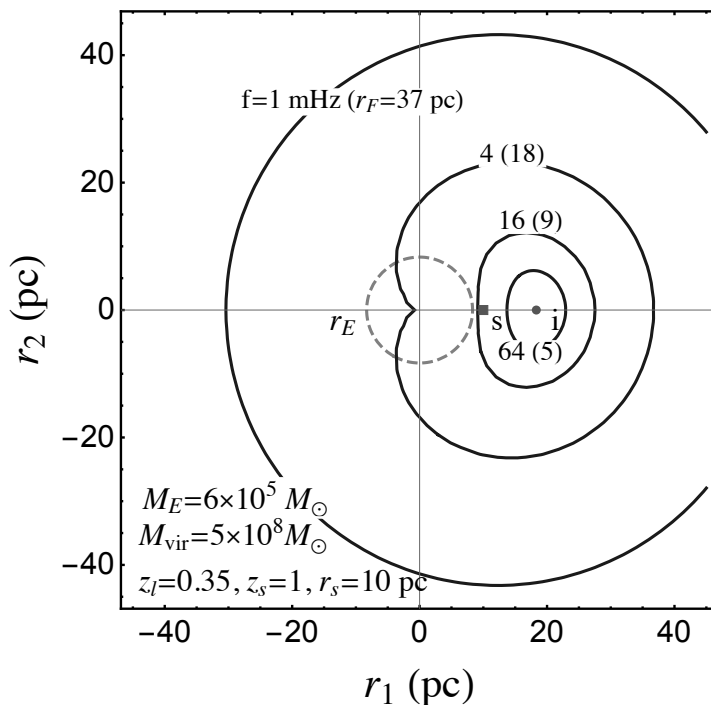


Figure 3.1 Illustrating how the chirping GW detects a diffuse subhalo and successively peels off its profile. The solid circles with radii  $\sim$  Fresnel length  $r_F \propto 1/\sqrt{f}$  are the points on the lens plane being probed by the wave with frequency  $f$ ; also where the phase difference with an image “i” is 1. As the frequency chirps, the circle shrinks and the wave feels the mass distribution at successively smaller scales, hence frequency-dependent diffractive lensing essentially due to *shear*. When  $r_F \lesssim r_s$ , the source “s” begins to be well located/imaged by Fermat principle, hence frequency-independent geometric optics. SIS is used for illustration, where mass is densely distributed within the Einstein radius  $r_E$  which is also a boundary between weak and strong diffraction. NFW is more diffuse with essentially zero  $r_E$ .

measurements. Along the line, our formalism provides easier description in terms of 2D potentials as well as basic understanding of qualitatively different regimes of diffractive lensing. Some of the main underlying physics is illustrated in Fig. 3.1 and will be discussed throughout.

We start by developing general formalism in Sec. 3.2, then we solve NFW diffractive lensing in Sec. 3.3, introduce and quickly estimate the GW lensing detection in Sec. 3.4, and present numerical results of detection prospects in Sec. 3.5. We demonstrate the application of our formalism to more general profiles in Sec. 3.6. We close by summarizing the results in Sec. 3.7.

## 3.2 Diffractive lensing formalism

We develop general formalism for diffractive lensing.

### 3.2.1 Lensing integral

Gravitational lensing effects are captured generally by a complex amplification factor  $F(f)$  as

$$\tilde{h}_L(f) = F(f)\tilde{h}(f), \quad (3.1)$$

where  $\tilde{h}$  ( $\tilde{h}_L$ ) is an unlensed (lensed) waveform in the frequency  $f$  domain. The amplification is calculated by Kirchhoff path integral on the lens plane as [122]

$$F(f) = \frac{f(1+z_l)}{id_{\text{eff}}} \int d^2\mathbf{r} \exp[i2\pi f(1+z_l)T_d(\mathbf{r}, \mathbf{r}_s)], \quad (3.2)$$

where  $\mathbf{r}$  is the physical displacement on the lens plane with its origin at the center of the lens,  $\mathbf{r}_s$  the source position projected onto the lens plane,  $T_d$  the arrival-time difference between the deflected path passing  $\mathbf{r}$  under the lens influence and a straight path in the absence of the lens, and  $d_{\text{eff}} = d_l d_{ls}/d_s$  is the effective angular-diameter distance to the lens.

It is convenient to normalize dimensionful parameters by a characteristic length scale  $r_0$

$$F(w) = \frac{w}{2\pi i} \int d^2\mathbf{x} \exp \left[ iw\hat{T}_d(\mathbf{x}, \mathbf{x}_s) \right], \quad (3.3)$$

where  $\mathbf{x} = \mathbf{r}/r_0$ ,  $\mathbf{x}_s = \mathbf{r}_s/r_0$ ,  $\hat{T}_d = d_{\text{eff}}T_d/r_0^2$ , and

$$w \equiv 2\pi f(1 + z_l) \frac{r_0^2}{d_{\text{eff}}} \quad (3.4)$$

is the dimensionless frequency. The dimensionless time-delay  $\hat{T}_d$ , also called the Fermat potential, is

$$\hat{T}_d(\mathbf{x}, \mathbf{x}_s) = \frac{1}{2}|\mathbf{x} - \mathbf{x}_s|^2 - \psi(\mathbf{x}). \quad (3.5)$$

The first term denotes the geometric time-delay and the second the Shapiro delay with dimensionless potential  $\psi$  being the solution of two-dimensional Poisson equation

$$\nabla_{\mathbf{x}}^2 \psi = 2\kappa(\mathbf{x}) = \frac{2\Sigma(\mathbf{x})}{\Sigma_{\text{crit}}}, \quad (3.6)$$

with the surface density projected onto the lens plane

$$\Sigma(\mathbf{x}) = \int_{-\infty}^{\infty} dz \rho(z, \mathbf{x}), \quad \Sigma_{\text{crit}} = \frac{1}{4\pi d_{\text{eff}}}. \quad (3.7)$$

The convergence  $\kappa(\mathbf{x})$  is the normalized surface density, characterizing lensing strength.

The formalism so far is general and scale invariant. The normalization  $r_0$  can be chosen to be any convenient scale of the lens. For example, the Einstein radius  $r_E = \sqrt{4M_E d_{\text{eff}}}$  is a convenient choice of  $r_0$  for a point-mass lens because its enclosed Einstein mass  $M_E$  is the total mass  $M$  so that  $w = 8\pi M f$  is a simple function of  $M$ . Thus, such a choice is often used for strong lensings (see Sec. 3.6 for the usage for power-law profiles).

For diffuse lenses such as NFW, which rarely induce strong lensing, it is more intuitive and useful to rewrite  $w$  in Eq. (3.4) in terms of a new length scale  $r_F$  such that

$$w = 2 \left( \frac{r_0}{r_F} \right)^2. \quad (3.8)$$

The new scale defined as [111, 123]

$$r_F \equiv \sqrt{\frac{d_{\text{eff}}}{\pi f(1+z_l)}} \simeq 1.76 \text{ pc} \sqrt{\frac{1}{1+z_l} \left( \frac{d_{\text{eff}}}{\text{Gpc}} \right) \left( \frac{\text{Hz}}{f} \right)}, \quad (3.9)$$

is equivalent to the Fresnel length of diffraction applied to lensing. We will use  $r_F$  throughout this paper, discussing its meaning and usefulness in later sections.

Usual geometric-optics lensing is obtained for  $w\hat{T}_d \gg 1$  from the stationary points of  $\hat{T}_d$ , hence Fermat principle.

### 3.2.2 Diffraction condition

Diffraction lensing, also called wave-optics lensing, is the lensing in the regime where Fermat principle does not lead to clear discrete paths of waves from Kirchhoff path integral. It is where the wave properties of a probe wave becomes relevant. This typically produces a single blurred image of a source when  $r_s \gg r_E$ . But for  $r_s \lesssim r_E$ , would-be multiple images may not be well resolved and interfere; such is also referred to as wave-optics effect [89, 91, 113, 124]. In this subsection, we derive conditions for diffractive lensing.

Fermat principle applies when the phase oscillation among the paths passing different parts of the lens plane is rapid enough, i.e.  $2\pi f T_d \gg 1$  near  $r_s$  in Eq. (3.2). Thus, diffractive lensing occurs when, in terms of  $w$  in Eq. (3.3),

$$w\hat{T}_d \simeq w \frac{x_s^2}{2} \lesssim 1, \quad (3.10)$$

where the approximate equality holds if  $r_s \gg r_E$  so that the  $\psi$  contribution to  $\hat{T}_d$  in Eq. (3.5) is negligible compared to the geometric contribution.

Diffractive lensing can also be understood by the analogy with single-slit experiment. The shadow of a slit is blurred when light rays propagating from opposite edges of the slit interfere weakly. This happens when the phase difference between them,  $2\pi(\sqrt{a^2 + d^2} - d)/\lambda \sim \pi a^2/(\lambda d) = (a/r_F)^2$ , is small [125]; here,  $a$ ,  $d$ , and  $\lambda$  are the

slit size, the distance between the slit and the screen, and the wavelength of incident light, respectively. In gravitational lensing,  $a$  and  $d$  are replaced by  $r_s$  (single-imaged cases) and  $d_{\text{eff}}$ , respectively. Thus, diffractive lensing occurs if

$$r_F^2 \gtrsim r_s^2, \quad (3.11)$$

which is equivalent to Eq. (3.10) with the definition of  $w$  in Eq. (3.8). The condition in this form means that as chirping  $r_F$  falls below  $r_s$ , the source becomes well located and only the lens mass profile near the source direction begins to matter; see Fig. 3.1 and Sec. 3.2.5.  $r_F$  is essentially an effective source size [112], within which effects are smeared/interfered out.

The diffraction picture is refined when  $r_s \lesssim r_E$  (or,  $r_s$  near any caustic) so that a lens system can have multiple images. The deflection potential  $\psi$  now significantly contributes to  $\Delta\hat{T}_d$ . A more appropriate diffraction condition is  $2\pi f\Delta T_{ij} \lesssim 1$  or  $w\Delta\hat{T}_{ij} \lesssim 1$  (rather than Eq. (3.10)), where  $\Delta T_{ij}$  is the arrival-time difference between the  $i$ -th and  $j$ -th images [113]. Since typical  $\Delta T_{ij} \sim 4M_E = r_E^2/d_{\text{eff}}$  (equivalently,  $\Delta\hat{T}_{ij} \sim 1$  with  $r_0 = r_E$ ), the condition becomes  $r_F^2 \gtrsim r_E^2$  (cf. Eq. (3.11)). Applied to the point-mass lensing, the condition leads to a well-known interference relation  $\lambda \gtrsim 2\pi R_{Sch}$  between the probe wavelength  $\lambda$  and the lens Schwarzschild radius  $R_{Sch} = 2M$ , as  $r_E^2/r_F^2 = (4Md_{\text{eff}})/(\lambda d_{\text{eff}}/\pi) = 4\pi M/\lambda \lesssim 1$ . Thus, this relation is nothing but the requirement for the wave to see the lens (or the slit in the single-slit analogy), or equivalently for the interference between multiple images to be relevant [89, 91, 113, 124].

Wave properties (hence, frequency dependencies) remain important inside  $r_E$  up until  $r_F \gtrsim 2\sqrt{r_E r_s}$ . Consider  $x_s \rightarrow 0$  near a caustic. The would-be multiple images have very small relative time-delays,  $\Delta\hat{T}_d = 2x_E x_s + \mathcal{O}(x_s^2)$  (derived in Appendix A.2), as they are formed almost symmetrically around the corresponding critical lines (in this case, the Einstein radius  $x_E$ ). Only if the frequency is very large, the result-



ing interference becomes so rapid that geometric optics is reached. Thus, diffraction continues well inside the Einstein radius until

$$w \lesssim \frac{1}{2x_E x_s} \quad \leftrightarrow \quad r_F \gtrsim 2\sqrt{r_E r_s}. \quad (3.12)$$

Diffraction inside  $r_E$  is strong lensing, and it produces a blurred Einstein ring, which becomes sharper as  $r_F$  decreases toward this limit, eventually separated into clear images.

In all, Eq. (3.10) or (3.11) is a relevant diffraction condition for NFW (Sec. 3.3.2). But  $r_E$  and strong diffractive lensing with Eq. (3.12) can also be relevant to general diffuse profiles (Sec. 3.6). In next subsections, we formulate diffractive lensing and see how these physics arise.

### 3.2.3 Formalism for weak diffractive lensing

We solve Eq. (3.3) for *weak diffractive lensing*, in terms of much simpler 2D projected potentials. This formalism is applicable to any single lens profiles without symmetries. Weak lensing will be relevant to NFW.

In the diffraction regime  $r_F \gtrsim r_s$ , it is convenient to ignore  $x_s$  (effectively, not well resolved) so that Eq. (3.3) is rewritten as

$$F(w) \simeq \frac{w}{2\pi i} \int d^2 \mathbf{x} \exp \left[ i w \left( \frac{1}{2} |\mathbf{x}|^2 - \psi(\mathbf{x}) - T_0 \right) \right]. \quad (3.13)$$

$T_0$  is the overall time-delay in the geometric-optics limit relative to the unlensed case;  $F(w)$  now contains only the relative time delays among diffracted rays. We will see later what  $T_0$  means for both single- and multi-imaged cases.

For weak diffraction with small  $\psi$  (more precisely, when Shapiro delay is subdominant or  $r_s \gtrsim r_E$ ), the Born approximation leads to the expansion

$$F(w) \simeq 1 - \frac{w^2}{2\pi} \int d^2 \mathbf{x} e^{\frac{1}{2} i w |\mathbf{x}|^2} (\psi(\mathbf{x}) - \psi(0)) , \quad (3.14)$$

where  $T_0 \simeq -\psi(0)$  for weak lensing. Using the integration by parts (with  $iwx e^{iwx^2/2} = \frac{d}{dx}(e^{iwx^2/2})$ ), Eq. (3.14) can be written as

$$F(w) \simeq 1 + \frac{w}{i} \int_0^\infty dx x e^{iwx^2/2} \bar{\kappa}(x), \quad (3.15)$$

where  $\bar{\kappa}(x)$  is the *mean convergence* within the aperture of radius  $x$  centered at  $\mathbf{x}_s$  as [126]

$$\begin{aligned} \bar{\kappa}(x) &\equiv \frac{1}{\pi x^2} \int_{|\mathbf{x}'| < x} d^2 \mathbf{x}' \kappa(\mathbf{x}') \\ &= \frac{1}{2\pi x} \int_0^{2\pi} d\phi' \frac{\partial}{\partial x} \psi(x, \phi') \end{aligned} \quad (3.16)$$

with the lens-plane polar coordinate  $(x, \phi)$ .

Furthermore, important physics is contained in the frequency dependence of  $F(w)$ . By differentiating Eq. (3.16),

$$\langle \gamma_t(x) \rangle \equiv \frac{1}{2\pi} \int_0^{2\pi} d\phi \gamma_t(x, \phi) = -\frac{1}{2} \frac{d\bar{\kappa}(x)}{d \ln x}, \quad (3.17)$$

where  $\gamma_t$  is the tangential shear

$$\gamma_t(x, \phi) = \frac{1}{2} \left[ \frac{1}{x} \frac{\partial \psi}{\partial x} - \frac{\partial^2 \psi}{\partial x^2} + \frac{1}{x^2} \frac{\partial^2 \psi}{\partial \phi^2} \right]. \quad (3.18)$$

Using Eq. (3.17), the differentiation of Eq. (3.15) with respect to  $\ln w$  can be written in terms of shear

$$\frac{dF(w)}{d \ln w} = \frac{w}{i} \int_0^\infty dx x e^{iwx^2/2} \langle \gamma_t(x) \rangle. \quad (3.19)$$

Finally and remarkably, although Eqs. (3.15) and (3.19) are already new and insightful results of this work, they can be more usefully simplified as

$$F(w) \simeq 1 + \bar{\kappa} \left( \frac{1}{\sqrt{w}} e^{i\frac{\pi}{4}} \right) \quad (3.20)$$

$$\frac{dF(w)}{d \ln w} \simeq \left\langle \gamma_t \left( \frac{1}{\sqrt{w}} e^{i\frac{\pi}{4}} \right) \right\rangle, \quad (3.21)$$

in that the dominant support of the integral  $\int_0^\infty dx x e^{iwx^2/2}$  is near  $x = \frac{1}{\sqrt{w}} e^{i\pi/4}$ , which can be obtained by rotating the half real-line integration by  $e^{i\pi/4}$ . The phase factor in the support is crucial to make this single region a dominant contributor. These are good approximations as long as  $\bar{\kappa}(x)$  and  $\langle \gamma_t(x) \rangle$  do not vary rapidly near the support.

Eqs. (3.20) and (3.21) are one of the new and main results of this paper. The fact that complicated lensing integral is evaluated by much simpler 2D potentials is not only very convenient in estimating and understanding diffractive lensing, but also has various implications. Such utilities and implications will be discussed and demonstrated throughout this paper.

Before moving on, we discuss the formalism in more detail. First,  $F(w)$  is a complex quantity, containing information on both amplification  $|F(w)|$  and phase  $\varphi(w)$  (or interferences). For small  $\psi$ , one can decompose as [111]

$$|F(w)| \simeq \text{Re}[F(w)] = 1 + w \int_0^\infty dx x \sin \frac{wx^2}{2} \bar{\kappa}(x), \quad (3.22)$$

$$\varphi(w) \simeq \text{Im}[F(w)] = -w \int_0^\infty dx x \cos \frac{wx^2}{2} \bar{\kappa}(x), \quad (3.23)$$

and

$$\frac{d|F(w)|}{d \ln w} \simeq \text{Re} \left[ \frac{dF(w)}{d \ln w} \right] = w \int_0^\infty dx x \sin \frac{wx^2}{2} \langle \gamma_t(x) \rangle, \quad (3.24)$$

$$\frac{d\varphi(w)}{d \ln w} \simeq \text{Im} \left[ \frac{dF(w)}{d \ln w} \right] = -w \int_0^\infty dx x \cos \frac{wx^2}{2} \langle \gamma_t(x) \rangle. \quad (3.25)$$

The frequency dependences of amplification and phase are of the same order and governed commonly by shear. Both physics must be utilized for detection and precision measurements.

Up to this point, no assumptions on  $\psi$  were made except for its smallness. For axisymmetric profiles considered in this paper, the angular dependence is trivial so

that 2D identities are simplified as

$$\bar{\kappa}(x) = \frac{1}{x} \psi'(x), \quad (3.26)$$

$$\langle \gamma_t(x) \rangle = \gamma(x) = \frac{1}{2} \left[ \frac{1}{x} \psi'(x) - \psi''(x) \right]. \quad (3.27)$$

From here on, we will drop the subscript ‘t’ for shear. Thus, we arrive at final formula for an axisymmetric lens

$$F(w) \simeq 1 + \frac{w}{i} \int_0^\infty dx x e^{i w \frac{x^2}{2}} \bar{\kappa}(x) \simeq 1 + \bar{\kappa} \left( \frac{1}{\sqrt{w}} e^{i \frac{\pi}{4}} \right), \quad (3.28)$$

$$\frac{dF(w)}{d \ln w} \simeq \frac{w}{i} \int_0^\infty dx x e^{i w \frac{x^2}{2}} \gamma(x) \simeq \gamma \left( \frac{1}{\sqrt{w}} e^{i \frac{\pi}{4}} \right). \quad (3.29)$$

### 3.2.4 Shear as the origin of frequency dependence

The most remarkable meaning of Eq. (3.21) or (3.29) is that the origin of the frequency dependence is (1) ‘shear’ of a lens, (2) at frequency-dependent  $x \simeq 1/\sqrt{w}$  or  $r \simeq r_F/\sqrt{2}$ .

Why does this make sense? Shear, defined in Eq. (3.27), is produced from asymmetric mass distributions, hence distorting the shapes of background galaxies. But it also reflects how steeply a profile varies at a given point. Consider the expression in the form

$$\gamma(x) = \bar{\kappa}(x) - \kappa(x), \quad (3.30)$$

derived from Eqs. (3.26) and (3.27) and  $\kappa(x) = \frac{1}{2} \nabla^2 \psi(x) = \frac{1}{2} (\psi'(x)/x + \psi''(x))$  for axisymmetric cases. Note that  $\bar{\kappa}(x)$ , hence  $\gamma(x)$ , does not necessarily vanish even though density  $\kappa(x) \propto \Sigma(x)$  may vanish there. So this form makes it clear that the variation of the potential is the one that produces shear, except at the spherically symmetric point (as a component of the Weyl conformal curvature tensor [127,128]).

Further, Eqs. (3.28) and (3.29) are consistent with Gauss’ theorem: gravitational effects must depend only on the enclosed mass. The enclosure boundary in our prob-

lem is given by the diffraction length scale  $r_F \propto f^{-1/2}$ . Thus, as the frequency grows, the boundary shrinks and the enclosed mass changes; see Fig. 3.1 for illustration. The change of lensing effects as a function of frequency thus must be related to the variation of the mass or potential at the boundary, which is given by shear.

Nevertheless, geometric optics is frequency independent. As  $r_F \lesssim r_s$  or  $2\sqrt{r_E r_s}$ , the source is well resolved, and Fermat principle determines image properties solely from  $\hat{T}_d$  in the narrow region around the image. This will be further discussed in the next subsection. In reality, a mass profile may contain several substructures at various scales of their own small curvatures. If we probe this profile with a broad range of  $r_F$ , every time  $r_F$  crosses this scale of a substructure, there appears wave-optics effect perturbing and correcting the image properties accounting for the substructure influence.

Eq. (3.29) offers a new concrete way to measure the mass profile. The measurement of  $dF(w)/d\ln w$  for a range of  $w$  (even from a single GW event) can be directly translated to the measurement of the shear field  $\gamma(x)$  for the corresponding length range; recall that  $F(w)$  cannot be measured directly. Just as the shear field measured from galaxy shape distortions are used to measure the mass of a lens galaxy cluster, the shear field from GW diffraction (this time even with a single event) can tell the lens mass profile. In Sec. 3.6.3, we apply our formalism to briefly demonstrate this physics potential.

Practically, Eq. (3.29) allows to estimate diffractive lensing much more easily. Kirchhoff integral is usually very difficult to calculate even numerically, but 2D projected potentials are much easier. In the following sections, we work out NFW diffractive lensing both analytically and numerically, not only confirming our formalism but also showing how readily one can estimate diffractive lensing.

### 3.2.5 Complete formalism with strong diffraction

When the Einstein radius of a lens can be comparable to the  $r_F$  of chirping GWs, *strong diffractive lensing* which is qualitatively different from the weak diffractive lensing must be taken into account. As derived in Eq. (3.12), strong diffractive lensing occurs if  $2\sqrt{r_E r_s} \lesssim r_F \lesssim r_E$ . Given the condition, one can show that the main contributions to the lensing integral Eq. (3.3) arises at  $x \simeq x_E$ , i.e. the Einstein ring. Using the stationary phase approximation at  $x = x_E$ , Eq. (3.3) is evaluated as

$$F(f) \simeq i^{-\frac{1}{2}} x_E \sqrt{\frac{2\pi w}{1 - \kappa(x_E) + \gamma(x_E)}}, \quad (3.31)$$

which is again expressed in terms of  $\kappa$  and  $\gamma$ , this time at  $x = x_E$ .

Interestingly, the frequency dependence  $F(f) \propto w^{1/2}$  of strong diffractive lensing is universal to all axisymmetric lenses. This can be intuitively understood from the shape of an Einstein ring, which is produced since  $r_s$  is negligible. By diffraction effect, the ring is blurred so that it looks like an annulus with thickness  $\sim r_F$  and radius  $\sim r_E$ . Then, one can expect Eq. (3.3) to be  $F(f) \propto r_F^{-2} \times (\text{area of the annulus}) \propto r_E r_F^{-1} = x_E \sqrt{w}$ , and this is exactly as in Eq. (3.31).

The situation was different in the weak diffraction regime, where  $F(f)$  directly connects to the lens profile through  $\bar{\kappa}$  and  $\gamma$  at  $x \simeq r_F$ . What is the origin of the difference between the two diffraction regimes? It is due to the approximate scale invariance in the weak diffraction regime; no length scales up to weak gravitational potential  $\psi$ . In contrast to strong diffractive lensing, the weak lensing integral is dominated by a disk with radius  $r_F$  centered at the origin. By the similar argument, one might expect  $F(f) \propto r_F^{-2} \times r_F^2 \propto \text{const}$ , which looks at first inconsistent with Eqs. (3.28) and (3.29), but is just a manifestation of a scale invariance. The existence of  $\psi$  corrects this perturbatively. Note that  $F(f)$  is invariant under the scale transform  $x \rightarrow \lambda x$  and  $w \rightarrow \lambda^{-2} w$  if there were no lens. Since the symmetry is broken by  $\psi$ , we

keep track of the effects by a spurion coupling  $a\psi$  that compensates the symmetry breaking. For simplicity, by considering a power-law profile  $\psi \propto x^{2-k}$  (Sec. 3.6), the scale invariance  $wax^{2-k} \rightarrow wax^{2-k}$  requires  $a \rightarrow \lambda^k a$ . The leading term of the perturbation expansion (in powers of  $a$ ) of  $F(f)$  must be of the form

$$F(f) = a\psi w^q + \text{const.}, \quad \text{with } q = \frac{k}{2} \quad (3.32)$$

to respect the scale invariance. The power of  $w$  is thus uniquely determined by the spurious scale invariance, and indeed agrees with our power-law calculation in Sec. 3.6.1. On the other hand, in the strong diffraction regime, the Einstein radius fixes the length scale of  $F(f)$  (as a stationary point), and a scale invariance no longer exists. Therefore, the existence of a scale invariance discriminates strong/weak diffractive lensing.

The frequency independence of geometric optics is also explained similarly. In this regime of  $r_F \lesssim \max(r_s^2, 2\sqrt{r_s r_E})$  and  $r_s \neq 0$ , only stationary points of  $\hat{T}_d(\mathbf{x})$  (hence, separate images) contribute to Eq. (3.3). In the small neighborhood of each image, a scale invariance holds and, as a result, the contribution of each image to  $F(f)$  is constant. If there are multiple images,  $F(f)$  also contains the interference between them, which becomes increasingly oscillatory with  $w$ .

As an interesting aside, we can understand the frequency dependences in yet another way. We can derive them just by matching  $F(w)$  to geometric optics at the diffraction boundaries  $r_F = r_s$  Eq. (3.11) and  $r_F^2 = 4r_s r_E$  Eq. (3.12). For weak diffraction, matched at  $r_F = r_s$ , the geometric-optics magnification of the single image at  $r_s$  is

$$F = \sqrt{\frac{1}{(1 - \kappa(r_s))^2 - \gamma(r_s)^2}} \simeq 1 + \kappa(r_s) \quad (3.33)$$

$$= 1 + \frac{2-k}{2} x_s^{-k} = 1 + \frac{2-k}{2} \left(\frac{w}{2}\right)^{\frac{k}{2}} \quad (3.34)$$

where  $\kappa, \gamma \ll 1$  and in the second line we have used power-law results derived in Sec. 3.6. This indeed has  $F-1 \propto w^{k/2}$  as in Eq. (3.32). For strong diffraction, matched at  $r_F^2 = 4r_s r_E$ , the geometric-optics magnification of one of the multi-images located at  $x_i = 1 + \delta x = 1 + x_s/(1 - \psi''(1))$  Eq. (A.8) is ( $\delta x \ll 1$ )

$$F = \sqrt{\frac{1}{(1 - \kappa(x_i)^2) - \gamma(x_i)^2}} \simeq \sqrt{\frac{1}{kx_s}} = \sqrt{\frac{2w}{k}}. \quad (3.35)$$

where again we have used power-law results. This indeed has  $F \propto w^{1/2}$  as in Eq. (3.31); the dependence of  $k^{-1/2}$  is also correct as in Eq. (3.79). Thus, the physics of the wave-to-geometric optics boundary and geometric-optics magnification already contain the  $w$ -dependences.

This completes the formalism of diffractive lensing. In the next few sections, we apply the weak diffraction to NFW, while in Sec. 3.6 we apply the full formalism to general power-law profiles.

### 3.3 NFW lensing

As an important example, we work out diffractive lensing by NFW using our formalism.

#### 3.3.1 Profile

The Navarro-Frenk-White (NFW) profile [69] is commonly used to parametrize spherically symmetric density profiles of CDM halos. With two parameters,  $\rho_0$  and  $r_0$ , its 3-dimensional radial profile is given by

$$\rho(r) = \frac{4\rho_0}{(r/r_0)(1 + r/r_0)^2}, \quad (3.36)$$

where  $r$  is the radial distance from the center,  $r_0$  the scale radius at which the slope of profile turns from  $-1$  inside to  $-3$  outside, and  $\rho_0$  the mass density at  $r_0$ . Since



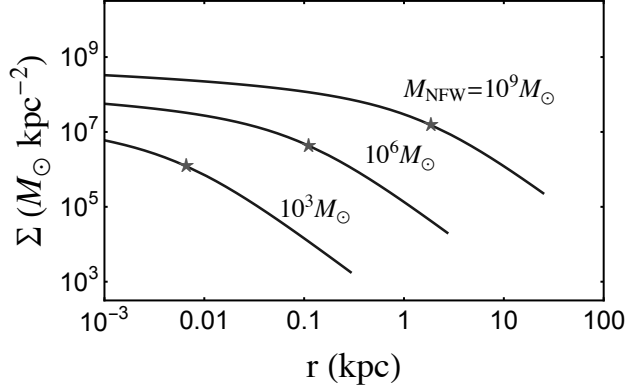


Figure 3.2 The surface mass density  $\Sigma(r)$  at the distance  $r$  from the center of the NFW profile, with  $M_{\text{NFW}} = 10^9, 10^6, 10^3 M_{\odot}$ . The star on each curve denotes the location of the scale radius  $r_0$ . The curves end at their virial radius,  $r_{\text{vir}} = cr_0$ , where  $c$  is given by the Okoli's  $M_{\text{vir}} - c$  relation [130].

the total mass diverges, this profile must be cut off at some  $r$  not far from  $r_0$ ; only the scale  $r \lesssim r_0$  will be relevant to the lensing. The surface density at the distance  $x = r/r_0$  from the center on the lens plane is given by [129]

$$\Sigma(x) = \int_{-\infty}^{\infty} dz \rho \left( \sqrt{x^2 r_0^2 + z^2} \right) = 3\Sigma_0 \frac{1 - \mathcal{F}(x)}{x^2 - 1}, \quad (3.37)$$

where  $\Sigma_0 = 8\rho_0 r_0/3 = \Sigma(x=1)$  and

$$\mathcal{F}(x) = \begin{cases} \frac{\text{arctanh}\sqrt{1-x^2}}{\sqrt{1-x^2}} & x < 1 \\ 1 & x = 1 \\ \frac{\text{arctan}\sqrt{x^2-1}}{\sqrt{x^2-1}} & x > 1 \end{cases} . \quad (3.38)$$

The 2D Poisson equation Eq. (3.6) is solved as

$$\psi(x) = 3\kappa_0 \left[ \ln^2 \frac{x}{2} + (x^2 - 1)\mathcal{F}^2(x) \right], \quad (3.39)$$

where  $\kappa_0 = \Sigma_0/\Sigma_{\text{crit}}$ .

The NFW parameterization is simplified by removing one of the two parameters using the  $M_{\text{vir}} - c$  relation predicted by CDM simulations. Here,  $M_{\text{vir}}$  is the virial mass of a halo, and  $c \equiv r_{\text{vir}}/r_0$  is the concentration. We take the  $M_{\text{vir}} - c$  relation at  $z = 0$  from Okoli et. al. in [130]. Moreover, instead of conventional  $M_{\text{vir}}$ , it is more convenient to use the NFW mass defined as

$$M_{\text{NFW}} \equiv 16\pi\rho_0 r_0^3 \quad (3.40)$$

because it represents the halo mass independently of redshift. The two masses are related by

$$M_{\text{vir}} = M_{\text{NFW}} \left( \ln(1+c) - c(1+c)^{-1} \right), \quad (3.41)$$

differing only by  $\mathcal{O}(1)$  as  $c = 10 \sim 50$  for  $M_{\text{vir}} = 10^4 \sim 10^{10} M_{\odot}$  [130, 131].

Now,  $M_{\text{NFW}}$  fixes all the parameters of NFW profile. For example, we can express most relevant lens properties in terms of  $M_{\text{NFW}}$  as (using central values of the Okoli's relation)

$$\Sigma_0 = \frac{8}{3}\rho_0 r_0 \simeq 1.3 \times 10^7 M_{\odot}/\text{kpc}^2 \left( \frac{M_{\text{NFW}}}{10^9 M_{\odot}} \right)^{0.18}, \quad (3.42)$$

$$r_0 = \sqrt{\frac{M_{\text{NFW}}}{6\pi\Sigma_0}} \simeq 2 \text{ kpc} \left( \frac{M_{\text{NFW}}}{10^9 M_{\odot}} \right)^{0.41}. \quad (3.43)$$

Fig. 3.2 shows the surface mass density  $\Sigma(x)$  and  $r_0$  for  $M_{\text{NFW}} = 10^3, 10^6$ , and  $10^9 M_{\odot}$ .  $\Sigma(r)$  is obviously smaller for lighter halos while not varying rapidly inside  $r_0$ ; thus,  $\Sigma_0 = \Sigma(r = r_0)$  or  $\kappa_0$  characterizes the values of  $\Sigma(x)$  or  $\kappa(x)$ .  $r_0$  is smaller for lighter NFWs, and it is the length scale relevant to this work. We collect other useful expressions too:

$$\kappa_0 = \frac{\Sigma_0}{\Sigma_{\text{crit}}} \simeq 7.9 \times 10^{-3} \left( \frac{M_{\text{NFW}}}{10^9 M_{\odot}} \right)^{0.18} \left( \frac{d_{\text{eff}}}{\text{Gpc}} \right), \quad (3.44)$$

$$\Sigma_{\text{crit}} = \frac{1}{4\pi d_{\text{eff}}} \simeq 1.66 \times 10^9 M_{\odot} \text{kpc}^{-2} \left( \frac{\text{Gpc}}{d_{\text{eff}}} \right). \quad (3.45)$$

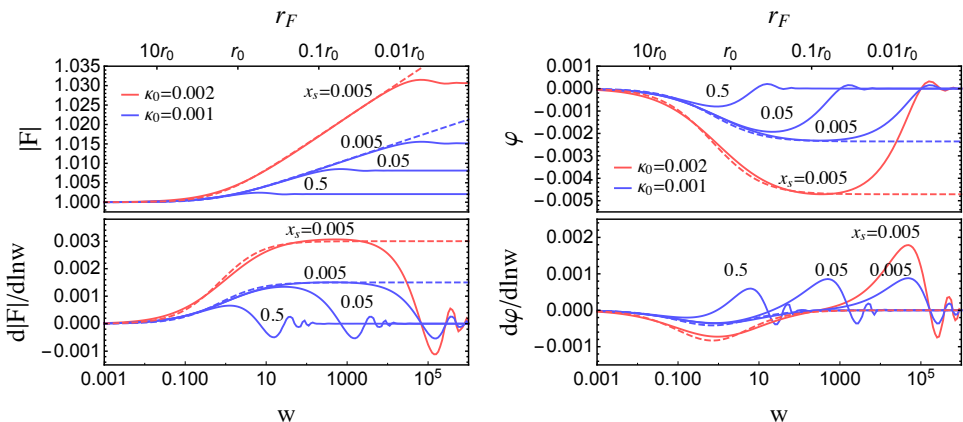


Figure 3.3  $|F(w)|$  (upper left),  $\frac{d|F(w)|}{d \ln w}$  (lower left),  $\varphi(w)$  (upper right), and  $\frac{d\varphi(w)}{d \ln w}$  (lower right) for NFW profiles with  $\kappa_0 = 0.002$  (red) and  $\kappa_0 = 0.001$  (blue). Solid lines are full numerical solutions of Eq. (3.13), while dashed are diffraction-limit results in Eqs. (3.51) and (3.52). Their  $|F(w)|$  and  $\varphi(w)$  are obtained according to Eqs. (3.22~3.25). All of them agree in the diffraction regime  $w \lesssim 2/x_s^2$ ; see more in text. Each curve is marked with  $x_s$  value.

### 3.3.2 Critical curves

Critical curves are the locations of images where their magnifications (formally) diverge. The magnification in the geometric-optics limit

$$\mu = [\det A(\mathbf{x})]^{-1} \quad (3.46)$$

$$= [(1 - \kappa)^2 - \gamma^2]^{-1} = \left[ \left( 1 - \frac{\psi'}{x} \right) (1 - \psi'') \right]^{-1}, \quad (3.47)$$

where  $A(\mathbf{x}) \equiv d\mathbf{x}_s/d\mathbf{x}$  is a  $2 \times 2$  matrix of the  $\hat{T}_d$  curvature around the image, yields two such solutions

$$x_t \simeq 2 \exp \left[ -\frac{1}{2} - \frac{1}{3\kappa_0} \right], \quad x_r \simeq 2 \exp \left[ -\frac{3}{2} - \frac{1}{3\kappa_0} \right], \quad (3.48)$$

called tangential and radial critical curves, respectively.  $x_t$  is also called the Einstein radius  $x_E$ . Since  $\kappa_0 \lesssim 10^{-2}$  is small for NFWs considered in this work, the critical

curves are exponentially suppressed  $x_{t,r} \lesssim \exp(-100) \ll 1$  and  $x_E$  is essentially zero. What does this mean?

Critical curves (more precisely, caustics) are roughly the boundary between regions of different number of images; if  $\det A$  Eq. (3.46) does not turn its sign, then the mapping between source  $\mathbf{x}_s$  and image  $\mathbf{x}$  planes is one-to-one invertible so that there can only be a single image [132]. Also, critical curves are (more precisely, Einstein radius) the boundary between geometric versus Shapiro time-delay dominance. Therefore, NFW lensing is always single-imaged (see also Appendix A.3) and governed by geometric time-delay; leading gravitational effects come from the perturbation of order  $\psi$  near the image. But this is not a general property of diffuse profiles, as will be discussed in Sec. 3.6.1.

How can single-imaged lensing be detected? Again, it is possible by the frequency dependence of diffractive lensing and the frequency chirping of GW.

### 3.3.3 Diffractive lensing

We solve NFW (weak) diffractive lensing analytically. Plugging Eq. (3.39) into Eqs. (3.26) and (3.27), we have

$$\bar{\kappa}(x) = \frac{6\kappa_0}{x^2} \left[ \ln \frac{x}{2} + \mathcal{F}(x) \right], \quad (3.49)$$

$$\gamma(x) = \frac{6\kappa_0}{x^2} \left[ \ln \frac{x}{2} + \mathcal{F}(x) - \frac{x^2}{2} \frac{1 - \mathcal{F}(x)}{x^2 - 1} \right], \quad (3.50)$$

where  $\mathcal{F}(x)$  is given in Eq. (3.38). Then, according to Eqs. (3.28) and (3.29), the analytic continuation of Eqs. (3.49) and (3.50) yields

$$F(w) \simeq 1 - 6\kappa_0 i w \left[ \frac{i\pi}{4} - \frac{1}{2} \ln w - \ln 2 + \mathcal{F}(w^{-\frac{1}{2}} e^{\frac{i\pi}{4}}) \right], \quad (3.51)$$

$$\begin{aligned} \frac{dF(w)}{d \ln w} \simeq & -6\kappa_0 i w \left[ \frac{i\pi}{4} - \frac{1}{2} \ln w - \ln 2 + \mathcal{F}(w^{-\frac{1}{2}} e^{\frac{i\pi}{4}}) \right. \\ & \left. - \frac{i}{2} \frac{1 - \mathcal{F}(w^{-\frac{1}{2}} e^{\frac{i\pi}{4}})}{i - w} \right]. \end{aligned} \quad (3.52)$$

Recall that this derivation is valid for  $r_F \gtrsim r_s$  and  $r_s \gtrsim r_E$ , but since  $r_E$  vanishes for NFW these results are valid for all  $w = 2(r_0/r_F)^2$  as long as  $r_F \gtrsim r_s$ . Although these are complicated functions of  $w$  in general, they are simplified in the limits of  $w \gg 1$  and  $\ll 1$ . For  $w \ll 1$  ( $w \gg 1$ ), they asymptote as  $dF/d\ln w \propto w$  ( $\propto \text{const}$ ), which agrees with the results of  $k \rightarrow 2$  ( $k \rightarrow 0$ ) power-law profiles since these limits correspond to the outer (inner) part of NFW with  $\rho \propto r^{-3}$  ( $r^{-1}$ ).

Fig. 3.3, above all, confirms these analytic solutions (dashed) in the diffractive regime of  $w \lesssim 2/x_s^2$ , compared with full numerical results of Eq. (3.2) (solid). Around this boundary, they are matched well to the well-known geometric-optics results. Therefore, it is remarkable that one can understand the results of complicated lensing integral in terms of much simpler 2D potentials.

Fig. 3.3 further demonstrates the main features of NFW diffractive lensing. In the diffraction regime, both amplification  $|F(w)|$  and phase  $\varphi(w)$  are frequency dependent, as expected. Its strength does not depend on  $x_s$  (i.e.,  $x_s$  not resolved) so that blue curves with different  $x_s$  coincide there. But  $x_s$  determines at which frequency lensing becomes geometric optics (i.e., when  $x_s$  is resolved). As a result, larger lensing effects can be obtained for smaller  $x_s$ ; geometric-optics lensing is stronger for sources closer to the lens. Soon after geometric optics is reached, the slopes of  $|F(w)|$  and  $\varphi(w)$  vanish, and lensing becomes frequency independent. Lastly, single-imaged diffraction always amplifies the wave, as also proved in Appendix A.3.

Notably,  $\varphi(w)$  itself also vanishes in the geometric-optics limit. It is because  $T_0$  was factored out in Eq. (3.13) so that the single image in this limit does not have extra phases; we will see  $\varphi(w)$  for multi-imaged cases in Sec. 3.6. Although the frequency dependence of  $\varphi(w)$  is more complicated than that of  $|F(w)|$ , their overall sizes are anyway similar, commonly given by  $\bar{\kappa}(x)$  and  $\gamma(x)$ .

## 3.4 GW detection of NFW

We introduce the concept of detection with chirping GW and likelihood criteria for detection.

### 3.4.1 GW chirping

One of the most important features of GW is that its amplitude and frequency “chirp”. It is worth emphasizing that what is actually measurable is the frequency-dependent change of lensing effects, not the absolute size of amplification.

The observed unlensed chirping amplitude in the frequency domain can be written as

$$\tilde{h}(f) = A_p A(f) e^{i(2\pi f t_c^0 + \phi_c^0 + \Psi(f))}. \quad (3.53)$$

The chirping  $A(f)$  with particular frequency dependences as described below will be the basis of lensing detection, while the chirping phase  $\Psi(f)$  will be canceled out between lensed and unlensed waveforms (see Eq. (3.57)). Coalescence time  $t_c^0$  and constant phase  $\phi_c^0$  set to zero for the best-fit procedure (see Eq. (3.58)) since they can be arbitrary. For simplicity, we fix binary and detector parameters (polarization, binary inclination, and detector antenna direction) such that  $A_p = 1$ , and ignore black hole spins and detector reorientation during measurements; such effects will in principle be distinguishable from lensing effects. We refer to [89, 110] for more discussions on this simplified analysis.

The frequency dependence of  $A(f)$  differs in the successive phases of inspiral-merger-ringdown. For the inspiral phase  $f < f_{\text{merg}}$ , we adopt PhenomA waveform templates developed in Ref. [133], approximating non-spinning quasi-circular binaries. The waveform is

$$A(f) = A_{\text{insp}}(f) = \sqrt{\frac{5}{24}} \frac{\mathcal{M}_6^{\frac{5}{6}} f^{-\frac{7}{6}}}{\pi^{\frac{2}{3}} d_L}, \quad (3.54)$$

which is the restricted post-Newtonian approximation. The chirp mass  $\mathcal{M} = M_{\text{BBH}}/2^{6/5}$  for equal-mass binaries with the total mass  $M_{\text{BBH}}$  (we consider only such cases), and  $d_L$  is the luminosity distance to the source. All the masses are redshifted ones. The amplitude in the merger ( $f_{\text{merg}} \leq f < f_{\text{ring}}$ ) and ringdown phases ( $f_{\text{ring}} \leq f < f_{\text{cut}}$ ) are

$$A(f) = A_{\text{insp}}(f_{\text{merg}}) \times \begin{cases} \left(\frac{f}{f_{\text{merg}}}\right)^{-2/3} & \text{merger} \\ \frac{\sigma_f^2/4}{(f-f_{\text{ring}})^2 + \sigma_f^2/4} & \text{ringdown} \end{cases}, \quad (3.55)$$

where  $\sigma_f$  is the width of a peak centered at  $f_{\text{ring}}$ . The expressions for  $f_{\text{merg}}$ ,  $f_{\text{ring}}$ ,  $f_{\text{cut}}$ , and  $\sigma_f$  are detailed in Ref. [133]. Example chirping waveforms  $|\tilde{h}(f)|$  based on these expressions are shown in Fig. 3.4. Frequency-dependent lensing effects will be detectable as a deviation to the chirping.

Also marked on the chirping waveforms are the time remaining until final merger. The frequency chirping in time at leading post-Newtonian order is given by

$$f(t) = \frac{1}{8\pi\mathcal{M}} \left(\frac{5\mathcal{M}}{t}\right)^{3/8} = 0.39 \text{ Hz} \left(\frac{M_{\odot}}{M_{\text{BBH}}}\right)^{5/8} \left(\frac{\text{yr}}{t}\right)^{3/8} \quad (3.56)$$

for time  $t$  before final merger. Almost all of the time is spent during the inspiral.

The benchmark GW detectors are Laser Interferometer Space Antenna (LISA) [134, 135], Big Bang Observer (BBO) [136], Matter-wave Atomic Gradiometer Interferometric Sensor (MAGIS) [137, 138], and Einstein Telescope (ET) [139]. Their noise spectral densities  $S_n(f)$  are shown in Fig. 3.4. The sensitivity ranges are roughly  $[10 \mu\text{Hz}, 1 \text{ Hz}]$  (LISA),  $[1 \text{ mHz}, 100 \text{ Hz}]$  (BBO),  $[30 \text{ mHz}, 3 \text{ Hz}]$  (MAGIS), and  $[2 \text{ Hz}, 10 \text{ kHz}]$  (ET).

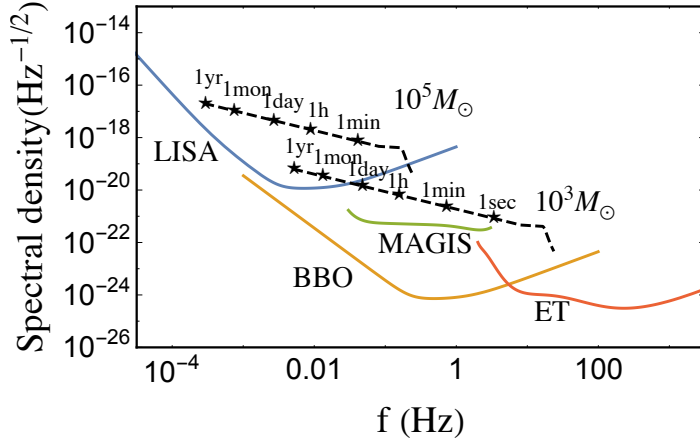


Figure 3.4 The spectral density of GW detector noises  $\sqrt{S_n(f)}$  (solid) and example chirping GW amplitudes  $\sqrt{f}|\tilde{h}(f)|$  (dashed) with  $M_{\text{BBH}} = 10^3 M_\odot$  and  $10^5 M_\odot$ .  $z_s = 1$ . The time marked with stars indicate the remaining time until final merger.

### 3.4.2 Log-likelihood detection

How well can the single-imaged diffractive lensing be detected? Detection likelihood is measured by [89, 110]

$$\ln p = -\frac{1}{2}(h_L - h_{\text{BF}}|h_L - h_{\text{BF}}), \quad (3.57)$$

where  $h_{\text{BF}}$  is the best-fit ‘unlensed’ GW waveform that maximizes the likelihood. The best-fit is performed with respect to the overall amplitude  $A$ , constant phase  $\phi_c$ , and coalescence time  $t_c$  of the unlensed  $\tilde{h}(f)$  Eq. (3.53) as

$$\tilde{h}_{\text{template}}(f) = \tilde{h}(f)Ae^{i(2\pi ft_c + \phi_c)}. \quad (3.58)$$

When  $h_{\text{BF}}$  perfectly matches  $h_L$ ,  $A = 1$  and  $t_c = \phi_c = 0$ . The inner product  $(h_1|h_2) = 4\text{Re} \int df \tilde{h}_1^*(f)\tilde{h}_2(f)/S_n(f)$ , where  $S_n(f)$  is the noise spectral density. The best-fit in this way is discussed more in [89, 110].



In this way, the  $\ln p$  measures how well lensed signals can be fitted with unlensed waveforms. Frequency dependent lensing amplitude  $|F(f)|$  will not be fitted by a constant  $A$ . Likewise, non-trivial frequency dependent lensing phase  $\varphi(f)$  cannot be canceled by  $\phi_c$  and  $t_c$ . Thus, the larger the  $|\ln p|$ , the worse the best-fit, hence the more confident is the existence of lensing.

In principle, the larger  $|\ln p|$ , which is equivalent to the smaller  $match^2$ , reduces the ability of GW detection. However, we can ignore such effects in our NFW lensing situations thanks to the small mismatch  $(1 - (\text{match}) \simeq 10^{-6})$ <sup>3</sup>. In spite of the small mismatch, the lensed GW can be distinguished from unlensed GW if signal-to-noise ratio(SNR) of GW waveform is sufficiently high [110, 121].

In this work, the binary intrinsic parameters like total mass, mass ratio, and spins are not included in the best-fit procedure. We expect that taking into account the binary parameters will not significantly reduce  $|\ln p|$  values. This is because, the frequency dependence of  $F(f)$  around the diffraction-geometric optics transition frequency (e.g. Fig. 3.3) is characteristically different from the intrinsic frequency dependence of GW waveform even if post-Newtonian corrections are considered. More accurate analysis on the potential degeneracy between the diffractive lensing and GW waveform are beyond our scope and should be explored in the future researches.

We require  $\ln p < -5.914$  for  $3\sigma$  confidence of the lensing detection. The requirement yields a proper lensing cross-section for given masses and distances

$$\sigma_l = \pi(r_0 x_s^{\max})^2. \quad (3.59)$$

There exists a maximum  $x_s^{\max}$  for given parameters because  $|\ln p|$  generally decreases with  $x_s$  as shown in Fig. 3.5. If there exist multiple roots of  $x_s^{\max}$ , we take the largest one, while if no root  $x_s^{\max} = 0$ . An example result of  $x_s^{\max}$  is shown in Fig. A.1 in

---

<sup>2</sup> $(\text{match}) \equiv (h_L | h_{\text{BF}}) / \sqrt{(h_L | h_L)(h_{\text{BF}} | h_{\text{BF}})}$

<sup>3</sup>Actually, from Eq. (3.63), one can easily show that the mismatch is approximately given by the square of the shear of the lens object.

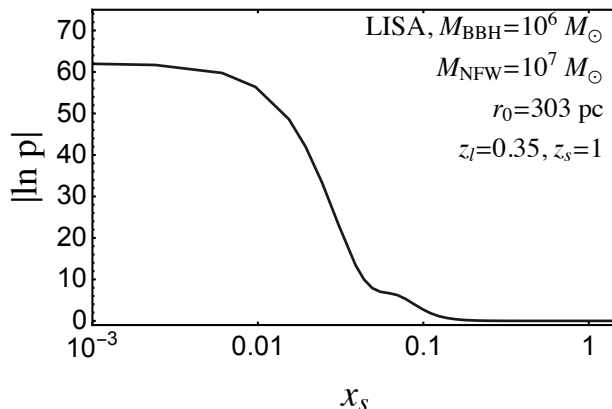


Figure 3.5  $|\ln p|$  as a function of  $x_s = r_s/r_0$ . Last 1 year of inspiral observed at LISA.

Appendix A.6. In later sections,  $\sigma_l$  will be used for lensing probabilities.

For numerical calculation, a more convenient form for  $\ln p$  is obtained by analytically minimizing  $\ln p$  with respect to  $A$  and  $\phi_c$  as

$$\ln p = -\frac{1}{2}(\rho_L^2 - \rho_{uL}^2), \quad (3.60)$$

where

$$\rho_L^2 = (h_L|h_L), \quad (3.61)$$

$$\rho_{uL}^2 = \max_{t_c} \left| \frac{4}{\rho_0} \int_{f_{\min}}^{f_{\max}} df \frac{|\tilde{h}_0(f)|^2}{S_n(f)} F^*(f) e^{2\pi i f t_c} \right|^2 \quad (3.62)$$

and  $\rho_0^2 = (h_0|h_0)$  is SNR squared. Here, the maximization with respect to  $t_c$  should be done numerically; but  $t_c$  maximization is relatively unimportant since adding  $T_0$  in Eq. (3.13) approximately does this maximization. More discussions are presented in Ref. [110] and in Appendix A.4.

As an aside, there also exists the maximum  $|\ln p|$  for some small  $x_s$  for given lensing parameters. As shown in Fig. 3.5,  $|\ln p|$  stops growing for  $x_s \lesssim 10^{-2}$ . It

is because for small enough  $x_s$  diffraction occurs in the whole frequency range of measurement so that diffraction amplification does not depend on  $x_s$  as shown in Fig. 3.3. Under this condition, we find that

$$|\ln p| \simeq \frac{1}{8} \left\{ \rho_0 \cdot \left| \gamma \left( \frac{r_F(f_0) e^{i\frac{\pi}{4}}}{\sqrt{2}} \right) \right| \cdot \ln \frac{f_{\max}}{f_{\min}} \right\}^2, \quad (3.63)$$

where  $f_0$  is a characteristic frequency at which

$$\frac{\rho_0^2}{2} = 4 \int_{f_0}^{f_{\max}} df \frac{|h_0(f)|^2}{S_n(f)}. \quad (3.64)$$

$f_0$  is typically close to the maximum point of  $|h_0(f)|^2/S_n(f)$ . Its derivation is given in Appendix A.5. Eq. (3.63) also supports our intuition that the strength of shear is critical to lensing detection.

## 3.5 Prospects

We first develop intuitions by semi-analytically estimating the parameter space of NFW lensing, and then obtain final results with full numerical calculation.

### 3.5.1 Semi-analytic estimation

Which NFW mass scale is relevant to diffractive lensing? Since diffractive lensing is sensitive to the mass profile at  $r_F$  through shear  $\gamma(r_F)$  Eq. (3.29), the profile must have sizable shear in the chirping range of  $r_F$ . For NFW, this happens if some range of  $r_F$  satisfies

$$10^{-3} r_0 \lesssim r_F \lesssim r_0. \quad (3.65)$$

The maximum is restricted to be within  $r_0$  because it is where  $\gamma \sim 3\kappa_0/2$  is most sizable; outside, gravity is suppressed quickly with  $\gamma \propto 1/x^2$ . The minimum  $10^{-3}r_0$  is introduced for the ease of calculation and is chosen arbitrarily; the area within the minimum is small enough not to affect lensing probability, and the inner profile may

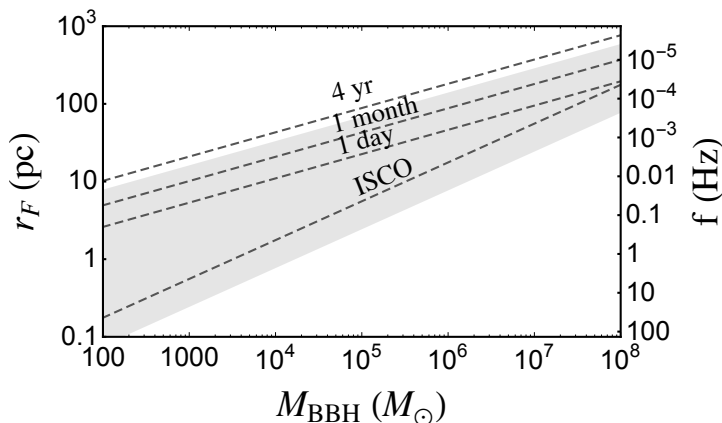


Figure 3.6 The range of Fresnel length Eq. (3.9) swept by a chirping GW during its last 1 year before merger (shaded). Other time periods are shown as dashed lines; ISCO refers to the innermost stable circular orbit. The corresponding GW frequencies are shown on the right vertical axis. Some part of this range, combined with detector sensitivities, must satisfy Eq. (3.65) for diffractive lensing.  $z_s = 1, z_l = 0.35$ .

be uncertain too. Therefore, the relevant  $M_{\text{NFW}}$  is the one whose length scale  $r_0$  is comparable to the range of  $r_F$ .

The chirping range of  $r_F \propto f^{-1/2}$  (hence the range of GW frequency) is determined by the total mass of a binary black hole,  $M_{\text{BBH}}$ , according to the standard GW chirping; see Sec. 3.4.1. Fig. 3.6 shows an example range of  $r_F$  swept during the last 1 year of chirping, as a function of  $M_{\text{BBH}}$ . Basically, the heavier, the earlier at lower frequencies they merge. The range spans one or two orders of magnitudes, while not significantly broadened by longer measurements since binary inspiral is much slower when far away from merger. We use the last 1-year measurements for numerical results.

Fig. 3.7 shows the relevant parameter space of NFW. The shaded region satisfies Eq. (3.65), which can be rewritten in terms of  $M_{\text{NFW}}$  and  $f$  as (using  $r_0$  in Eq. (3.43)

and  $r_F$  in Eq. (3.9))

$$13.6 M_\odot \left( \frac{\text{Hz}}{f_{\max}} \right)^{1.22} \lesssim M_{\text{NFW}} \lesssim 2.82 \times 10^8 M_\odot \left( \frac{\text{Hz}}{f_{\min}} \right)^{1.22}. \quad (3.66)$$

However, not all this region can be probed; signals must be strong enough. The overall change of amplification – the detectable signal – within a modest range of  $f$  is  $\Delta|F| \sim \gamma(r_F(f_*)) \cdot \mathcal{O}(1)$  from Eq. (3.29), with a characteristic frequency  $f_*$  within Eq. (3.65). Since the shear of NFW does not vary much within  $r_0$  as shown in Fig. 3.7,  $\gamma(r_F(f_*)) \sim \gamma(r_0)$ . Thus, roughly,

$$\text{SNR} \gtrsim 1/\gamma(r_0) \cdot \mathcal{O}(1) \quad (3.67)$$

is needed to detect the diffractive lensing by  $M_{\text{NFW}}$ . This is somewhat more rigorously justified from Eq. (3.63) and Fig. 3.12. The contours of  $\gamma(r_F)$ , reflecting the required SNR, are shown as solid lines.

Based on these, one can now estimate the sensitivity range of  $M_{\text{NFW}}$ . As quick examples, we show a green bar for each detector, with their maximum SNR at the corresponding frequency:  $\text{SNR} \simeq 5000, 10^5, 1000, 500$  at  $f \simeq 0.004, 0.3, 0.08, 6$  Hz for LISA, BBO, MAGIS, ET, respectively. They roughly show maximal sensitivities, only as quick references. One can see that  $M_{\text{NFW}} \lesssim 10^7 M_\odot$  is potentially sensitive to all detectors. The sensitivity range is indeed estimated by the comparison of the  $r_F$  range and the lens scale  $r_0$ . The lower  $M_{\text{NFW}}$  range is limited by too low frequency for LISA and BBO that prohibits diffractive lensing by small  $M_{\text{NFW}}$  (SNRs are large enough), or by too small SNR for MAGIS and ET that prohibits detection of small diffraction. Another to note is that, for given  $M_{\text{NFW}}$ , larger SNR is needed for lower-frequency detectors because corresponding larger  $r_F$  probes only outer parts of NFW with smaller shear.

A caveat is that this kind of estimation does not show any lensing probabilities. In the next subsection, we obtain final results with full numerical calculation, showing

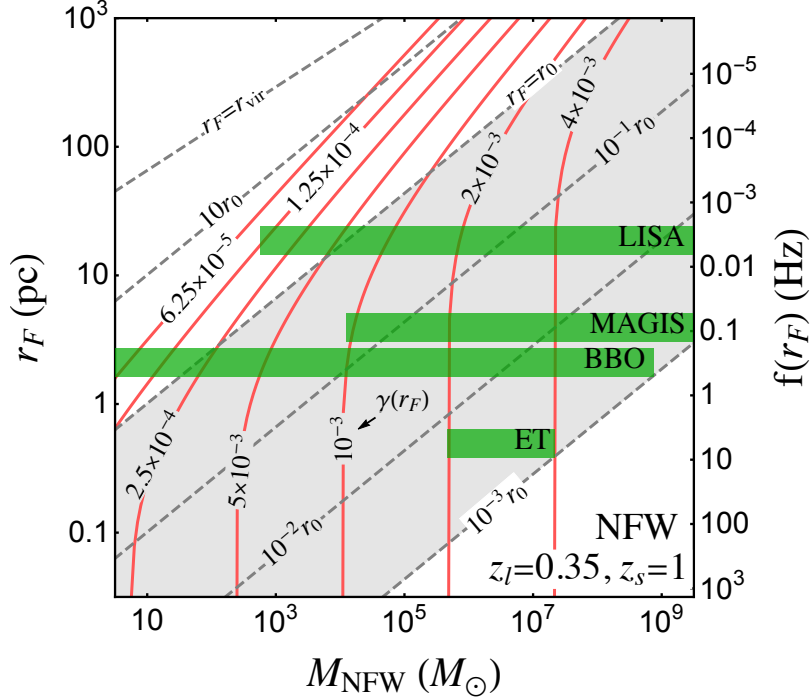


Figure 3.7 Semi-analytic estimation of the parameter space of NFW diffractive lensing. Diffractive lensing is relevant in the shaded region Eq. (3.65). Solid contours show the shear  $\gamma(r_F)$ , reflecting the required SNR for detection. The frequency corresponding to  $r_F$  is shown on the right vertical axis. For quick references, green bars roughly show maximal sensitivities at best frequencies. See text for details.  $z_s = 1, z_l = 0.35$ .

lensing probabilities as well as confirming these estimations.

### 3.5.2 Results

We calculate detection prospects, starting from the optical depth (lensing probability). For the given  $M_{\text{BBH}}$ ,  $z_s$  and  $M_{\text{NFW}}$ , the optical depth of the lensing is given by

$$\tau(z_s) = \int_0^{z_s} dz_l \sigma_l(z_l, z_s) \frac{1}{H_0} \frac{n_l(1+z_l)^2}{\sqrt{(1+z_l)^3 \Omega_m + \Omega_\Lambda}} , \quad (3.68)$$

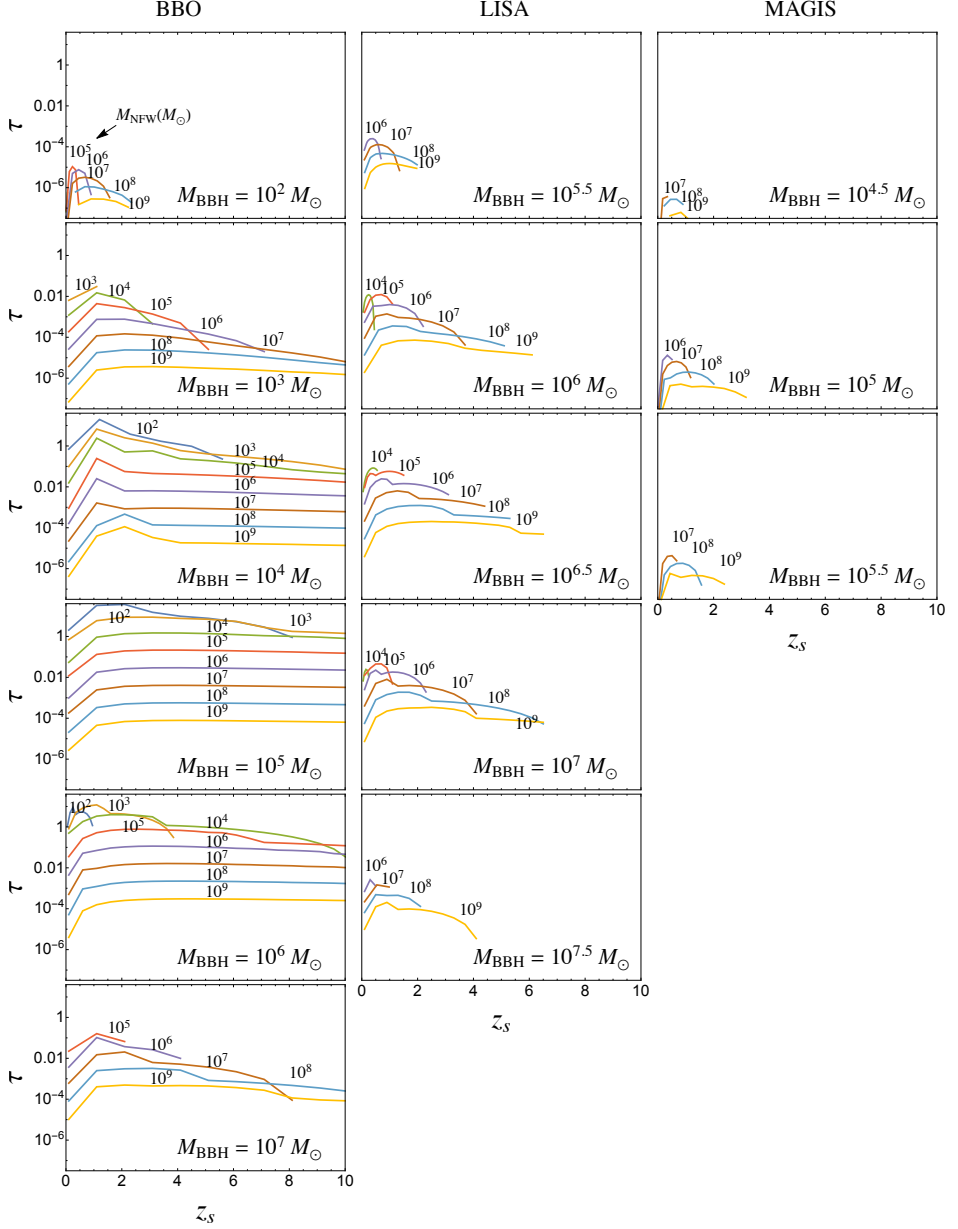


Figure 3.8 Optical depth  $\tau$  for the given  $M_{\text{NFW}}$  comprising the full DM abundance (i.e. no halo mass function) at BBO (left), LISA (mid), and MAGIS (right). Each curve is marked with  $M_{\text{NFW}}$ , and each panel with  $M_{\text{BBH}}$ . Last 1 year of inspiral and  $3\sigma$  log-likelihood lensing detection.

where  $\sigma_l$  is the proper cross-section defined in Eq. (3.59). The comoving DM number density  $n_l = \frac{f_{\text{DM}}\Omega_{\text{DM}}}{M_{\text{NFW}}} \frac{3H_0^2}{8\pi G}$  is assumed to be constant in  $z_l$ , with the fraction of mass density  $f_{\text{DM}}$  to the total DM abundance  $\Omega_{\text{DM}} = 0.25$ . Hubble constant  $H_0 = 70 \text{ km/s/Mpc}$ , and energy density  $\Omega_m = 0.3$ ,  $\Omega_\Lambda = 0.7$  of matter and vacuum energy in units of critical density  $\rho_c = 3H_0^2/8\pi G$ . The lensing probability is  $P(\tau) = 1 - e^{-\tau} \simeq \tau$  for  $\tau \ll 1$ .

Fig. 3.8 shows the optical depths at LISA, BBO, and MAGIS, for the given  $M_{\text{NFW}}$  comprising the total  $\Omega_{\text{DM}}$  (i.e.  $f_{\text{DM}} = 1$  regardless of  $M_{\text{NFW}}$ ); the optical depth at ET is too small to show. Overall, BBO and LISA have sizable  $\tau$  close to or even larger than 1, while MAGIS has much smaller  $\tau$  at most  $\sim 10^{-5}$ . This result for single  $M_{\text{NFW}}$  can be combined with any mass functions such as given in Refs. [140, 141].

The GW lensing event rate  $\dot{N}_L$  is obtained by integrating the lensing probability  $P(\tau)$  with the comoving merger-rate density  $\dot{n}_s$

$$\dot{N}_L = \int_0^{z_h} dz_s \frac{1}{H_0} \frac{4\pi\chi^2(z_s)}{\sqrt{(1+z_s)^3\Omega_m + \Omega_\Lambda}} \frac{\dot{n}_s}{1+z_s} P(\tau), \quad (3.69)$$

where  $z_h$  is the horizon distance of a GW detector and  $\chi(z)$  is the comoving distance. The extra factor  $1/(1+z_s)$  accounts for the redshift of the source-frame time period used to define the merger-rate.

Table 3.1 shows total lensing events per year  $\dot{N}_L$ . Results are marginalized over  $M_{\text{NFW}} = 10^3 - 10^{10} M_\odot$  with a mass function

$$\frac{dn_l}{dM_{\text{NFW}}} \propto M_{\text{NFW}}^{-2} \quad (3.70)$$

and summed for  $M_{\text{BBH}} = 10^2 - 10^8 M_\odot$  with three models of  $\dot{n}_s$ . The power slope of a mass function is taken to be  $-2$  for simplicity; heavier halos may contain abundant baryons that are not well described by NFW, while lighter halos' existence and properties are more model dependent. As for three models of  $\dot{n}_s$  (as a function of  $M_{\text{BBH}}$  and  $z_s$ ), two of them are taken from the models of massive black hole mergers



Detector	$\dot{N}_L$			$\dot{N}_{\text{GW}}$		
	const.	optim.	pessim.	const.	optim.	pessim.
BBO	30	40	10	58	270	13
LISA	0.3	0.03	0.02	47	63	12
MAGIS		$< 10^{-5}$		25	187	9
ET		0		21	124	1

Table 3.1 The expected numbers of lensing detections per year  $\dot{N}_L$  and of total GW detections per year  $\dot{N}_{\text{GW}}$ , at BBO, LISA, MAGIS, and ET. The results are marginalized over  $M_{\text{NFW}} = 10^{3-10} M_\odot$  with the mass function Eq. (3.70) and summed for  $M_{\text{BBH}} = 10^{2-8} M_\odot$  with three models of  $\dot{n}_s$ : constant  $\dot{n}_s = 0.01 \text{ Gpc}^{-3} \text{yr}^{-1}$ , optimistic and pessimistic merger models of heavy BBHs [142]. Light BBH mergers are ignored.

in Ref. [142]; most optimistic and pessimistic predictions are used. Another model, as a simple reference, is constant  $\dot{n}_s = 0.01 \text{ Gpc}^{-3} \text{yr}^{-1}$  for all  $M_{\text{BBH}}$  and  $z_s$ ; this reference choice predicts similar total GW detection rates  $\dot{N}_{\text{GW}}$ , as shown in the last three columns of Table. 3.1. In all cases, BBH mergers are considered for  $z_s \leq 10$  and  $M_{\text{BBH}} = 10^2 \sim 10^8 M_\odot$ , where lighter BBHs have too small SNRs to contribute to  $\dot{N}_L$  although they may contribute sizably to  $\dot{N}_{\text{GW}}$  (see Fig. 3.9 second panel).

Above all, in Table 3.1, all three models of  $\dot{n}_s$  predict that BBO can detect  $\mathcal{O}(10)$  lensing events per year, while LISA barely single event, and MAGIS and ET no event. Even though LISA and BBO have relatively large  $\tau$ , the number of relevant sources is not so large to start with (see the  $\dot{N}_{\text{GW}}$  column).

Which  $M_{\text{NFW}}$  range has high event rates? In Fig. 3.9 upper panel, we show the event rates in log intervals of  $M_{\text{NFW}}$  with the mass function. Most importantly, we conclude that the target range  $M_{\text{NFW}} \lesssim 10^7 - 10^8 M_\odot$  can be probed by diffractive lensing at BBO (and marginally at LISA). As discussed in Sec. 3.5.1 and Fig. 3.7, this range has the right scale radii  $r_0$  that happen to coincide with the range of  $r_F$  at these detectors. Although MAGIS and ET also have right frequency scales, their SNRs are

typically too small. Notably, most BBO events are expected from light NFWs:  $\mathcal{O}(10)$  events from light  $M_{\text{NFW}} = 10^3 - 10^5 M_\odot$ , and  $\mathcal{O}(1 - 10)$  from  $M_{\text{NFW}} = 10^5 - 10^7 M_\odot$ , and smaller from heavier NFWs. LISA and MAGIS are relatively more sensitive to heavier NFWs, albeit with smaller event rates.

Figs. 3.8 and 3.9 also show an important feature of diffractive lensing: heavier NFWs yield smaller  $\tau \propto M_{\text{NFW}}^{-0.8}$  (at low  $z_s$ ). Therefore, unlike geometric-optics lensing, lighter NFWs are actually more sensitive. It is because the number density of heavier NFWs falls ( $n_l \propto 1/M_{\text{NFW}}$ ) more quickly than the increase of the proper lensing cross-section ( $\sigma_l \propto M_{\text{NFW}}^{0.2}$ ). This is understood from that the length scale of diffractive lensing is determined dominantly by  $r_F$ , not by  $M_{\text{NFW}}$ , since the  $r_F$  range is much narrower than the  $r_0$  range. For example, consider diffractive lensing by  $M_{\text{NFW}} = 10^3 M_\odot$  and  $10^9 M_\odot$  probed by a common  $M_{\text{BBH}} = 10^5 M_\odot$ : even though their masses and  $r_0$  differ sizably by  $10^6$  and  $\sim 300$  (Eq. (3.43)), the relevant range of  $r_F$  is commonly fixed to be about  $\sim 10$  (Fig. 3.6) so that the lensing cross-sections cannot differ by more than  $\sim 10^2$ . This is why  $\sigma_l$  is not so sensitive to  $M_{\text{NFW}}$  that  $\tau$  has a negative slope with  $M_{\text{NFW}}$ <sup>4</sup>.

This is in stark contrast to usual geometric-optics lensing. For milli-lensing perturbations discussed in Sec. 3.1 and Appendix A.1,  $n_l \sigma_l \propto M_{\text{NFW}}^{1.5-4}$  has a large positive slope with the mass so that light subhalos are insensitive inherently. The strong lensing by a point-mass  $M$  is another example, where  $r_E \gtrsim r_F$  makes  $\sigma_l \propto r_E^2 \propto M$ . But in this case, the power is cancelled by that of  $n_l \propto 1/M$  so that very light compact DM can also be probed with lensing, as mentioned. Diffractive lensing is sensitive to lower masses more preferentially.

Then, what does determine the lower range of  $M_{\text{NFW}}$ ? Fig. 3.8 shows that, at low  $z_s$ , only down to  $M_{\text{NFW}} \gtrsim 10^2, 10^4, 10^6 M_\odot$  can have sizable  $\tau$  at BBO, LISA, MAGIS.

---

<sup>4</sup>As an aside, if detection criterion is relaxed (say,  $3\sigma$  to  $2\sigma$ ),  $\tau$  becomes steeper  $\propto M_{\text{NFW}}^{-1}$ , as the lighter NFW detection is more subject to the criterion.

As discussed in Fig. 3.7, it is either too long Fresnel length (for BBO and LISA with large enough SNRs) or too small SNR (for MAGIS and ET); light enough NFWs would have too small  $r_0$  or too weak gravity to induce large enough diffractions. Moreover, the weaker gravity also limits the sensitivity at high  $z_s$  for lighter NFWs. The highest range of  $z_s$  roughly scales with  $\gamma(r_0)$ , since  $\text{SNR} \propto 1/z_s \gtrsim 1/\gamma$ . For example, the ratio of  $\gamma(r_0)$  between  $M_{\text{NFW}} = 10^5$  and  $10^7 M_\odot$  is about 3 (Fig. 3.7), and this roughly explains why  $M_{\text{NFW}} = 10^7 M_\odot$  can probe 3 times farther  $z_s$ , e.g. at LISA. Meanwhile, the decrease at small  $z_s$  is due to the small number of lenses and small  $\kappa_0 \propto d_{\text{eff}}$ .

Fig. 3.9 lower panel also shows the event rates in terms of  $M_{\text{BBH}}$  (with  $M_{\text{NFW}}$  summed with the mass function). The largest  $\tau$  is obtained for  $M_{\text{BBH}} = 10^{6-7} M_\odot$  at LISA,  $10^{4-6} M_\odot$  at BBO, and  $\sim 10^5 M_\odot$  at MAGIS. They are the mass ranges that typically produce largest SNRs. As expected, large  $\text{SNR} \gtrsim \mathcal{O}(10^3)$  is needed to overcome small fractional change of waveforms  $\sim \mathcal{O}(\gamma(r_0)) \sim \mathcal{O}(\kappa_0) \lesssim \mathcal{O}(10^{-3})$ . Such a large SNR is readily obtained at LISA and BBO from heavy BBHs, while rarely at MAGIS, simply due to larger noise. Although the frequency range of ET is right to induce diffractive lensing by small NFWs (see Fig. 3.7), SNRs are just too small.

The variations between optimistic and pessimistic predictions are shown as shaded bands. They are only about  $\sim 10$ . But the predictions from the constant  $\dot{n}_s$  (solid) at LISA and MAGIS tend to be larger (by about 10) even though they had similar  $\dot{N}_{\text{GW}}$ . This tendency stems from that the massive-black-hole merger models predict more sources at higher  $z_s$  so that LISA and MAGIS with smaller SNRs depend more sensitively on such distributions of source properties.

Lastly, the results without a mass function (dashed) have almost the same shape as the solid lines but just a larger normalization by a factor  $\sim 8$ . One exception is at low  $M_{\text{NFW}}$  range of BBO, where  $\tau > 1$  had to be cut off at  $\tau = 1$  in our calculation.

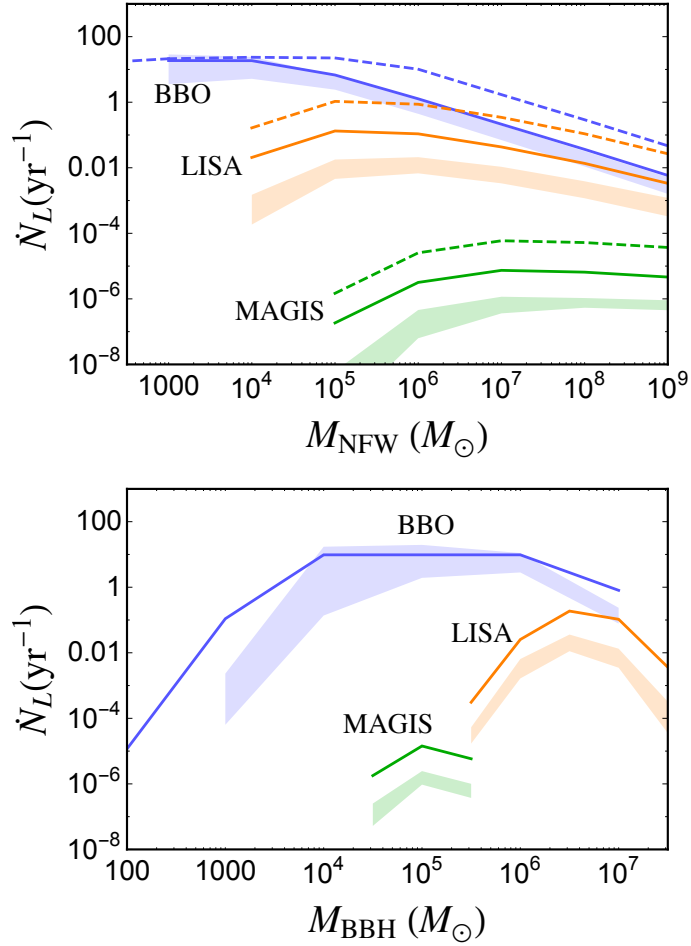


Figure 3.9 The number of lensing events per year  $\dot{N}_L$  at BBO, LISA, and MAGIS, as functions of  $M_{\text{NFW}}$  (top) or  $M_{\text{BBH}}$  (bottom). The shaded bands are the range of optimistic and pessimistic  $\dot{n}_s$ , while the solid lines are from constant  $\dot{n}_s$ ; their total event rates are normalized as in Table 3.1. For comparison, dashed lines show results without a mass function; each  $M_{\text{NFW}}$  comprises total  $\Omega_{\text{DM}}$ . See more in text. Last 1 year of inspiral and  $3\sigma$  log-likelihood lensing detection.

These events are where multi-lensings of a single GW can occur. If SNR is very large, even tiny lensing effects that might happen multiple times along the line of sight can all be counted. Such events may not be well detected as signals will be complicated, depending on many parameters of multi-lens environments. Using  $\tau = 1$  for such events means that we can always select out single-lensing events by, e.g., imposing stronger detection criteria for such events, favoring the ones with single strong lensing and small perturbations.

This completes our study on the NFW DM subhalos to which weak diffractive lensing is applied.

## 3.6 Generalization

In this section, by working out lensing by power-law profiles, we not only demonstrate how readily one can estimate diffractive lensing in general (using our formalism), but also complete our discussions with strong diffractive lensing and the idea of measuring/distinguishing mass profiles.

### 3.6.1 Lensing by power-law profiles

Starting from a general power-law density profile

$$\rho(x) = \rho_0 x^{-k-1}, \quad (0 < k < 2) \quad (3.71)$$

with  $x = r/r_0$  for some scale  $r_0$ , we obtain 2D projected potentials

$$\bar{\kappa}(x) = \frac{2\kappa_0}{2-k} x^{-k}, \quad \kappa(x) = \kappa_0 x^{-k}, \quad \gamma(x) = \frac{k\kappa_0}{2-k} x^{-k}, \quad (3.72)$$

with

$$\kappa_0 = 4\pi d_{\text{eff}} \rho_0 r_0 \text{B}\left(\frac{1}{2}, \frac{k}{2}\right). \quad (3.73)$$

The range of  $k$  makes the enclosed mass finite.

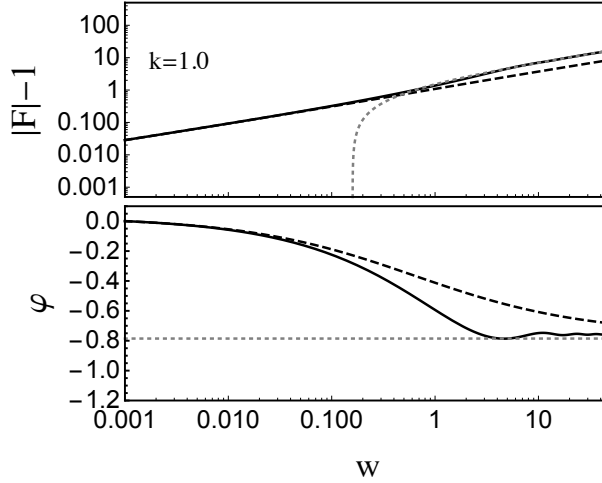


Figure 3.10 The amplitude and phase of  $F(w)$  obtained by full calculation (solid), weak diffraction approximation Eq. (3.77) (dashed), and strong diffraction approximation Eq. (3.79) (dotted) for a power-law profile with  $k = 1$ .  $x_s = 0$  for simplicity.

We fix the overall scale by specifying  $M_{\text{vir}}$ . Further by choosing  $r_0 = r_E$ , 2D projected potentials are simplified as

$$\bar{\kappa}(x) = x^{-k}, \kappa(x) = \frac{2-k}{2}x^{-k}, \gamma(x) = \frac{k}{2}x^{-k}, \quad (3.74)$$

now with  $x = r/r_E$ . The Einstein radius is fixed by  $M_{\text{vir}}$  as

$$r_E = \left[ \frac{8\pi}{2-k} d_{\text{eff}} \rho_0 r_0^{k+1} B\left(\frac{1}{2}, \frac{k}{2}\right) \right]^{\frac{1}{k}}, \quad (3.75)$$

$$\rho_0 r_0^{1+k} = \frac{200\rho_c(2-k)}{3} \left( \frac{3}{4\pi} \frac{M_{\text{vir}}}{200\rho_c} \right)^{\frac{1+k}{3}}, \quad (3.76)$$

where  $\rho_c = 3H_0^2/(8\pi)$  and  $B(x, y) = \Gamma(x)\Gamma(y)/\Gamma(x+y)$ . Unlike NFW,  $k < 2$  profiles have non-negligible  $r_E$  so that it is a useful length scale when it is comparable to the  $r_F$  of GWs.

For weak diffractive lensing which is valid for  $w = 2(r_E/r_F)^2 \lesssim \min(1, 2/x_s^2)$

(Eqs. (3.11) and (3.12)), our approximate results in terms of  $\bar{\kappa}(x)$  and  $\gamma(x)$  are

$$\begin{aligned}
F(w) &\simeq 1 + \frac{w}{i} \int_0^\infty dx x e^{iw \frac{x^2}{2}} x^{-k} \\
&= 1 + 2^{-\frac{k}{2}} e^{-i \frac{k\pi}{4}} \Gamma\left(1 - \frac{k}{2}\right) w^{\frac{k}{2}} \\
&= 1 + 2^{-\frac{k}{2}} \Gamma\left(1 - \frac{k}{2}\right) \bar{\kappa}\left(\frac{1}{\sqrt{w}} e^{i \frac{\pi}{4}}\right), \tag{3.77}
\end{aligned}$$

$$\begin{aligned}
\frac{dF(w)}{d \ln w} &\simeq \frac{w}{i} \int_0^\infty dx x e^{iw \frac{x^2}{2}} \frac{k}{2} x^{-k} \\
&= 2^{-\frac{k}{2}} e^{-i \frac{k\pi}{4}} \Gamma\left(1 - \frac{k}{2}\right) \frac{k w^{\frac{k}{2}}}{2} \\
&= 2^{-\frac{k}{2}} \Gamma\left(1 - \frac{k}{2}\right) \gamma\left(\frac{1}{\sqrt{w}} e^{i \frac{\pi}{4}}\right). \tag{3.78}
\end{aligned}$$

Here, integrals are evaluated exactly and the results agree with Eqs. (3.28) and (3.29) obtained from dominant supports. Above the weak diffraction range, but still within  $w < 1/(2x_s)$ , strong diffractive lensing is described by Eq. (3.31) which is calculated in this case as

$$F(w) \simeq i^{-1/2} \sqrt{\frac{2\pi w}{1 - \kappa(1) - \gamma(1)}} = i^{-1/2} \sqrt{\frac{2\pi w}{k}}. \tag{3.79}$$

In Fig. 3.10, we compare  $F(w)$  obtained by full calculation (solid), weak diffraction Eq. (3.77) (dashed), and strong diffraction Eq. (3.79) (dotted) for  $k = 1$ . Approximate results do agree with full results in their respective validity ranges, confirming not only analytic calculations but also the validity ranges of weak/strong diffractions Eqs. (3.11) and (3.12). Weak diffraction starts to deviate at  $w \gtrsim 0.1$  somewhat earlier than at 1 since the Born approximation starts to break near  $r_E$ . Weak and strong diffractive lensing do have different slopes transitioning at around  $w = 2r_E^2/r_F^2 \simeq 1$  (the difference was explained in Sec. 3.2.5), thus  $r_E$  (existence and value) can be directly measured, effectively yielding  $M_E = r_E^2/4d_{\text{eff}}$  too. In the figure,  $x_s = 0$  for simplicity, but frequency independent results will arise for  $w \gtrsim 1/2x_s$  with finite  $x_s$ ,

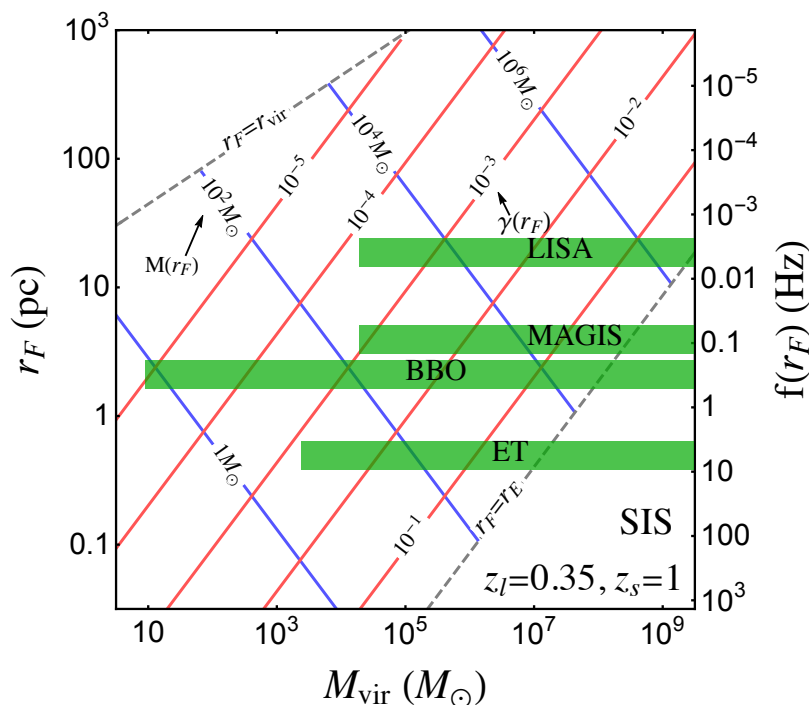


Figure 3.11 Same as Fig. 3.7 but for SIS with  $k = 1$ . Red contours show  $\gamma(r_F)$ , reflecting the required SNR for detection, and blue contours show the enclosed mass within  $r_F$ . Length scales,  $r_{\text{vir}}$  and  $r_E$ , are shown as dashed lines.

similarly to Fig. 3.3. Although not shown,  $\varphi(w)$  in this regime does not asymptote to zero (unlike the NFW case in Fig. 3.3) because the relative times delays among multiple images remain there.

### 3.6.2 Semi-analytic estimation

Using our analytic solutions, we estimate the detection prospects of diffractive lensing by power-law lenses.

To start off, as done for NFW, we estimate the relevant parameter space of the profile with  $k = 1$  in Fig. 3.11. This is called SIS profile, and is conventionally written



in terms of the isothermal velocity dispersion  $\sigma_v$  as  $\rho(r) = \sigma_v^2/(2\pi r^2)$ . 2D projected potentials are dimensionless

$$\bar{\kappa}(x) = 1/x, \quad \kappa(x) = 1/2x, \quad (3.80)$$

$$\gamma(x) = 1/2x = 0.07 \left( \frac{\sigma_v}{1 \text{ km/s}} \right)^2 \left( \frac{d_{\text{eff}}}{\text{Gpc}} \right) \left( \frac{\text{pc}}{r} \right), \quad (3.81)$$

with  $x = r/r_E$ , but scale parameters are rewritten as

$$r_E = 4\pi d_{\text{eff}} \sigma_v^2 = 0.14 \text{ pc} \times \left( \frac{\sigma_v}{1 \text{ km/s}} \right)^2 \left( \frac{d_{\text{eff}}}{\text{Gpc}} \right), \quad (3.82)$$

and the enclosed mass  $M(r) = \pi \sigma_v^2 r$  within  $r_E$  and  $r_{\text{vir}}$

$$M_E = 4\pi^2 d_{\text{eff}} \sigma_v^4 = 1.02 \times 10^6 M_\odot \left( \frac{\sigma_v}{10 \text{ km/s}} \right)^4 \left( \frac{d_{\text{eff}}}{\text{Gpc}} \right), \quad (3.83)$$

$$M_{\text{vir}} = \frac{2}{\sqrt{50}} \frac{\sigma_v^3}{H_0} = 9.39 \times 10^8 M_\odot \left( \frac{\sigma_v}{10 \text{ km/s}} \right)^3. \quad (3.84)$$

The detectable  $M_{\text{vir}}$  range is again estimated by the comparison of  $\gamma(r_F)$  and SNR, with  $r_F$  being the Fresnel length at the most sensitive frequency. For example, ET ( $r_F(f = 10 \text{ Hz}) \sim 1 \text{ pc}$ ) with  $\text{SNR} = \mathcal{O}(100)$  can probe a SIS lens as small as  $M_{\text{vir}} = 10^4 M_\odot$  (or,  $\sigma_v = \mathcal{O}(1 \text{ km/s})$ ), corresponding to the enclosed mass  $M(r_F) = 10 M_\odot$  (blue solid). This estimation agrees with more dedicated calculations in Ref. [110], as the lower mass range is in the weak diffraction regime with  $r_F \gg r_E \simeq 0.1 \text{ pc}$ .

There are a few notable differences of Fig. 3.11 from NFW results of Fig. 3.7. The first is that ET can probe smaller  $M_{\text{vir}}$  than MAGIS and LISA. This is because, for a given  $M_{\text{vir}}$ , higher frequencies probe inner parts which now yield significantly larger shear, reflecting the steeper profile. Another is the relevance of the Einstein radius, which was essentially zero for NFW. This is further discussed in the following.

Further, we can estimate somewhat more accurately, but still much more easily than full numerical analysis. Using weak diffraction results Eqs. (3.77) and (3.78), we calculate  $\ln p$  for detection by minimizing with respect to  $A$  and  $\phi_c$ . This result is

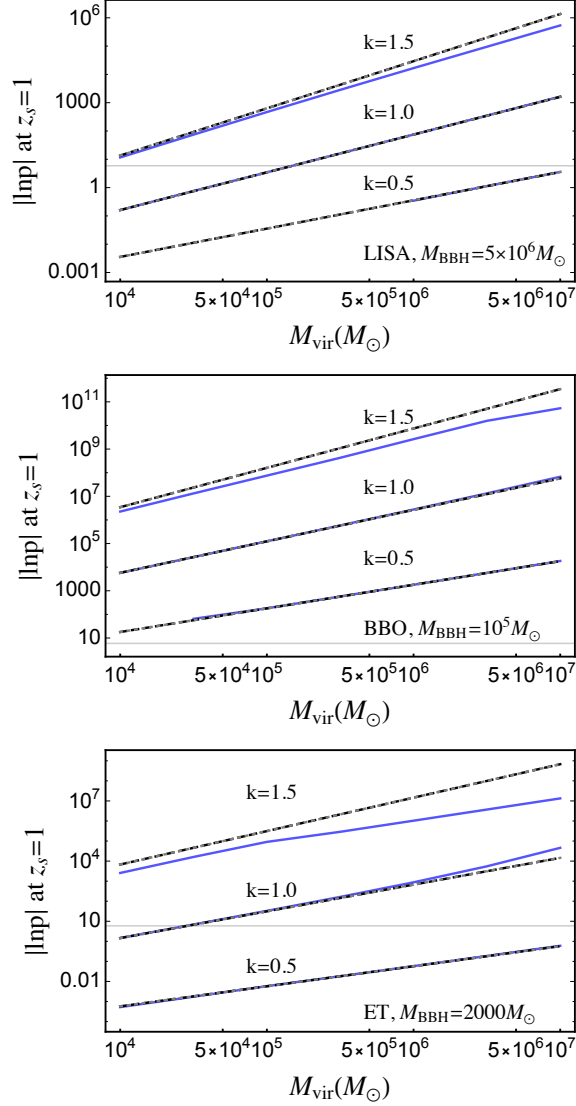


Figure 3.12 The comparison of  $|\ln p|$  for detection obtained with full numerical (solid) and approximate weak diffraction Eqs. (3.77) and (3.78) (dashed). Also shown are estimations using only shear and SNR Eq. (3.85) (dotted; which overlap with dashed). Each panel uses the BBH mass yielding maximum SNR. Horizontal lines denote the  $3\sigma$  threshold,  $|\ln p| = 5.914$ .

compared with full numerical result in Fig. 3.12. They do agree well for most  $M_{\text{vir}}$  and  $k$ , but deviations in the heavy mass region of large  $k$  are due to strong diffractive lensing. As shown in Fig. 3.13, for given  $M_{\text{vir}}$ , the larger  $k$ , the larger  $M_E$  so that strong diffraction becomes more relevant from lower frequencies. In this region, the frequency slope  $w^{1/2}$  Eq. (3.79) is steeper (shallower) than that of weak diffraction  $w^{k/2}$  Eq. (3.77) for  $k < 1$  ( $k > 1$ )<sup>5</sup> so that full results are stronger (weaker). In addition to these results, dotted lines show much simpler estimations based solely on shear and SNR (motivated in Sec. 3.5.1 and supported rigorously in Eq. (3.63))

$$|\ln p| \simeq \alpha (\text{SNR} \times \gamma(r_F(f_*)))^2, \quad (3.85)$$

where  $\alpha = \mathcal{O}(0.1)$  reproduces the analytic results. In all, Fig. 3.12 confirms our analytic results and demonstrates how readily one can estimate diffractive lensing using our formalism.

### 3.6.3 Peeling off profiles

It was advocated that our formalism in terms of 2D potentials makes it clear what it means to measure the mass profile with a single diffractive lensing event. The basic idea is simple: different profile slope  $k$  results in different frequency dependence during the probe of a successively smaller length scale. As a simple demonstration of this exciting possibility, we estimate the measurement accuracy of the slope  $k$ .

Similarly to detection estimates, we calculate  $\ln p$ , but this time including  $k$  as a fitting parameter (in addition to  $A$  and  $\phi_c$ ). We define the measurement accuracy  $\delta k$  as the variation of  $k$  with respect to the true  $k_0$  that yields  $|\ln p| = 5.914$ . In Fig. 3.14, we show the results, again obtained from full numerical, weak diffraction analytic, and shear-times-SNR. Above all, different calculations agree well if weak diffraction dominates (for small  $k$  and small  $M_{\text{vir}}$ ). Measurement accuracies are good as long as

---

<sup>5</sup>The turnover can be more accurately found to be  $k \simeq 1.3$  using Eqs. (3.77) and (3.79).

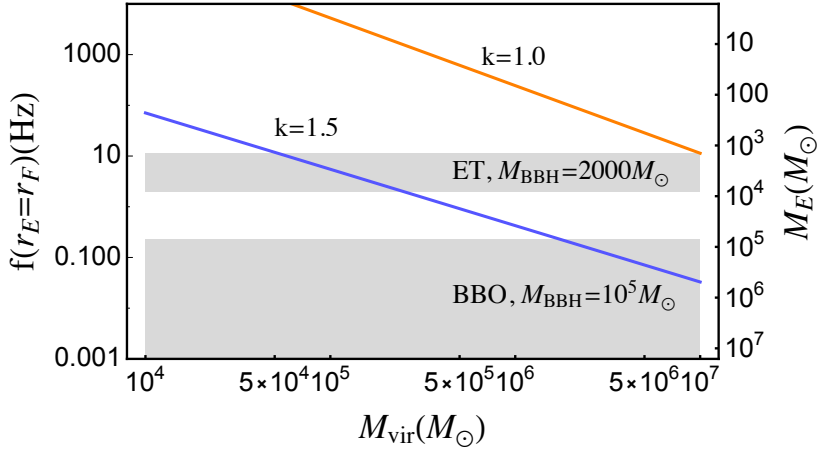


Figure 3.13 The Einstein mass and the corresponding frequency for  $r_F = r_E$ , as a function of  $M_{\text{vir}}$ .  $k = 1.0$  (orange) and  $1.5$  (blue). The region above(below) each line is the weak(strong) diffraction regime. Shaded regions represent the chirping frequency ranges measured at given detectors.  $z_s = 1, z_l = 0.35$ .

lensing can be detected. Basically, in the weak diffraction regime, the heavier or the steeper the lens is, the more accurate measurement or distinction of profiles.

Notably, full numerical results deviate more significantly and yield much worse results in Fig. 3.14, compared to the detection prospects in Fig. 3.12. This is an important effect of strong diffractive lensing, qualitatively different from weak diffraction. Strong diffraction has universal frequency dependence  $w^{1/2}$  Eq. (3.79) independent of the power  $k$ ; as discussed carefully in Sec. 3.2.5, it was due to the breaking of the scale invariance by an Einstein ring. As a result, different profiles are harder to be distinguished; detection itself was more robust because it is essentially the comparison of power  $k$  and flat potentials. Thus, peeling off profiles is possible only with weak diffractive lensing.

Since our analysis on the diffractive lensing ignores the parameter degeneracies between the lens profile and GW waveform, there might be some overestimation in

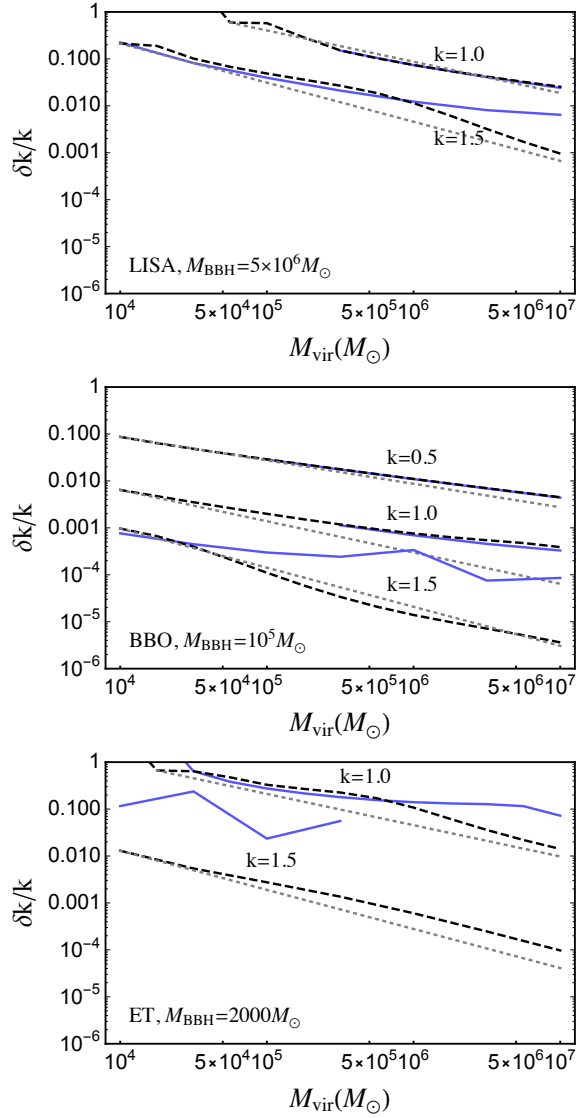


Figure 3.14 Same as Fig. 3.12 but for profile measurement accuracies represented by  $\delta k/k$ . Cases with  $\delta k/k > 1$  are not shown.

the profile measurement accuracy. But, in practice, the non-zero impact parameter  $x_s$  which induces the diffraction-to-geometric-optics transition might be able to resolve some degeneracy between the profile and GW waveform parameters as discussed in

Sec. 3.4.2.

### 3.6.4 Core-vs-cusp

If GW diffractive lensing can probe mass profiles, can it resolve the core-vs-cusp problem? There exist observational evidences that DM halos may contain flat cores of  $\mathcal{O}(0.1 - 1)$  kpc radius [68, 70] rather than cuspy NFW  $\propto 1/r$ . Such cores would change lensing effects at the corresponding frequencies. But this length scale is too large, corresponding to too low frequencies  $f \lesssim 10^{-4}$  Hz (Fig. 3.6) for chirping GWs to be relevant; the LISA's most sensitive frequency range was  $\sim 0.003$  Hz. It is currently the problem more of halos rather than of subhalos. Whether this problem persists to smaller length scales (smaller DM-dominated halos) is not certain, and it is this question that can be answered by observations of GW diffractive lensing.

## 3.7 Summary

First, we have developed a formalism for weak and strong diffractive lensing and solved it analytically. As a result, complex lensing integral is evaluated in terms of much simpler 2D-projected potentials. In particular, the frequency dependence of weak lensing turns out to be due to shear of a lens at the Fresnel length  $r_F \propto f^{-1/2}$ . These results make not only underlying physics of diffraction clearer but also its estimation much easier, as discussed and demonstrated throughout this paper. Moreover, the idea of measuring mass profiles became concrete.

We have also derived the condition or the validity range of diffractive lensing. It turns out that there exist two different phases of diffraction: weak and strong. They are separated by the Einstein radius, outside of which is approximately scale invariant leading to  $|F(w)| - 1 \propto w^{k/2}$  (for power-law profiles) while inside of which has only azimuthal symmetry leading to universal  $|F(w)| \propto w^{1/2}$ . The innermost range of

diffractive lensing is determined by properties of a caustic (multi-imaged cases) or by the source location.

Applying these, we have shown that NFW subhalos of  $M_{\text{NFW}} \lesssim 10^7 M_\odot$ , which cannot be probed with existing methods, can be detected individually with GW diffractive lensing. Detection prospects are  $\mathcal{O}(10)$  events per year at BBO and less at LISA, limited mainly by small merger rates and large required SNR  $\gtrsim 1/\gamma(r_0) \sim 10^3$ . This mass scale is sensitive because the corresponding scale radius  $r_0$  happens to be comparable to the range of  $r_F$  at future GW detectors. Notably, unlike strong lensing observables, the scale of diffractive lensing is dominantly fixed by  $r_F$  rather than  $r_0$  (or the lens mass) so that it can be relatively more sensitive to lighter lenses.

Further, we have applied our formalism to readily estimate the detection and profile measurements for general power-law potentials. This application also makes it clear about the features of strong diffractive lensing and makes the idea of measuring mass profiles concrete. Just as the shear field measured from galaxy shape distortions is used to measure galactic profiles and matter power spectrum, GW diffractive lensing can potentially be used to measure small-scale shear and reveal the particle nature of DM roaming in the subgalactic scale.

# Appendix A

## Appendix for Diffractive lensing

### A.1 $M_{\text{NFW}}$ scaling of milli-lensing perturbation

We estimate the sensitivity of milli-lensing perturbation observations on  $M_{\text{NFW}}$ . In particular, we aim to derive the dependence on the mass and the lower mass range, both of which can be contrasted with those of diffractive lensing.

The flux ratio anomaly is the most sensitive observable of milli-lensing perturbation; it is a second-derivative of  $\hat{T}_d$  surface [72]. The typical requirement of  $\gtrsim 10\%$  flux perturbation  $\Delta\mu/\mu$  by NFW subhalos [75, 78, 98] is translated to the requirement of subhalo's  $\kappa(x)$  as

$$\frac{\Delta\mu}{\mu} \simeq \kappa(x) \gtrsim 0.1, \quad (\text{A.1})$$

leading to maximum possible  $x$  (using Eqs. (3.39) and (3.38))

$$x \lesssim x_{\text{max}} \simeq 2 \exp \left( -\frac{0.1}{3\kappa_0(M_{\text{NFW}})} - \frac{1}{2} \right). \quad (\text{A.2})$$

Using  $\kappa_0 \propto M_{\text{NFW}}^{0.18}$  Eq. (3.44) and  $r_0^2 \propto M_{\text{NFW}}^{0.82}$  Eq. (3.43), the lensing cross-section



$\sigma_l = \pi r_0^2 x_{\max}^2$  scales with the mass as

$$\frac{d \ln \sigma_l}{d \ln M_{\text{NFW}}} \simeq 0.82 + 0.18 \left( \frac{2}{3} \frac{0.1}{\kappa_0(M_{\text{NFW}})} \right) \simeq 5 - 2.5 \quad (\text{A.3})$$

for  $M_{\text{NFW}} = 10^7 - 10^9 M_\odot$  (having  $\kappa_0(M_{\text{NFW}}) = 0.003 - 0.008$ ), respectively. Thus,  $n_l \sigma_l \propto M_{\text{NFW}}^{4-1.5}$  scales rapidly with the mass. Although heavier masses are subject to larger shot noise, this scaling inherently limits the sensitivity to light NFWs. If the profile were more compact as for SIS or pseudo-Jaffe with a power-law  $\kappa(x) \propto 1/x$ , the mass dependence would have been shallower as  $n_l \sigma_l \propto M_{\text{vir}}^{1/3}$ . As emphasized, this positive scaling slope is in stark contrast with the negative slope of diffractive lensing (which makes GW diffraction more suitable to probe light NFWs).

Now, how small  $M_{\text{NFW}}$  can be detectable with sizable probabilities? The average 2D-projected separation of NFW subhalos within the Einstein radius 5 kpc of a galaxy is about  $\mathcal{O}(0.1) r_0$  (if a whole DM abundance is in the form of subhalos and is uniformly distributed). So, by requiring  $x_{\max} \gtrsim 10^{-3} - 10^{-2}$  for sizable optical depths, we obtain  $M_{\text{NFW}} \gtrsim 10^7 - 10^9 M_\odot$ . This is the current lower limit [81–84], which will not be improved significantly in the future.

## A.2 Range of diffractive lensing near a caustic

Near a caustic, time-delays between the images formed just around corresponding critical lines are very small. Thus, very high frequency is needed to reach the geometric-optics regime. We quantify this condition.

Start from a dimensionless time-delay in Eq. (3.5) ( $x = r/r_E$ )

$$\hat{T}_d(\mathbf{x}, \mathbf{x}_s) = \frac{1}{2} |\mathbf{x} - \mathbf{x}_s|^2 - \psi(x), \quad (\text{A.4})$$

which appears in the path integral as  $\int d^2 \mathbf{x} \exp[iw \hat{T}_d(\mathbf{x}, \mathbf{x}_s)]$ . The locations of geometric-optics images are stationary points, yielding the lens equation

$$\hat{T}'_d = 0 \quad \leftrightarrow \quad \mathbf{x}_s = \mathbf{x} - \psi'(x). \quad (\text{A.5})$$

For given  $\mathbf{x}_s$  with  $x_s > 0$ , images can form in either side. Removing the vector notation and using  $x > 0$ , we obtain two lens equations

$$x_s = x - \psi'(x), \quad x_s = -x + \psi'(x). \quad (\text{A.6})$$

At the caustic  $x_s = 0$ , images are formed at the critical line  $x_t$  (in this case, the Einstein radius  $x_t = x_E = 1$ )

$$x_t = \psi'(x_t), \quad (\text{A.7})$$

and the two solutions are connected to form an Einstein ring. Near a caustic with  $x_s \neq 0$ , two image locations are  $x_t + \delta x$  and  $-x_t + \delta x$  satisfying

$$x_s = \delta x - \psi''(x_t)\delta x \quad \leftrightarrow \quad \delta x = \frac{x_s}{1 - \psi''(x_t)}. \quad (\text{A.8})$$

Thus, one image (in the same direction) is slightly outside the critical line, while the other (in the opposite direction) is slightly inside. Note that  $\delta x$  and  $x_s$  are proportional to each other.

The dimensionless time-delay of each image is

$$\begin{aligned} \hat{T}_d(x_t + \delta x) &\simeq \hat{T}_d(x_t) + \hat{T}'_d(x_t)\delta x + \dots \\ &= \frac{1}{2}(x_t - x_s)^2 - \psi(x_t) + ((x_t - x_s) - \psi'(x_t))\delta x, \end{aligned} \quad (\text{A.9})$$

and

$$\begin{aligned} \hat{T}_d(-x_t + \delta x) &\simeq \hat{T}_d(-x_t) + \hat{T}'_d(-x_t)\delta x + \dots \\ &= \frac{1}{2}(x_t + x_s)^2 - \psi(x_t) + ((x_t + x_s) - \psi'(x_t))\delta x. \end{aligned} \quad (\text{A.10})$$

The relative time-delay is then

$$\Delta \hat{T}_d = \hat{T}_d(-x_t + \delta x) - \hat{T}_d(x_t + \delta x) \quad (\text{A.11})$$

$$\simeq 2x_t x_s + 2x_s \delta x = 2x_t x_s + \mathcal{O}(x_s^2). \quad (\text{A.12})$$

Thus, diffraction occurs inside the Einstein radius if

$$w \lesssim \frac{1}{2x_t x_s} \quad \leftrightarrow \quad r_F \gtrsim 2\sqrt{r_E r_s} \quad (\text{A.13})$$

rather than  $w \lesssim 2/x_s^2$  (or  $r_F \gtrsim r_s$ ) outside the Einstein radius. This is the innermost range of (strong) diffractive lensing discussed in Eq. (3.12).

### A.3 Single image of diffractive lensing

We prove that diffractive lensing is single-imaged and that the image is always magnified as shown in Fig. 3.3. The proofs are based on existing theorems and logics for general lensing properties; see e.g. [132].

Each image is associated with an index characterizing whether it is located at an extremum or a saddle point of  $\hat{T}_d$  surface. Define the angle  $\varphi$  of the gravity force field on the lens plane as  $\nabla \hat{T}_d \propto (\cos \varphi, \sin \varphi)$ . The index can be defined as the loop integral of  $\varphi$  around the image:  $\frac{1}{2\pi} \oint_C d\varphi = +1$  for a maximum or a minimum and  $-1$  for a saddle. Index theorem says that a closed-integral along an arbitrary loop is the sum of all enclosed indices

$$\frac{1}{2\pi} \oint_C d\varphi = n_{\max} + n_{\min} - n_{\text{saddle}}, \quad (\text{A.14})$$

where the total number of images is  $n = n_{\max} + n_{\min} + n_{\text{saddle}}$ . Since  $\hat{T}_d$  has an absolute minimum (corresponding to the minimum travel time),  $n_{\min} \geq 1$ .

In the diffractive regime sufficiently far away from a lens, (1)  $A \rightarrow I$  identity, and (2)  $\nabla \hat{T}_d$  is radial. The latter implies  $\frac{1}{2\pi} \oint_C d\varphi = 1$ . The former implies  $\text{tr} A > 0$  and  $\det A > 0$  so that all images are of the minimum-type (a saddle-type has  $\det A < 0$  while a maximum  $\text{tr} A < 0$ ). Therefore,  $n = n_{\min} = 1$ ; diffractive lensing produces a single image, of the minimum-type.

The (1) also implies  $\text{tr} A = 2(1 - \kappa) > 0$  (with  $\kappa > 0$ ) and  $\det A = (1 - \kappa)^2 - \gamma^2 > 0$

so that  $\gamma < 1 - \kappa \leq 1$ , hence  $\det A < 1$ . Thus, the magnification of the single image is  $\mu = 1/\det A > 1$ , always magnified.

## A.4 Formulation of $\ln p$

The inner product between two time domain waveforms,  $h_1(t)$  and  $h_2(t)$ , is defined as

$$(h_1|h_2) = 4 \operatorname{Re} \int_0^\infty df \frac{\tilde{h}_1^*(f) \tilde{h}_2(f)}{S_n(f)}, \quad (\text{A.15})$$

where  $\tilde{h}_1(f)$ ,  $\tilde{h}_2(f)$  are the Fourier transform of the time domain waveform and  $S_n(f)$  is the noise spectral density of the detector. For a detector output  $s(t)$  and a waveform template  $h_{\lambda_1, \lambda_2, \dots}$ , where  $\lambda_1, \lambda_2, \dots$  are free parameters of the template, the best-fit waveform  $h_{\text{BF}}$  is the waveform that minimizes the inner product

$$\mathcal{D} = (s - h_{\lambda_1, \lambda_2, \dots} | s - h_{\lambda_1, \lambda_2, \dots}). \quad (\text{A.16})$$

The lensed gravitational waveform in frequency domain  $\tilde{h}_L$  is given by

$$\tilde{h}_L(f) = F(f) \tilde{h}(f), \quad (\text{A.17})$$

where  $\tilde{h}(f)$  is an ordinary gravitational wave without lensing effects generated by compact binary coalescence.

Suppose the signal  $s(t)$  is well described by the lensed waveform  $\tilde{h}_L(f) = F(f) \tilde{h}_{\lambda_1^0, \lambda_2^0, \dots}(f)$  and we have unlensed template  $\tilde{h}_{\lambda_1, \lambda_2, \dots}(f)$ . Then the best-fit waveform  $h_{\text{BF}}$  is given by minimizing

$$\begin{aligned} \mathcal{D} &= (h_L - h_{\lambda_1, \lambda_2, \dots} | h_L - h_{\lambda_1, \lambda_2, \dots}) \\ &= (F h_{\lambda_1^0, \lambda_2^0, \dots} | F h_{\lambda_1^0, \lambda_2^0, \dots}) - 2(F h_{\lambda_1^0, \lambda_2^0, \dots} | h_{\lambda_1, \lambda_2, \dots}) \\ &\quad + (h_{\lambda_1, \lambda_2, \dots} | h_{\lambda_1, \lambda_2, \dots}) \end{aligned} \quad (\text{A.18})$$

in the parameter space  $\lambda_1, \lambda_2, \dots$ . In general, the parameter space includes total mass, mass ratio of the compact binary, luminosity distance to the source, and etc.

However, for simplicity of analysis, we consider only three parameters; constant phase  $\phi_c$ , overall amplitude  $A$ , and coalescence time  $t_c$ . Then, the lensed waveform and the template waveform can be written as

$$\tilde{h}_L(f) = F(f)\tilde{h}_0(f) \quad (\text{A.19})$$

$$\tilde{h}(f) = \tilde{h}_0(f)Ae^{i\phi_c+2\pi ift_c}, \quad (\text{A.20})$$

where the waveform  $\tilde{h}_0(f)$  contains all the other parameter dependence of GW waveform. Here, we set  $\phi_c^0 = t_c^0 = 0$  since they can be arbitrary. Then,  $\mathcal{D}$  is given by

$$\mathcal{D} = (Fh_0|Fh_0) - 2A(Fh_0|h_0e^{i\phi_c+2\pi ift_c}) + A^2(h_0|h_0). \quad (\text{A.21})$$

We can solve the minimization problem of Eq. (A.21) analytically for  $\phi_c$  and  $A$ . If  $\mathcal{D}$  is minimized for  $\phi_c$  and  $A$ , it satisfies

$$\begin{aligned} \frac{\partial \mathcal{D}}{\partial \phi_c} &= -iA \left[ e^{i\phi_c} \langle Fh_0|h_0e^{2\pi ift_c} \rangle - (\text{c.c.}) \right] \\ &= 0 \end{aligned} \quad (\text{A.22})$$

$$\begin{aligned} \frac{\partial \mathcal{D}}{\partial A} &= 2 \left[ A(h_0|h_0) - (Fh_0|h_0e^{i\phi_c+2\pi ift_c}) \right] \\ &= 0, \end{aligned} \quad (\text{A.23})$$

where we define complex overlap

$$\langle h_1|h_2 \rangle = 4 \int_0^\infty df \frac{\tilde{h}_1^*(f)\tilde{h}_2(f)}{S_n(f)}, \quad (\text{A.24})$$

and (c.c) denotes complex conjugate of the other term in the same parenthesis. The equations are solved by

$$e^{i\phi_c} = \frac{|\langle Fh_0|h_0e^{2\pi ift_c} \rangle|}{\langle Fh_0|h_0e^{2\pi ift_c} \rangle}, \quad (\text{A.25})$$

$$\begin{aligned} A &= \frac{(Fh_0|h_0e^{i\phi_c+2\pi ift_c})}{(h_0|h_0)} \\ &= \frac{|\langle Fh_0|h_0e^{2\pi ift_c} \rangle|}{(h_0|h_0)}. \end{aligned} \quad (\text{A.26})$$

Now, we have

$$\mathcal{D} = (Fh_0|Fh_0) - \frac{|\langle Fh_0|h_0e^{2\pi ift_c}\rangle|^2}{(h_0|h_0)}. \quad (\text{A.27})$$

Following the definition of GW data analysis, SNR of the lensed signal,  $\rho_L$ , and SNR of the unlensed template,  $\rho_{uL}$  are defined as

$$\rho_L^2 = (h_L|h_L) = (Fh_0|Fh_0), \quad (\text{A.28})$$

$$\rho_{uL}^2 = (h_L|h_{\text{BF}}) = \max_{t_c} \frac{|\langle Fh_0|h_0e^{2\pi ift_c}\rangle|^2}{(h_0|h_0)}, \quad (\text{A.29})$$

where

$$\tilde{h}_{\text{BF}}(f) = \frac{|\langle Fh_0|h_0e^{2\pi if\hat{t}_c}\rangle|^2}{(h_0|h_0)\langle Fh_0|h_0e^{2\pi if\hat{t}_c}\rangle} \tilde{h}_0(f)e^{2\pi if\hat{t}_c}, \quad (\text{A.30})$$

and  $\hat{t}_c$  is the coalescence time difference at which  $\rho_{uL}$  is defined. Then, the minimum of  $\mathcal{D}$  is given by

$$\mathcal{D} = \rho_L^2 - \rho_{uL}^2. \quad (\text{A.31})$$

The log-likelihood ratio,  $\ln p$ , is given by

$$\ln p = -\frac{1}{2}\mathcal{D} = -\frac{1}{2}(\rho_L^2 - \rho_{uL}^2). \quad (\text{A.32})$$

This likelihood ratio can be interpreted as the probability that the fluctuation in the signal is just a noise. We claim the detection of lensing signal when  $\ln p$  achieves  $3\sigma$  significance, i.e.,

$$\begin{aligned} \ln p &= \ln \left( 1 - \int_{-3}^3 dx \frac{1}{\sqrt{2\pi}} e^{-\frac{1}{2}x^2} \right) \\ &= -5.914 \dots \end{aligned} \quad (\text{A.33})$$

## A.5 Derivation of maximum $|\ln p|$

In this section, we derive Eq. (3.63). The lensing amplification factor  $F(f)$  can be written as

$$F(u) = F_{\max} - \int_{u_{\min}}^{u_{\max}} du' \frac{dF(u')}{du'} \Theta(u' - u), \quad (\text{A.34})$$

where  $u = \ln f$ ,  $F_{\max} = F(u_{\max})$  and  $\Theta(u)$  is the unit step function. If the phase evolution of  $F(f)$  is small, we can set  $t_c \sim 0$  in Eq. (A.29). Inserting  $F(u)$  in Eqs. (A.28) and (A.29), the lensed and unlensed SNRs are given by

$$\begin{aligned} \rho_L^2 &= |F_{\max}|^2 \rho_0^2 - 2\text{Re} \int_{u_{\min}}^{u_{\max}} du' F_{\max}^* \frac{dF(u')}{du'} R(u') \\ &+ 2\text{Re} \int_{u_{\min}}^{u_{\max}} du' \int_{u'}^{u_{\max}} du'' \frac{dF^*(u')}{du'} \frac{dF(u'')}{du''} R(u'), \end{aligned} \quad (\text{A.35})$$

and

$$\begin{aligned} \rho_{uL}^2 &= |F_{\max}|^2 \rho_0^2 - 2\text{Re} \int_{u_{\min}}^{u_{\max}} du' F_{\max}^* \frac{dF(u')}{du'} R(u') \\ &+ \frac{1}{\rho_0^2} \left| \int_{u_{\min}}^{u_{\max}} du' \frac{dF(u')}{du'} R(u') \right|^2, \end{aligned} \quad (\text{A.36})$$

respectively. Here we define

$$R(u) \equiv 4 \int_u^{u_{\max}} du e^{-u} \frac{|h(u)|^2}{S_n(u)} = 4 \int_f^{f_{\max}} df \frac{|h(f)|^2}{S_n(f)}, \quad (\text{A.37})$$

and  $\rho_0^2 = R(u_{\min})$ . Thus, we have

$$\begin{aligned} \ln p &= -\text{Re} \int_{u_{\min}}^{u_{\max}} du' \int_{u'}^{u_{\max}} du'' \frac{dF^*(u')}{du'} \frac{dF(u'')}{du''} \\ &\times R(u') \left( 1 - \frac{R(u'')}{\rho_0^2} \right). \end{aligned} \quad (\text{A.38})$$

Note the inequality

$$R(u') \left( 1 - \frac{R(u'')}{\rho_0^2} \right) \leq \frac{\rho_0^2}{4}, \quad (\text{A.39})$$

where equality holds for  $R(u_0) = \rho_0^2/2$  for some  $u_0 = \ln f_0$ . If  $dF(u)/du$  is a slowly varying function in  $u$ , it is approximately

$$|\ln p| \simeq \frac{1}{8} \left[ \rho_0 \left| \frac{dF(\ln f_0)}{d \ln f} \right| \ln \frac{f_{\max}}{f_{\min}} \right]^2. \quad (\text{A.40})$$

In diffraction regime, using the approximation Eq. (3.29), we get

$$|\ln p| \simeq \frac{1}{8} \left[ \rho_0 \left| \gamma \left( \frac{r_F(f_0) e^{i\frac{\pi}{4}}}{\sqrt{2}} \right) \right| \ln \frac{f_{\max}}{f_{\min}} \right]^2. \quad (\text{A.41})$$

## A.6 Example diffractive lensing cross-sections

As shown in Fig. 3.5,  $|\ln p|$  tends to decreasing function with  $x_s$ , we can define  $x_s^{\max}$  as

$$\ln p(x_s^{\max}) = -5.914, \quad (\text{A.42})$$

where  $-5.914$  corresponds to  $3\sigma$  detection criteria. This definition leads to lensing cross-section Eq. (3.59). In Fig. A.1, we show an example of  $x_s^{\max}$  (black contour curves). We assume LISA observation of chirping GW from  $M_{\text{BBH}} = 10^6 M_\odot$  BBH, and NFW lens  $M_{\text{NFW}} = 10^7 M_\odot$ . To show a length scale more clearly,  $r_s^{\max} \equiv \sqrt{\sigma_l/\pi}$  is denoted on the contours. Square of the numbers times  $\pi$  is just the lensing cross-section in  $\text{pc}^2$  for a given  $z_l$  and  $z_s$ . Note that the lensing cross-section in Fig. A.1 has 10pc length scale which coincide with  $r_F$  scale of the GW source in LISA band ( $f \sim 10^{-3}\text{Hz}$ ). The results can be understood by the diffraction condition  $r_F > r_s$ . When GW SNR is sufficiently large, frequency dependent  $F(f)$  within GW spectrum is enough for lensing detection. Thus, the length scale of  $r_s^{\max}$  cannot be significantly larger than  $r_F$  length scale of a given GW spectrum. In other words, mostly those two have similar length scale as long as GW SNR is not a limiting factor.



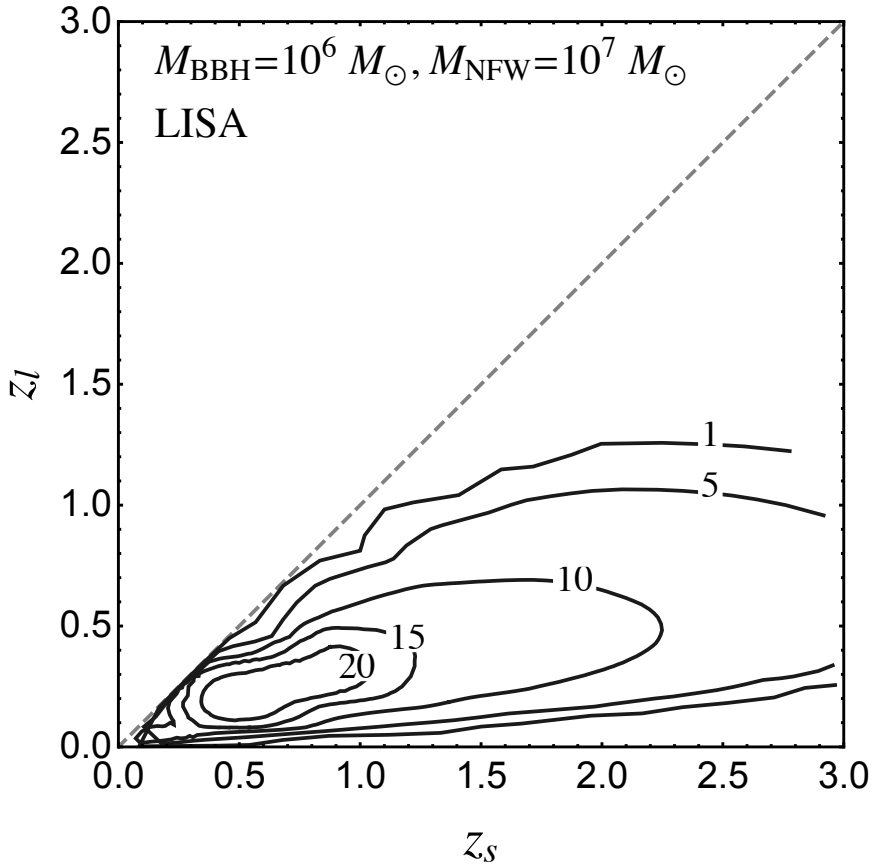


Figure A.1 Contours of lensing cross-section in  $z_s - z_l$  space. The number on the contours are  $r_s^{\max} \equiv \sqrt{\sigma_l/\pi}$  in parsec. Likewise in Fig. 3.5, LISA observation is assumed and the source and lens mass are set to  $M_{\text{BBH}} = 10^6 M_{\odot}$  and  $M_{\text{NFW}} = 10^7 M_{\odot}$ , respectively.

# Bibliography

- [1] B. P. Abbott *et al.* [LIGO Scientific and Virgo Collaborations], “Observation of Gravitational Waves from a Binary Black Hole Merger,” *Phys. Rev. Lett.* **116**, no. 6, 061102 (2016)
- [2] B. P. Abbott *et al.* [LIGO Scientific and Virgo Collaborations], “Astrophysical Implications of the Binary Black-Hole Merger GW150914,” *Astrophys. J.* **818**, no. 2, L22 (2016)
- [3] B. P. Abbott *et al.* [LIGO Scientific and Virgo Collaborations], “Tests of general relativity with GW150914,” *Phys. Rev. Lett.* **116**, no. 22, 221101 (2016)  
Erratum: [*Phys. Rev. Lett.* **121**, no. 12, 129902 (2018)]
- [4] B. P. Abbott *et al.* [LIGO Scientific and Virgo], *Phys. Rev. X* **9**, no.3, 031040 (2019)
- [5] B. P. Abbott *et al.* [LIGO Scientific and Virgo Collaborations], “GW170817: Observation of Gravitational Waves from a Binary Neutron Star Inspiral,” *Phys. Rev. Lett.* **119**, no. 16, 161101 (2017)
- [6] R. Abbott *et al.* [LIGO Scientific and Virgo], *Phys. Rev. Lett.* **125**, no.10, 101102 (2020)

- [7] R. A. Isaacson, *Phys. Rev.* **166**, 1272-1279 (1968)
- [8] B. P. Abbott *et al.* [LIGO Scientific and Virgo and 1M2H and Dark Energy Camera GW-E and DES and DLT40 and Las Cumbres Observatory and VIN-ROUGE and MASTER Collaborations], “A gravitational-wave standard siren measurement of the Hubble constant,” *Nature* **551**, no. 7678, 85 (2017)
- [9] A. Nelson, S. Reddy and D. Zhou, “Dark halos around neutron stars and gravitational waves,” arXiv:1803.03266 [hep-ph].
- [10] D. Croon, A. E. Nelson, C. Sun, D. G. E. Walker and Z. Z. Xianyu, “Hidden-Sector Spectroscopy with Gravitational Waves from Binary Neutron Stars,” *Astrophys. J.* **858**, no. 1, L2 (2018)
- [11] J. Ellis, A. Hektor, G. Hutsi, K. Kannike, L. Marzola, M. Raidal and V. Vaskonen, “Search for Dark Matter Effects on Gravitational Signals from Neutron Star Mergers,” *Phys. Lett. B* **781**, 607 (2018)
- [12] J. Ellis, G. Hutsi, K. Kannike, L. Marzola, M. Raidal and V. Vaskonen, “Dark Matter Effects On Neutron Star Properties,” *Phys. Rev. D* **97**, no. 12, 123007 (2018)
- [13] L. Randall and Z. Z. Xianyu, “Induced Ellipticity for Inspiring Binary Systems,” *Astrophys. J.* **853**, no. 1, 93 (2018)
- [14] J. E. Kim and G. Carosi, “Axions and the Strong CP Problem,” *Rev. Mod. Phys.* **82**, 557 (2010)
- [15] W. Hu, R. Barkana and A. Gruzinov, “Cold and fuzzy dark matter,” *Phys. Rev. Lett.* **85**, 1158 (2000)
- [16] P. W. Graham, D. E. Kaplan and S. Rajendran, “Cosmological Relaxation of the Electroweak Scale,” *Phys. Rev. Lett.* **115**, no. 22, 221801 (2015)

- [17] P. W. Graham, D. E. Kaplan, J. Mardon, S. Rajendran and W. A. Terrano, “Dark Matter Direct Detection with Accelerometers,” *Phys. Rev. D* **93**, no. 7, 075029 (2016)
- [18] F. Piazza and M. Pospelov, “Sub-eV scalar dark matter through the super-renormalizable Higgs portal,” *Phys. Rev. D* **82**, 043533 (2010)
- [19] B. Bertotti, L. Iess and P. Tortora, *Nature* **425**, 374 (2003).
- [20] P. C. C. Freire, M. Kramer and N. Wex, *Class. Quant. Grav.* **29**, 184007 (2012)
- [21] A. M. Archibald *et al.*, *Nature* **559**, no. 7712, 73 (2018)
- [22] D. Blas, D. L. Nacir and S. Sibiryakov, “Ultralight Dark Matter Resonates with Binary Pulsars,” *Phys. Rev. Lett.* **118**, no. 26, 261102 (2017)
- [23] J. Huang, M. C. Johnson, L. Sagunski, M. Sakellariadou and J. Zhang, “Prospects for axion searches with Advanced LIGO through binary mergers,” arXiv:1807.02133 [hep-ph].
- [24] J. Kopp, R. Laha, T. Opferkuch and W. Shepherd, “Cuckoo’s Eggs in Neutron Stars: Can LIGO Hear Chirps from the Dark Sector?,” arXiv:1807.02527 [hep-ph].
- [25] S. Alexander, E. McDonough, R. Sims and N. Yunes, “Hidden-Sector Modifications to Gravitational Waves From Binary Inspirals,” arXiv:1808.05286 [gr-qc].
- [26] A. Arvanitaki, S. Dimopoulos and K. Van Tilburg, “Sound of Dark Matter: Searching for Light Scalars with Resonant-Mass Detectors,” *Phys. Rev. Lett.* **116**, no. 3, 031102 (2016)

- [27] K. Van Tilburg, N. Leefer, L. Bougas and D. Budker, “Search for ultralight scalar dark matter with atomic spectroscopy,” *Phys. Rev. Lett.* **115**, no. 1, 011802 (2015)
- [28] A. Arvanitaki, J. Huang and K. Van Tilburg, “Searching for dilaton dark matter with atomic clocks,” *Phys. Rev. D* **91**, no. 1, 015015 (2015)
- [29] Y. V. Stadnik and V. V. Flambaum, “Enhanced effects of variation of the fundamental constants in laser interferometers and application to dark matter detection,” *Phys. Rev. A* **93**, no. 6, 063630 (2016)
- [30] Y. V. Stadnik and V. V. Flambaum, “Searching for dark matter and variation of fundamental constants with laser and maser interferometry,” *Phys. Rev. Lett.* **114**, 161301 (2015)
- [31] J. P. W. Verbiest *et al.*, “The International Pulsar Timing Array: First Data Release,” *Mon. Not. Roy. Astron. Soc.* **458**, no. 2, 1267 (2016)
- [32] N. K. Porayko *et al.*, *Phys. Rev. D* **98**, no. 10, 102002 (2018)
- [33] J. G. Williams, S. G. Turyshev and D. Boggs, “Lunar Laser Ranging Tests of the Equivalence Principle,” *Class. Quant. Grav.* **29**, 184004 (2012)
- [34] A. Arvanitaki, P. W. Graham, J. M. Hogan, S. Rajendran and K. Van Tilburg, “Search for light scalar dark matter with atomic gravitational wave detectors,” *Phys. Rev. D* **97**, no. 7, 075020 (2018)
- [35] A. Pierce, K. Riles and Y. Zhao, “Searching for Dark Photon Dark Matter with Gravitational Wave Detectors,” *Phys. Rev. Lett.* **121**, no. 6, 061102 (2018)
- [36] E. G. Adelberger, B. R. Heckel and A. E. Nelson, “Tests of the gravitational inverse square law,” *Ann. Rev. Nucl. Part. Sci.* **53**, 77 (2003)

- [37] T. A. Wagner, S. Schlamminger, J. H. Gundlach and E. G. Adelberger, “Torsion-balance tests of the weak equivalence principle,” *Class. Quant. Grav.* **29**, 184002 (2012)
- [38] P. Touboul *et al.*, “MICROSCOPE Mission: First Results of a Space Test of the Equivalence Principle,” *Phys. Rev. Lett.* **119**, no. 23, 231101 (2017)
- [39] A. Hees, O. Minazzoli, E. Savalle, Y. V. Stadnik and P. Wolf, “Violation of the equivalence principle from light scalar dark matter,” *Phys. Rev. D* **98**, no. 6, 064051 (2018)
- [40] A. Hees, J. Guena, M. Abgrall, S. Bize and P. Wolf, “Searching for an oscillating massive scalar field as a dark matter candidate using atomic hyperfine frequency comparisons,” *Phys. Rev. Lett.* **117**, no. 6, 061301 (2016)
- [41] Y. V. Stadnik and V. V. Flambaum, “Improved limits on interactions of low-mass spin-0 dark matter from atomic clock spectroscopy,” *Phys. Rev. A* **94**, no. 2, 022111 (2016)
- [42] B. P. Abbott *et al.* [LIGO Scientific and Virgo Collaborations], “GW150914: The Advanced LIGO Detectors in the Era of First Discoveries,” *Phys. Rev. Lett.* **116**, no. 13, 131103 (2016)
- [43] P. W. Graham, J. M. Hogan, M. A. Kasevich and S. Rajendran, “Resonant mode for gravitational wave detectors based on atom interferometry,” *Phys. Rev. D* **94**, no. 10, 104022 (2016)
- [44] P. W. Graham *et al.* [MAGIS Collaboration], “Mid-band gravitational wave detection with precision atomic sensors,” arXiv:1711.02225 [astro-ph.IM].
- [45] S. Hild *et al.*, “Sensitivity Studies for Third-Generation Gravitational Wave Observatories,” *Class. Quant. Grav.* **28**, 094013 (2011)

- [46] K. Yagi and N. Seto, “Detector configuration of DECIGO/BBO and identification of cosmological neutron-star binaries,” *Phys. Rev. D* **83**, 044011 (2011)  
Erratum: [*Phys. Rev. D* **95**, no. 10, 109901 (2017)]
- [47] P. W. Graham and S. Jung, “Localizing Gravitational Wave Sources with Single-Baseline Atom Interferometers,” *Phys. Rev. D* **97**, no. 2, 024052 (2018)
- [48] C. Cutler, “Angular resolution of the LISA gravitational wave detector,” *Phys. Rev. D* **57**, 7089 (1998)
- [49] B. P. Abbott *et al.* [LIGO Scientific and Virgo Collaborations], “Upper Limits on the Rates of Binary Neutron Star and Neutron Star-black Hole Mergers From Advanced Ligo’s First Observing run,” *Astrophys. J.* **832**, no. 2, L21 (2016)
- [50] T. Linden, “Dark matter in the Galactic center,” *IAU Symp.* **303**, 403 (2014).
- [51] C. Cutler *et al.*, “The Last three minutes: issues in gravitational wave measurements of coalescing compact binaries,” *Phys. Rev. Lett.* **70**, 2984 (1993)
- [52] C. Cutler and E. E. Flanagan, “Gravitational waves from merging compact binaries: How accurately can one extract the binary’s parameters from the inspiral wave form?,” *Phys. Rev. D* **49**, 2658 (1994)
- [53] R. Nair and T. Tanaka, “Synergy between ground and space based gravitational wave detectors. Part II: Localisation,” *JCAP* **1808**, no. 08, 033 (2018)
- [54] S. Jung and T. Kim, “A New Probe of Cosmic Strings at LIGO and Mid-band: Gravitational Lensing Fringe,” *arXiv:1810.04172 [astro-ph.CO]*.
- [55] S. Jung and C. S. Shin, “Gravitational-Wave Lensing Fringes by Compact Dark Matter at LIGO,” *arXiv:1712.01396 [astro-ph.CO]*.

- [56] S. Isoyama, H. Nakano and T. Nakamura, “Multiband Gravitational-Wave Astronomy: Observing binary inspirals with a decihertz detector, B-DECIGO,” PTEP **2018**, no. 7, 073E01 (2018)
- [57] R. Takahashi and T. Nakamura, “Deci hertz laser interferometer can determine the position of the coalescing binary neutron stars within an arc minute a week before the final merging event to black hole,” Astrophys. J. **596**, L231 (2003)
- [58] A. A. Klypin, A. V. Kravtsov, O. Valenzuela and F. Prada, “Where are the missing Galactic satellites?,” Astrophys. J. **522** (1999), 82-92
- [59] B. Moore, *et al.*, “Dark matter substructure within galactic halos,” Astrophys. J. Lett. **524** (1999), L19-L22
- [60] S. Y. Kim, A. H. G. Peter and J. R. Hargis, “Missing Satellites Problem: Completeness Corrections to the Number of Satellite Galaxies in the Milky Way are Consistent with Cold Dark Matter Predictions,” Phys. Rev. Lett. **121** (2018) no.21, 211302
- [61] E. O. Nadler *et al.* [DES], “Milky Way Satellite Census. III. Constraints on Dark Matter Properties from Observations of Milky Way Satellite Galaxies,”
- [62] N. Banik, J. Bovy, G. Bertone, D. Erkal and T. J. L. de Boer, “Evidence of a population of dark subhalos from Gaia and Pan-STARRS observations of the GD-1 stream,”
- [63] J. S. Bullock, A. V. Kravtsov and D. H. Weinberg, “Reionization and the abundance of galactic satellites,” Astrophys. J. **539** (2000), 517
- [64] V. Bromm, “Formation of the First Stars,” Rept. Prog. Phys. **76** (2013), 112901
- [65] M. R. Buckley and A. H. G. Peter, “Gravitational probes of dark matter physics,” Phys. Rept. **761** (2018), 1-60



- [66] J. W. Hsueh, *et al.*, “SHARP – VII. New constraints on the dark matter free-streaming properties and substructure abundance from gravitationally lensed quasars,” *Mon. Not. Roy. Astron. Soc.* **492** (2020) no.2, 3047-3059
- [67] D. Gilman, *et al.*, “Warm dark matter chills out: constraints on the halo mass function and the free-streaming length of dark matter with eight quadruple-image strong gravitational lenses,” *Mon. Not. Roy. Astron. Soc.* **491** (2020) no.4, 6077-6101
- [68] J. S. Bullock and M. Boylan-Kolchin, “Small-Scale Challenges to the  $\Lambda$ CDM Paradigm,” *Ann. Rev. Astron. Astrophys.* **55** (2017), 343-387
- [69] J. F. Navarro, C. S. Frenk and S. D. M. White, “The Structure of cold dark matter halos,” *Astrophys. J.* **462**, 563–575 (1996)
- [70] B. Moore, “Evidence against dissipationless dark matter from observations of galaxy haloes,” *Nature* **370** (1994), 629
- [71] R. A. Flores and J. R. Primack, “Observational and theoretical constraints on singular dark matter halos,” *Astrophys. J. Lett.* **427** (1994), L1-4
- [72] S. d. Mao and P. Schneider, “Evidence for substructure in lens galaxies?,” *Mon. Not. Roy. Astron. Soc.* **295** (1998), 587-594
- [73] C. S. Kochanek and N. Dalal, “Tests for substructure in gravitational lenses,” *Astrophys. J.* **610** (2004), 69-79
- [74] J. Chen, A. V. Kravtsov and C. R. Keeton, “Lensing optical depth for substructure and isolated dark matter halos,” *Astrophys. J.* **592** (2003), 24-31
- [75] R. B. Metcalf, “The Importance of intergalactic structure to gravitationally lensed quasars,” *Astrophys. J.* **629** (2005), 673-679

- [76] L. V. E. Koopmans, “Gravitational-mass imaging of CDM substructure,” *Mon. Not. Roy. Astron. Soc.* **363** (2005), 1136
- [77] H. Sugai, A. Kawai, A. Shimono, T. Hattori, G. Kosugi, N. Kashikawa, K. T. Inoue and M. Chiba, “Integral Field Spectroscopy of the Quadruply Lensed Quasar 1RXS J1131-1231: New Light on Lens Substructures,” *Astrophys. J.* **660** (2007), 1016-1022
- [78] D. D. Xu, *et al.*, “On the Effects of Line-of-Sight Structures on Lensing Flux-ratio Anomalies in a  $\Lambda$ CDM Universe,” *Mon. Not. Roy. Astron. Soc.* **421** (2012), 2553
- [79] E. Zackrisson and T. Riehm, “Gravitational lensing as a probe of cold dark matter subhalos,” *Adv. Astron.* **2010** (2010), 478910
- [80] Y. Hezaveh, *et al.*, “Dark Matter Substructure Detection Using Spatially Resolved Spectroscopy of Lensed Dusty Galaxies,” *Astrophys. J.* **767** (2013), 9
- [81] A. M. Nierenberg, T. Treu, S. A. Wright, C. D. Fassnacht and M. W. Auger, “Detection of substructure with adaptive optics integral field spectroscopy of the gravitational lens B1422+231,” *Mon. Not. Roy. Astron. Soc.* **442** (2014) no.3, 2434-2445
- [82] Y. D. Hezaveh, *et al.*, “Detection of lensing substructure using ALMA observations of the dusty galaxy SDP.81,” *Astrophys. J.* **823** (2016) no.1, 37
- [83] S. Asadi, E. Zackrisson and E. Freeland, “Probing cold dark matter subhaloes with simulated ALMA observations of macrolensed sub-mm galaxies,” *Mon. Not. Roy. Astron. Soc.* **472**, no.1, 129–140 (2017)
- [84] R. Fadely, C. R. Keeton, “Substructure in the lens HE 0435-1223,” *Mon. Not. Roy. Astron. Soc.* **419**, no.2, 936–951 (2012)

- [85] H. Niikura *et al.*, “Microlensing constraints on primordial black holes with Subaru/HSC Andromeda observations,” *Nat. Astron.* **3**, no. 6, 524 (2019)
- [86] M. Zumalacarregui and U. Seljak, “Limits on stellar-mass compact objects as dark matter from gravitational lensing of type Ia supernovae,” *Phys. Rev. Lett.* **121**, no. 14, 141101 (2018)
- [87] J. B. Muñoz, E. D. Kovetz, L. Dai and M. Kamionkowski, “Lensing of Fast Radio Bursts as a Probe of Compact Dark Matter,” *Phys. Rev. Lett.* **117**, no. 9, 091301 (2016)
- [88] T. T. Nakamura, “Gravitational lensing of gravitational waves from inspiraling binaries by a point mass lens,” *Phys. Rev. Lett.* **80**, 1138 (1998).
- [89] S. Jung and C. S. Shin, “Gravitational-Wave Fringes at LIGO: Detecting Compact Dark Matter by Gravitational Lensing,” *Phys. Rev. Lett.* **122**, no. 4, 041103 (2019)
- [90] A. Gould, “Femtolensing of gamma-ray bursters,” *Astrophys. J.* **386**, L5 (1992)
- [91] A. Katz, J. Kopp, S. Sibiryakov and W. Xue, “Femtolensing by Dark Matter Revisited,” *JCAP* **1812**, 005 (2018)
- [92] R. J. Nemiroff and A. Gould, “Probing for MACHOs of mass  $10^{-15}M_{\odot}$ – $10^{-7}M_{\odot}$  with gamma-ray burst parallax spacecraft,” *Astrophys. J.* **452**, L111 (1995) [[astro-ph/9505019](#)].
- [93] S. Jung and T. Kim, “Gamma-ray burst lensing parallax: Closing the primordial black hole dark matter mass window,” *Phys. Rev. Res.* **2** (2020) no.1, 013113
- [94] J. A. Dror, H. Ramani, T. Trickle and K. M. Zurek, “Pulsar Timing Probes of Primordial Black Holes and Subhalos,” *Phys. Rev. D* **100**, no. 2, 023003 (2019)

- [95] C. Mondino, A. M. Taki, K. Van Tilburg and N. Weiner, “First Results on Dark Matter Substructure from Astrometric Weak Lensing,” *Phys. Rev. Lett.* **125** (2020) no.11, 111101
- [96] R. B. Metcalf and P. Madau, “Compound gravitational lensing as a probe of dark matter substructure within galaxy halos,” *Astrophys. J.* **563** (2001), 9
- [97] M. Chiba, “Probing dark matter substructure in lens galaxies,” *Astrophys. J.* **565** (2002), 17
- [98] R. B. Metcalf and H. Zhao, “Flux ratios as a probe of dark substructures in quadruple-image gravitational lenses,” *Astrophys. J. Lett.* **567** (2002), L5
- [99] N. Dalal and C. S. Kochanek, “Direct detection of CDM substructure,” *Astrophys. J.* **572** (2002), 25-33
- [100] A. V. Maccio and M. Miranda, “The effect of low mass substructures on the cusp lensing relation,” *Mon. Not. Roy. Astron. Soc.* **368** (2006), 599-608
- [101] Y. Hezaveh, N. Dalal, G. Holder, T. Kisner, M. Kuhlen and L. Perreault Levasseur, “Measuring the power spectrum of dark matter substructure using strong gravitational lensing,” *JCAP* **11** (2016), 048
- [102] A. Diaz Rivero, F. Y. Cyr-Racine and C. Dvorkin, “Power spectrum of dark matter substructure in strong gravitational lenses,” *Phys. Rev. D* **97** (2018) no.2, 023001
- [103] F. Y. Cyr-Racine, C. R. Keeton and L. A. Moustakas, “Beyond subhalos: Probing the collective effect of the Universe’s small-scale structure with gravitational lensing,” *Phys. Rev. D* **100** (2019) no.2, 023013
- [104] S. Vegetti, *et al.*, “Gravitational detection of a low-mass dark satellite at cosmological distance,” *Nature* **481** (2012), 341

- [105] S. Vegetti, G. Despali, M. R. Lovell and W. Enzi, “Constraining sterile neutrino cosmologies with strong gravitational lensing observations at redshift  $z \sim 0.2$ ,” *Mon. Not. Roy. Astron. Soc.* **481** (2018) no.3, 3661-3669
- [106] D. Erkal and V. Belokurov, “Properties of Dark Subhaloes from Gaps in Tidal Streams,” *Mon. Not. Roy. Astron. Soc.* **454** (2015) no.4, 3542-3558
- [107] R. Feldmann and D. Spolyar, “Detecting Dark Matter Substructures around the Milky Way with Gaia,” *Mon. Not. Roy. Astron. Soc.* **446** (2015), 1000-1012
- [108] M. Buschmann, J. Kopp, B. R. Safdi and C. L. Wu, “Stellar Wakes from Dark Matter Subhalos,” *Phys. Rev. Lett.* **120** (2018) no.21, 211101
- [109] A. Bonaca, D. W. Hogg, A. M. Price-Whelan and C. Conroy, “The Spur and the Gap in GD-1: Dynamical evidence for a dark substructure in the Milky Way halo,”
- [110] L. Dai, S. S. Li, B. Zackay, S. Mao and Y. Lu, “Detecting Lensing-Induced Diffraction in Astrophysical Gravitational Waves,” *Phys. Rev. D* **98**, no.10, 104029 (2018)
- [111] R. Takahashi, “Amplitude and phase fluctuations for gravitational waves propagating through inhomogeneous mass distribution in the universe,” *Astrophys. J.* **644**, 80–85 (2006)
- [112] M. Oguri and R. Takahashi, “Probing Dark Low-mass Halos and Primordial Black Holes with Frequency-dependent Gravitational Lensing Dispersions of Gravitational Waves,” *Astrophys. J.* **901** (2020) no.1, 58
- [113] R. Takahashi and T. Nakamura, “Wave effects in gravitational lensing of gravitational waves from chirping binaries,” *Astrophys. J.* **595**, 1039 (2003)

- [114] K. H. Lai, O. A. Hannuksela, A. Herrera-Martín, J. M. Diego, T. Broadhurst and T. G. F. Li, “Discovering intermediate-mass black hole lenses through gravitational wave lensing,” *Phys. Rev. D* **98** (2018) no.8, 083005
- [115] P. Christian, S. Vitale and A. Loeb, “Detecting Stellar Lensing of Gravitational Waves with Ground-Based Observatories,” *Phys. Rev. D* **98** (2018) no.10, 103022
- [116] T. Suyama, T. Tanaka and R. Takahashi, “Exact wave propagation in a space-time with a cosmic string,” *Phys. Rev. D* **73** (2006), 024026
- [117] S. Jung and T. Kim, “Probing Cosmic Strings with Gravitational-Wave Fringe,” *JCAP* **07** (2020), 068
- [118] S. C. Grijalva and C. Calcáneo-Roldán, “Gravitational Wave Enhancement as a Tool to Distinguish Dark Matter Halo Profiles,” *Revista Mexicana de Astronomía y Astrofísica*, **55**, 231-235 (2019)
- [119] X. Guo and Y. Lu, “Convergence and Efficiency of Different Methods to Compute the Diffraction Integral for Gravitational Lensing of Gravitational Waves,” arXiv:2012.03474 [gr-qc].
- [120] J. M. Diego, O. A. Hannuksela, P. L. Kelly, T. Broadhurst, K. Kim, T. G. F. Li, G. F. Smoot and G. Pagano, “Observational signatures of microlensing in gravitational waves at LIGO/Virgo frequencies,” *Astron. Astrophys.* **627**, A130 (2019)
- [121] A. Mishra, A. K. Meena, A. More, S. Bose and J. S. Bagla, “Gravitational Lensing of Gravitational Waves: Effect of Microlens Population in Lensing Galaxies,”
- [122] T. T. Nakamura and S. Deguchi “Wave Optics in Gravitational Lensing,” *Prog. Theor. Phys. Suppl.* **133**, 137-153 (1999)

- [123] J. P. Macquart, “Scattering of gravitational radiation: Second order moments of the wave amplitude,” *Astron. Astrophys.* **422**, 761–775 (2004)
- [124] D. L. Jow, S. Foreman, U. L. Pen and W. Zhu, “Wave effects in the microlensing of pulsars and FRBs by point masses,” *Mon. Not. Roy. Astron. Soc.* **497**, no.4, 4956–4969 (2020)
- [125] K. S. Thorne, R. D. Blandford, “Modern Classical Physics: Optics, Fluids, Plasmas, Elasticity, Relativity, and Statistical Physics” (Princeton Univ. Press, 2017)
- [126] P. Schneider, C. Kochanek, J. Wambsganss, “Gravitational Lensing: Strong, Weak and Micro,” (Springer, Berlin, Heidelberg, 2006)
- [127] D. E. Holz and R. M. Wald, “A New method for determining cumulative gravitational lensing effects in inhomogeneous universes,” *Phys. Rev. D* **58** (1998), 063501
- [128] R. M. Wald, “General Relativity,” (University of Chicago Press, 1984).
- [129] C. R. Keeton, “A catalog of mass models for gravitational lensing,” arXiv:astro-ph/0102341 [astro-ph].
- [130] C. Okoli and N. Afshordi, “Concentration, Ellipsoidal Collapse, and the Densest Dark Matter haloes,” *Mon. Not. Roy. Astron. Soc.* **456**, no.3, 3068–3078 (2016)
- [131] C. Okoli, “Dark matter halo concentrations: a short review,” arXiv:1711.05277 [astro-ph.CO].
- [132] P. Schneider, J. Ehlers, E. E. Falco, “Gravitational Lenses,” (Springer, New York, 1992).

- [133] P. Ajith *et al.* “A Template bank for gravitational waveforms from coalescing binary black holes. I. Non-spinning binaries,” *Phys. Rev. D* **77**, 104017 (2008) [erratum: *Phys. Rev. D* **79**, 129901 (2009)]
- [134] P. Amaro-Seoane *et al.* [LISA], “Laser Interferometer Space Antenna,” arXiv:1702.00786 [astro-ph.IM].
- [135] T. Robson, N. J. Cornish and C. Liu, “The construction and use of LISA sensitivity curves,” *Class. Quant. Grav.* **36**, no.10, 105011 (2019)
- [136] C. Cutler and D. E. Holz, “Ultra-high precision cosmology from gravitational waves,” *Phys. Rev. D* **80**, 104009 (2009)
- [137] P. W. Graham *et al.* [MAGIS], “Mid-band gravitational wave detection with precision atomic sensors,” arXiv:1711.02225 [astro-ph.IM].
- [138] P. W. Graham, J. M. Hogan, M. A. Kasevich and S. Rajendran, “Resonant mode for gravitational wave detectors based on atom interferometry,” *Phys. Rev. D* **94**, no.10, 104022 (2016)
- [139] M. Punturo *et al.* “The Einstein Telescope: A third-generation gravitational wave observatory,” *Class. Quant. Grav.* **27**, 194002 (2010)
- [140] W. H. Press and P. Schechter, *Astrophys. J.* **187**, 425-438 (1974) doi:10.1086/152650
- [141] R. K. Sheth and G. Tormen, *Mon. Not. Roy. Astron. Soc.* **308**, 119 (1999) doi:10.1046/j.1365-8711.1999.02692.x [arXiv:astro-ph/9901122 [astro-ph]].
- [142] M. Bonetti, A. Sesana, F. Haardt, E. Barausse and M. Colpi, “Post-Newtonian evolution of massive black hole triplets in galactic nuclei – IV. Implications for LISA,” *Mon. Not. Roy. Astron. Soc.* **486**, no.3, 4044–4060 (2019)



# 초록

이 논문에서 우리는 중력파를 이용해 암흑물질 물리학을 탐사하는 새로운 방법을 보여준다. 우리는 가벼운 스칼라 암흑물질이 중성자와 상호작용해서 그것에 시간-진동성 질량 변화를 일으킨다면, 중성자별 쌍성의 나선운동에서 나온 중력파 처프 신호가 그 효과에 민감할 것임을 알아냈다. 그 민감함은 광대역(0.01 Hz – 1000 Hz)에서 1년 이상의 중력파 측정으로 얻은 매우 큰 수치의 중력파 진동횟수 덕분이다. 그러한 광대역 측정은 미래에 LIGO와 중간-주파수 중력파 관측기를 포함하는 관측소 네트워크에 의해 실현될 수 있으며, 가벼운 스칼라 암흑물질의 아직 탐사되지 못한 파라미터 영역을 탐사할 것이다.

우리는 또한 중력파의 중력렌즈현상이 은하규모 미만( $M < 10^7 M_\odot$ )의 암흑물질 서브-헤일로 탐사할수 있는 수단임을 보였다. 빛의 중력렌즈현상으로는 그러한 규모를 탐사하기가 쉽지 않았다. 중력파의 특별한 점은 그것의 프레넬 길이가 파섹 규모라는 것인데, 이는 그것의 긴 파장과 파원까지의 우주론적 거리 덕분이다. 이는 중력파 처프 신호가 파섹 규모의 서브-헤일로에 의해 회절될 수 있게 했다. 우리는 그 회절성 렌즈 신호가 렌즈물체의 *shear* 분포와 동일함을 보였고, 따라서 그것이 렌즈의 물질분포를 재구성하는데 이용될 수 있음을 보였다. 그러한 중력파의 중력렌즈현상은 BBO 디텍터에서 1년에 수십번 정도 관측할것으로 예측된다.

**주요어:** 중력파, 암흑물질, 중력렌즈

**학번:** 2015-20356

# 감사의 글

무엇보다도 박사학위를 받기까지 저를 이끌어주신 정성훈 교수님께 깊이 감사드립니다. 지난 3년간 행복한 연구활동을 할 수 있었던 것은 교수님의 아낌없는 가르침, 그리고 응원과 격려 덕분입니다. 교수님께서 지도교수로서 보여주신 책임감 있는 리더십, 근면함 그리고 물리적 직관은 제가 한명의 연구자로 성장하는데 큰 영감을 주었습니다. 그리고 저의 첫 지도교수님이셨던 이형목 교수님께도 큰 은혜를 입었습니다. 무엇보다 중력과 천체물리학이라는 신선하고 흥미로운 분야를 접할 수 있게 된 것은 이형목 교수님 덕분입니다.

바쁜 와중에도 시간을 내어 논문심사에 참석해주신 김형도 교수님, 김석 교수님 그리고 정동희 교수님께도 매우 감사드립니다. 특히 김형도 교수님의 날카로운 지적은 발표준비에 많은 도움이 되었습니다. 간간이 토론 상대가 되어 주시고, 연구자의 진로에 대해서도 많은 조언을 해주셨던 이준규 교수님께도 감사의 말을 드리고 싶습니다.

언제나 중력과 전공 후배들을 챙겨주시는 박찬 박사님, 김진호 박사님, 배영복 박사님, 그리고 김영민 박사님 등 한국 중력과 그룹 박사님들께 이 자리를 빌어 감사를 표합니다. 코로나 19 사태 때문에 박사님들을 자주 뵙지 못하게 되어 아쉬울 따름입니다. 그리고 중력 현상에 대해 항상 진지하게 토론에 참여해주신 조기혁 선배에게도 정말 고맙다는 말을 하고 싶습니다. 그리고 정성훈 교수님 연구실멤버인 김태훈, 이정환, 박찬웅 학생에게도 물리에 대해 많이 배울 수 있었어서 고맙고, 동시에 선배로서 많이 챙겨주지 못해 미안한 마음이 듭니다. 특히 박찬웅 학생의 도움이 없었다면 중력렌즈 연구를 끝마치지 못했을 것이라 특히 더 고맙습니다.

물리학과 친구들이 없었다면 고된 대학원 생활을 버티나갈 수 없었을 것입니다. 56동 5층 멤버였던 준, 동섭은 대학원 일상을 함께한 소중한 친구들입니다. 무엇보다 준의 경험과 동섭이 남긴 메뉴얼 덕분에 박사 졸업 절차를 수월하게 준비할 수 있었고, 다시 한번 고맙다는 말을 하고 싶습니다. 그리고 정수와 핵물리학과 피아노 등 다양한 얘기를

나눴던 티타임은 대학원 생활에서 잊지 못할 추억일 것이며, 그와 동시에 선배로서 해주었던 조언은 많은 도움이 되었습니다. 굵든 저를 매번 잘 챙겨주었던 상현, 학자로서 배울 점이 많았던 도현, 그리고 같은 취미를 공유할 수 있었던 성전, 모두 대학원 생활의 든든한 버팀목이 되어준 고마운 친구들입니다.

천문학과 친구들을 빼놓고는 제 대학원 생활을 얘기할 수 없을 것입니다. 물리학을 제외한 좋은 것 - 천문학, 와인, 맥주, 커피, 음식, 음악 등등... - 대부분을 천문학과 친구들로부터 배울 수 있었기 때문입니다. 상혁이 없었다면 학부 대학원에 이르는 제 학창시절은 밋밋한 56동 건물을 닮아 있었을 것입니다. 그리고 무엇보다 천문학과 사람들과의 인연은 상혁 덕입니다. 호진과 윤수는 여러모로(위트 포함) 배울점이 많았던 친구들입니다. 19동의 바쿠스, 민철이형에게도 정말 신세를 많이 졌습니다. 이 졸업논문을 준비하던 시기에 저를 많이 챙겨주었던 성아에게도 이 자리를 빌어 고맙다는 말을 하고 싶습니다.

그 외에도 감사인사를 전하고 싶은 사람은 얼마든지 있습니다. 우선, 한 학기 앞서 박사졸업한 선배로서 여러 격려와 조언을 해주었던 지홍이에게 감사합니다. 분야를 막론하고 학술활동은 커피를 글로 변환하는 과정이라고 할 수 있습니다. 그런 의미에서 항상 최고의 커피를 내려주시고 다채로운 커피의 세계를 경험할 수 있게 해주신 윤석커피 사장님께 감사드리고 싶습니다. 그리고 학술활동 또한 일종의 커뮤니케이션으로서 외모가 매우 중요하다 할 수 있습니다. 그러므로, 쓰리스타일리스트 민제원장님 지난 10년간 제 헤어스타일을 맡아주셔서 감사합니다. 앞으로도 잘 부탁드립니다.

마지막으로, 부모님의 아낌없는 지원과 응원이 없었다면 저는 여기까지 해낼 수 없었을 것입니다. 오랜 시간 저를 믿고 지켜봐 주셔서 감사합니다. 그리고 역시 저를 항상 응원해준 제 동생 수정, 할머니, 그리고 지금은 하늘에 계신 할아버지 모두 감사합니다.